Land surface temperature retrieval from hyperspectral thermal infrared data

Xinyu Lan

UNIVERSITÉ DE STRASBOURG

ÉCOLE DOCTORALE MATHEMATIQUES SCIENCES DE L'INFORMATION ET DE L'INGENIEUR

[Uds – INSA - ENGEES]

THÈSE présentée par :

Xinyu LAN

soutenue le : **07 Octobre 2020**

pour obtenir le grade de : **Docteur de l'université de Strasbourg**

Discipline/ Spécialité : Electronique/Télédétection

Land surface temperature retrieval from hyperspectral thermal infrared data

THÈSE dirigée par :

M. Z-L. LI	Directeur de Recherches CNRS, France

RAPPORTEURS :

M. J. SOBRINO	Professeur, Université de Valencia, Espagne
M. H. WU	Directeur de Recherches CAS, Chine

AUTRES MEMBRES DU JURY :

Mme J. Labed	Maître de Conférence, UdS, France
Mme F. NERRY	Directeur de Recherches CNRS, France
M. B-H. TANG	Directeur de Recherches de IGSNRR, Chine

Acknowledgements

During my four years as a doctoral student, I gained a lot of help from teachers, classmates and friends. I really want to express my thanks to them.

First of all, I want to express my great respect and deep appreciation to my supervisor Professor Zhao-liang Li. Professor Li helped me a lot in my study and life. On 30 September 2016, I arrived in France. At that time, I was unfamiliar with France and had problems communicating with local people. Professor Li and his wife Mrs. Zhao helped me find the house and solve many problems. In the past four study years, Professor Li instructed me with the greatest patience. He helped me modify each part of work and gave me many suggestions. I truly felt the rigorous, meticulous, and keen insight that a researcher possessed, with his guidance, I gradually got on the right track, gradually understanding, familiarizing, and completing research work. I am honored and very glad to be able to study under the tutelage of Professor Li.

Meanwhile, I want to present my great thankfulness to Dr. Jélila Labed and Dr. Françoise Nerry. They are kind and provide me many suggestions to promote my works. They consider for me whether every word in the work is accurate and whether every sentence is fluent. I express my most sincere respect and gratitude to them.

Thanks also for the help of Dr. Xiaojing Han, Dr. Yuanyuan Chen, Dr. Ronghai Hu, Dr. Xinke Zhong, Dr. Xiaopo Zheng, Pro. Changsen Zhao. I hope all of you can live happy and healthy.

Thanks for the support of my family, especially my father, he is a great father.

Résumé

La température de surface terrestre (LST) est un paramètre clé dans les processus physiques du bilan énergétique de surface et de l'équilibre de l'eau à l'échelle régionale et globale (Anderson et al., 2008). Elle a été utilisée dans de nombreux domaines, y compris le changement climatique, l'hydrologie, l'écologie et le climat urbain. Compte tenu de l'hétérogénéité spatiale de la température de surface, les mesures au sol ne peuvent pas réellement fournir la LST à l'échelle régionale ou globale. Avec le développement de la télédétection, les données satellitaires offrent la possibilité de mesurer la LST à l'échelle globale avec une résolution temporelle suffisamment élevée et l'accès, non pas à une valeur ponctuelle, mais à une moyenne spatiale (Li et al., 2013).

La LST peut être obtenue à partir de données infrarouges thermiques (TIR) en utilisant l'équation de transfert radiatif. Plusieurs algorithmes ont été développés pour ce faire, et de nombreux résultats ont été obtenus. Cependant, du fait du problème de l'équation mal conditionnée, des hypothèses sont encore nécessaires pour restituer la LST de façon précise. Par ailleurs, le capteur multispectral a une fonction de poids large, une basse résolution verticale, et peu de canaux par rapport au capteur hyperspectral. Les données d'observation comprennent généralement des informations sur les profils atmosphériques (la température et la vapeur d'eau), la température de surface, l'émissivité de surface (LSE), et autres traces de gaz. Le nombre restreint de canaux n'est pas approprié à la restitution de la LST.

Les données TIR hyperspectrales avec des caractéristiques spectrales plus résolues fournissent beaucoup d'informations sur les processus de surface terrestre, en particulier sur le paramètre LST. Avec un grand nombre de canaux, l'hyperspectral dans le TIR peut augmenter la stabilité du système d'équations et également fournir plus de contraintes pour séparer LST et LSEs, afin d'améliorer la précision de restitution de LST. Par conséquent, notre recherche utilise les

données TIR hyperspectrales comme principale source d'information et vise à accéder, moyennant le modèle de transfert radiatif, à la LST. Cette thèse est composée de six chapitres.

Différentes méthodes d'obtention de la LST sont développées pour les données TIR multispectrales: par exemple, la méthode monocanal, l'algorithme « Split Window », la méthode d'émissivité basée sur la classification (classification-based emissivity method), la méthode des indices spectraux jour / nuit indépendants de la température (day/night temperature-independent spectral-indices method), la méthode d'émissivité du corps gris (gray body emissivity method), la méthode de séparation de la température et de l'émissivité (TES). Ces méthodes ont leurs avantages et leurs inconvénients. Mais là encore, le choix d'une méthode d'estimation de la LST dépend des caractéristiques du capteur. Ces méthodes, utilisant des données multispectrales, ne peuvent pas être directement appliquées aux données TIR hyperspectrales comportant des milliers de canaux. Pour estimer la LST à partir de données TIR hyperspectrales, il faut également rechercher l'émissivité de surface terrestre (LSE) et connaître exactement le profil atmosphérique. Certaines méthodes, par exemple la méthode de séparation d'émissivité de température de contrainte d'émissivité linéaire (linear emissivity constraint temperature emissivity separation method), la méthode spectralement lisse itérative (iterative spectrally smooth method) peuventt donner une bonne estimation de la LST avec une correction atmosphérique précise. La méthode du réseau de neurones artificiels ne nécessite pas de profil atmosphérique, mais elle nécessite des milliers de canaux. La méthode de récupération des profils atmosphériques, LST et LSE simultanément ne nécessite aucune autre information atmosphérique, mais elle est complexe en considérant la structure verticale de l'atmosphère. Par conséquent, de nouvelles méthodes et améliorations devraient permettre d'obtenir l'estimation de la LST à partir des données TIR hyperspectrales.

Le deuxième chapitre rappelle les concepts sur le rayonnement électromagnétique mentionnés dans notre thèse en particulier la théorie du

transfert radiatif atmosphérique dont l'équation couramment utilisée pour récupérer la LST pour les données TIR (Équation 1) est :

$$L(\lambda,\theta,\varphi) = \varepsilon(\lambda,\theta,\varphi)B(\lambda,T_s)\tau(\lambda,\theta,\varphi,p_s) + \int_{P_s}^{0} B\left(\lambda,T_p\right)\frac{\partial\tau(\lambda,\theta,\varphi,p)}{\partial p}dp$$
$$+\int_0^{2\pi}\int_0^{\frac{\pi}{2}}\rho(\lambda,\theta,\varphi,\theta',\varphi')\,L_d(\lambda,\theta',\varphi')\tau(\lambda,\theta,\varphi,p_s)cos\theta' sin\theta' d\theta' d\varphi' \quad (1)$$
$$+\int_0^{2\pi}\int_0^{\frac{\pi}{2}}\rho(\lambda,\theta,\varphi,\theta',\varphi')\,L_d(\lambda,\theta',\varphi')\tau(\lambda,\theta,\varphi,p_s)cos\theta' sin\theta' d\theta' d\varphi'$$
$$+\rho(\lambda,\theta,\varphi,\theta_s,\varphi_s)L_{sun}(\lambda,\theta_s,\varphi_s)\tau(\lambda,\theta_s,\varphi_s,p_s)\tau(\lambda,\theta,\varphi,p_s)$$

où $\theta,\varphi,\theta_s,\varphi_s$ sont l'angle zénithal et l'angle azimutal de l'observation et du soleil. θ'et φ' sont l'angle zénithal et l'angle azimutal de la direction descendante du rayonnement atmosphérique, respectivement. L est le rayonnement spectral mesuré au sommet de l'atmosphère (TOA). p_s est la pression au niveau de la surface. τ est la transmittance atmosphérique au TOA dans la direction d'observation. T_p est la température atmosphérique. ρ est la réflectance bidirectionnelle de la surface.

L'ensemble des données satellitaires, la base de données des profils atmosphériques et la base de données des émissivités spectrales utilisés sont présentés. Il comprend les données satellitaires de l'interféromètre infrarouge à sondage atmosphérique (IASI), les LST issues de Advanced Very High Resolution Radiometer LST, l'ensemble de données thermodynamiques Initial Guess Retrieval, la bibliothèque spectrale Advanced Spaceborne Thermal Emission Reflection Radiometer et certaines données mesurées sur le terrain. Le modèle de transfert radiatif 4A (Automatized Atmospheric Absorption Atlas) est adopté dans cette thèse comme simulation rapide du transfert radiatif pour les données TIR hyperspectrales.

Le troisième chapitre décrit une méthode proposée de restitution de la LST pour les données infrarouges thermiques hyperspectrales assocoiée à une correction atmosphérique précise. La restitution précise de la LST, qui est étroitement associée à LSEs, est un problème mal posé parce que le nombre

d'inconnues est plus grand que le nombre d'équations (pour N canaux spectraux), même si une correction atmosphérique précise a été réalisée. Il y a toujours N+1 inconnues (N LSEs et une LST) pour N équations (N luminances observées dans N canaux). La correction atmosphérique est un enjeu clé pour la détermination de LST. Les profils atmosphériques précis ne sont généralement pas disponibles de façon synchronisée avec les mesures TIR, et ainsi la précision de LST restituée peut être dégradée. Nous avons dans un premier temps supposé que la correction atmosphérique a été effectuée et avons mis au point une méthode pour obtenir la LST, basée sur la méthode de contrainte d'émissivité spectrale linéaire (LSEC) (Wang et al., 2011). En effet, une méthode pré-estimant la forme de la courbe spectrale de LSE (PSE)-LSEC a été proposée. Elle consiste à extraire, à partir de cette pré-estimation, la position des crêtes et des creux assurant un meilleur schéma de segmentation avec des intervalles différents et modifiables pour séparer LST et LSE.

Les expériences numériques ont montré que lorsque le bruit du capteur (NEΔT = 0.5 K) est ajouté aux données IRT simulées au sol, l'écart type (RMSE) de la LST est de 0.07 K (Figure 1). Ce qui implique que l'erreur de 0.5 K sur la température de brillance au niveau du sol a une influence relativement faible sur la restitution de la LST. Lorsque l'erreur sur le rayonnement atmosphérique descendant (le profil d'humidité est décalé de 1.2) est ajoutée aux données simulées, le RMSE de la LST est proche de 1 K. Par rapport à la méthode spectralement lisse itérative (ISSTES), PES-LSEC est moins sensible au bruit pour restituer LES (Figure 2). Par contre, l'erreur sur le profil d'humidité, impacte l'erreur du rayonnement atmosphérique descendant de façon plus importante avec la méthode PES-LSEC. Pour les mesures in situ, avec l'estimation de forme initiale, la méthode PSE-LSEC a obtenu, avec moins de segmentations, une meilleure précision de la LST que celle de la méthode LSEC. Les crêtes et les creux de la courbe spectrale de LSE sont mieux conservés à l'aide de la méthode PSE-LSEC. La précision de la restitution de la LST a été améliorée dans une certaine mesure. Pour la plupart des échantillons, les erreurs sur la LST se situent à moins de 1 K (Figure 3). Ces

résultats ont montré que la méthode PSE-LSEC pouvait donner une LST précise avec les données hyperspectrales TIR au niveau du sol.

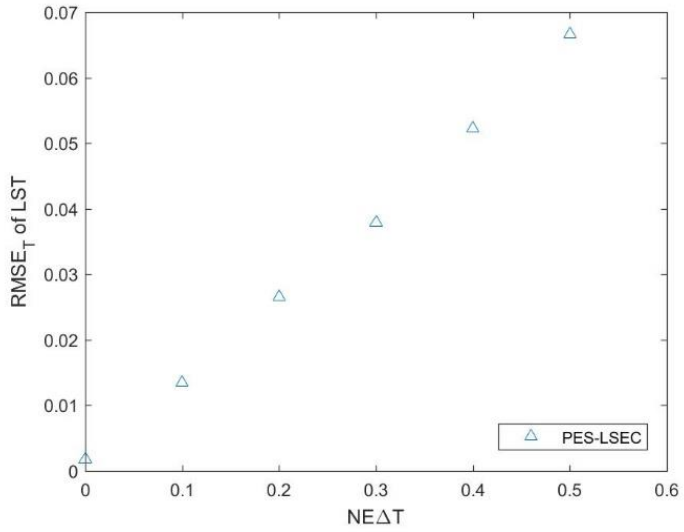

Figure 1. RMSE de LST avec la méthode PES-LSEC.

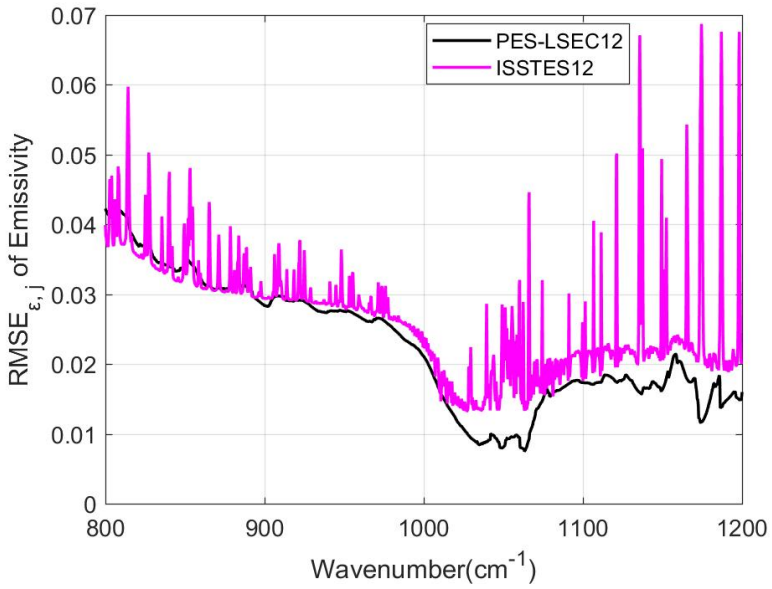

Figure 2. RMSE de LSE dans chaque bande pour la région 800–1200 cm^{-1}. La ligne noire est le résultat de l'extraction de la méthode PES-LSEC avec les facteurs d'échelle du profil d'humidité de 0.2. ISSTE12 présente le RMSE de l'émissivité dans chaque bande, en utilisant la méthode ISSTES avec les facteurs d'échelle du profil d'humidité de 0.2.

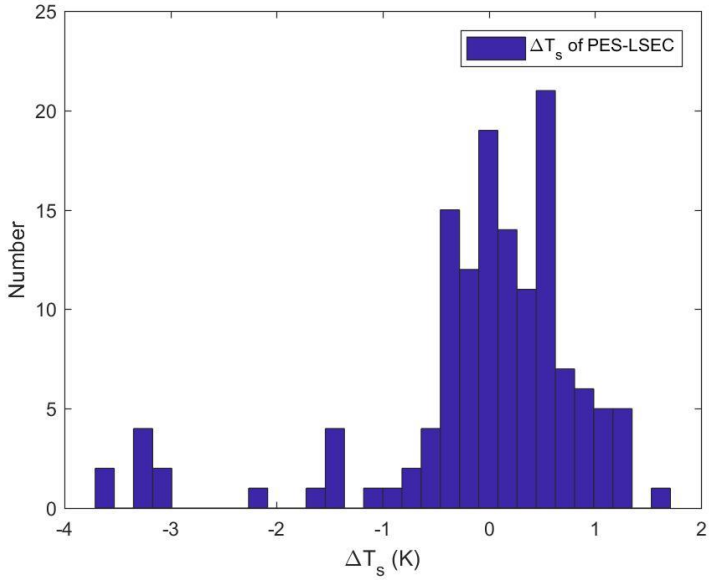

Figure 3. La différence entre la température récupérée et la température réelle avec la méthode PES-LSEC.

Dans le quatrième chapitre, un modèle de « deep learning » a été développé permettant de restituer directement la LST sans correction atmosphérique préalable à partir de données hyperspectrales de l'instrument IASI (l'interféromètre à sonde atmosphérique infrarouge). Ce modèle d'apprentissage est utilisé pour former et apprendre la relation entre les observations d'IASI (température de brillance) et la LST. Ce modèle de « deep learning » combine les avantages du réseau neuronal profond (DNN) et réseau neuronal convolutionnel (CNN) pour extraire les caractéristiques des données de formation avec le modèle de mémoire à court terme (Long Short-Term Memory : LSTM) pour la prédiction des séquences (Figure 4).

Le jeu de données de formation contient comme l'entrée du modèle les températures de brillance mesurées par l'IASI et fournit en la sortie la LST obtenue de l'AVHRR/MetOp (Advanced Very High Resolution Radiometer). L'ensemble des données s'étend de janvier 2016 à décembre 2018. Le modèle de « deep learning » ainsi construit a été appliqué aux autres observations réelles d'IASI pour estimer les LSTs. Les domaines de recherche sont l'Algérie et l'Afrique du Sud. Pour les deux domaines de recherche, 90% de l'ensemble de données a été

adopté comme données d'entraînement et les 10% restants ont été utilisé comme ensemble de données de test. La LST en Algérie et en Afrique du Sud a pu être restituée avec une précision <2 K et 2,5 K, respectivement, et validée avec l'ensemble de données de test (Figure 5). Cette procédure permet d'obtenir une bonne estimation de la LST.

Les données d'IASI de différentes saisons dans les deux régions sélectionnées (Afrique du Nord et du Sud avec une variété de couvertures de surface terrestre et de nombreux jours de ciel clair) sont utilisées pour valider ce modèle de restitution de la LST. Le RMSE de LST restituée par ce modèle sont de 3 K en comparant avec le produit LST de l'AVHRR/MetOp pour les zones sélectionnées. Les résultats indiquent que le modèle développé peut être utilisé pour déterminer la LST avec une bonne précision de 3 K. Par rapport à la méthode PSE-LSEC décrite dans le troisième chapitre, ce modèle ne nécessite aucune information atmosphérique.

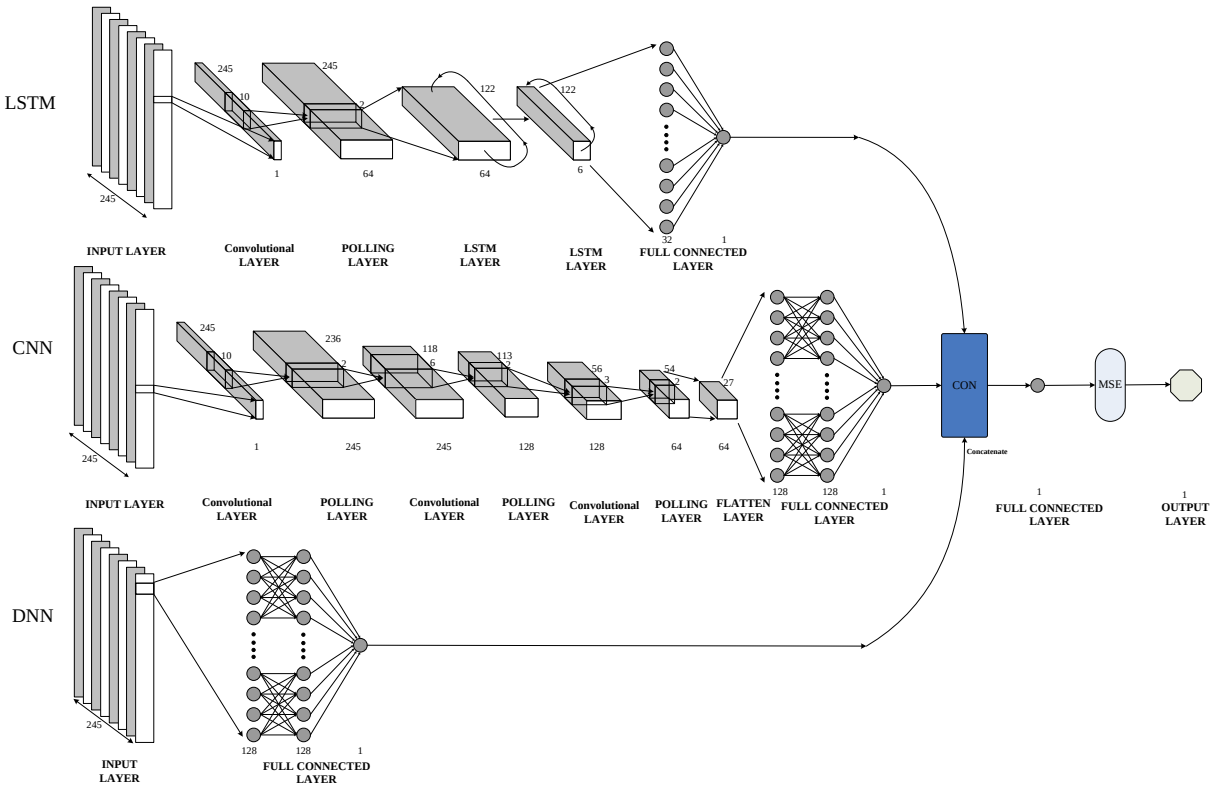

Figure 4. L'architecture du modèle d'apprentissage profond construit.

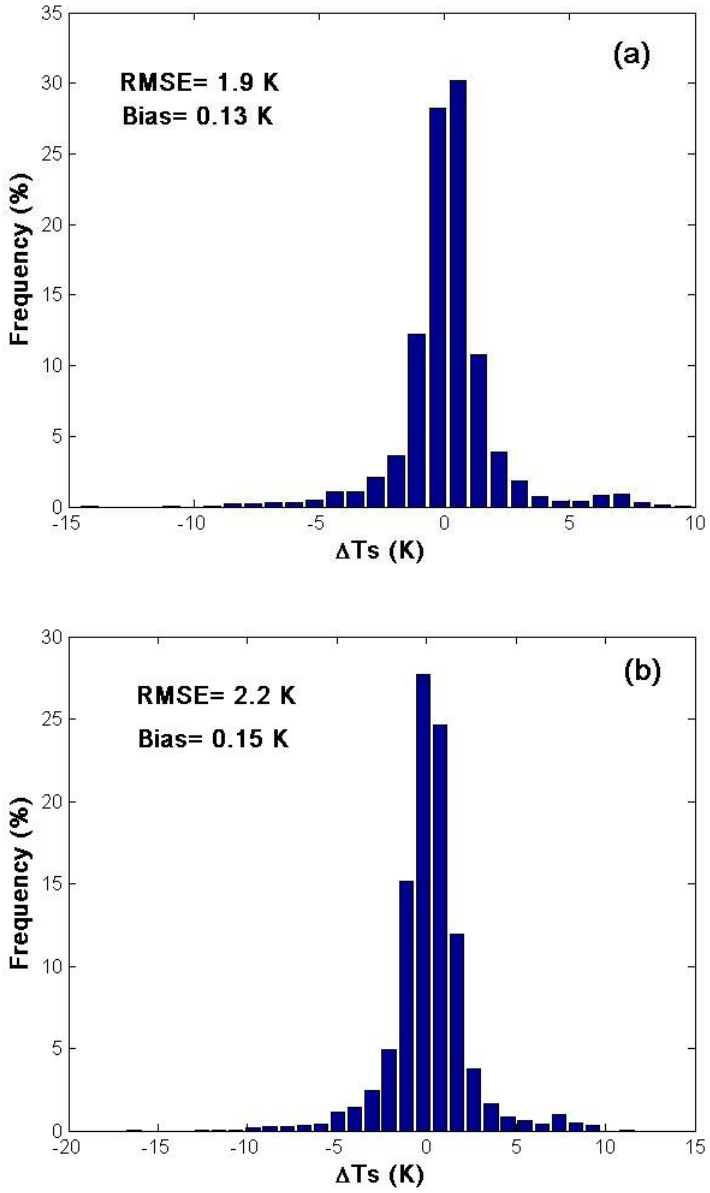

Figure 5. L'histogramme des résidus entre les valeurs récupérées à l'aide du modèle de mélange profond et les produits AVHRR / MetOp Daily LST. a) pour l'Afrique du Nord; (b) pour l'Afrique australe.

Le cinquième chapitre consiste à mettre au point une nouvelle méthode physique permettant de restituer la température de surface à partir de données hyperspectrales de l'instrument IASI sans correction atmosphérique. Cette méthode s'appuie sur la méthode de restitution physique en deux étapes (Ma et al., 2000) et tente une nouvelle forme simple pour re-linéariser l'équation de transfert radiatif (RTE). La RTE a été tangente linéaire autour des valeurs initiales de LST, LSEs, les températures équivalentes atmosphériques (Tas) et la teneur en vapeur

d'eau (q) dans l'atmosphère sans tenir compte de la structure verticale compliquée du profil atmosphérique. Le réseau de neurones artificiels est adopté pour obtenir les estimations initiales des LST, LSEs, Tas et q. La technique d'analyse en composantes principales (PCA) est utilisée pour réduire le nombre d'inconnues concernant les températures équivalentes atmosphériques (Tas) et les LSEs. La méthode de régularisation de Tikhonov et l'algorithme d'itération du principe de divergence sont utilisées pour stabiliser le problème mal posé et obtenir la solution finale de LST. De plus, un nouveau système de sélection des canaux a été proposé dans le but de donner une estimation précise de LST pour cette méthode physique. Dans cette étude, la sélection du canal spécifique varie dynamiquement en fonction de la valeur de poids LST de la matrice de poids calculée à partir de l'estimation initiale. Les canaux avec des poids LST plus élevés ont été sélectionnés.

Cet algorithme physique a été testé avec des données simulées et réelles du capteur IASI. L'écart type (RMSE) de LST obtenue par cette méthode physique à partir des données simulées est d'environ 1 K (Figure 6). L'analyse de sensibilité a montré que la restitution de LST peut être obtenue avec une erreur de 1 K si l'erreur aléatoire sur l'estimation initiale de LST est inférieure à 3 K, les erreurs relatives sur l'estimation initiale de Ta et q sont inférieures à 10% et 40%, respectivement et l'estimation initiale de LSEs est donnée comme une constante égale à 0.97. Avec les données simulées, les résultats ont montré que l'influence de l'estimation initiale des variables inconnues sur la restitution de LST est relativement faible et peut être négligée. Avec les données réelles de l'IASI acquises dans nos régions d'étude, en comparant avec les LSTs obtenues à partir des données AVHRR/MetOp, les LSTs peuvent être restituées par cette méthode physique avec une différence de 1.5 K (RMSE) de jour, et de 1 K de nuit. Ces valeurs montrent que la méthode proposée est capable de déterminer les LSTs avec une précision similaire à celle de l'AVHRR/MetOp.

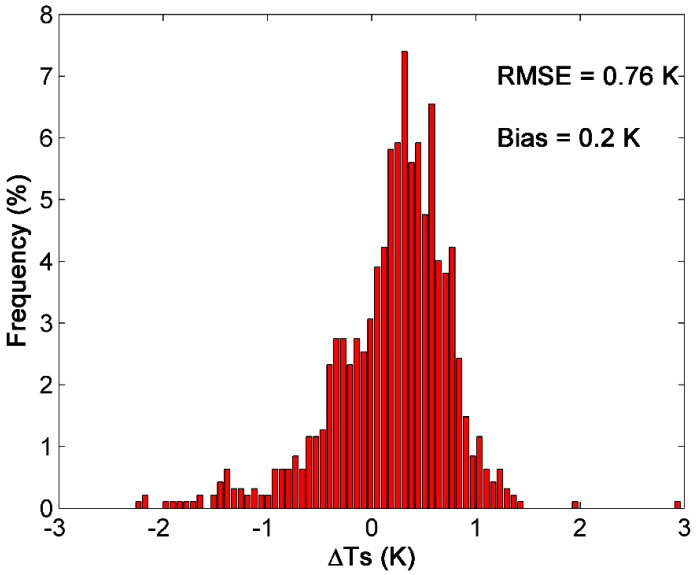

Figure 6. Histogramme des résidus entre LST restituées et LST réelles basés sur la méthode physique pour l'ensemble de données simulées.

Le sixième chapitre conclue les chapitres précédents et donne les perspectives de notre recherche. On peut conclure que les méthodes proposées dans cette thèse peuvent être utilisées pour restituer les LSTs à partir des données TIR hyperspectrales.

1) Avec une correction atmosphérique précise, la méthode PSE-LSEC peut fournir une bonne estimation de la LST. Elle fournit la tendance de base de LSE et détermine des positions de crête et de creux relativement précises, produisant un bon schéma de segmentation à intervalles irréguliers pour séparer la température et l'émissivité.

2) D'autre part, la méthode de « deep learning » et la méthode physique proposées peuvent donner l'estimation de LST sans aucune information préalable sur la surface terrestre et ni sur l'atmosphère. Ces deux méthodes présentent ainsi un réel avantage.

Pour les travaux futurs, prendre en compte l'angle d'observation devrait améliorer la validité de la méthode physique, développée et validée ici uniquement pour l'observation au nadir.

Content

List of Figures

List of Tables

Chapter 1. Introduction

1.1 Background

Land surface temperature (LST) is a key parameter in the physics processes of surface energy and water balance at regional through global scales (M. C. Anderson et al., 2008; Brunsell and Gillies, 2003; P. Dash et al., 2002; Jielun Sun and Mahrt, 1995; Vining and Blad, 1992). It has been used in many fields including climate change (Yu et al., 2007), hydrological (McCabe et al., 2008), ecological (Ryu et al., 2008), urban climate (Yuan and Bauer, 2007) and bio-geochemical (M C Anderson et al., 2008). Considering the complexity of LST, ground measurements cannot actually provide a wide range of values. With the development of remote sensing, satellite data offer the possibility for measuring LST over the earth with sufficiently high temporal resolution and complete spatially averaged rather than point values (Li et al., 2013).

The LST can be obtained with the satellite-based thermal infrared (TIR) data through the radiative transfer equation (RTE). There have been many algorithms for the extraction of surface temperature from multispectral TIR remote sensing data, and many achievements have been made. However, subject to the ill-conditioned equation itself, more assumptions are still required to accurately solve the surface temperature. At the same time, the multi-spectral sensor has a wide weight function, low vertical resolution, and few channels. The observation data commonly includes information of atmospheric temperature profile, surface temperature and emissivity, ozone, water vapor, methane and other trace gases. The small number of channels is also not conducive to the inversion of target LST information.

Hyperspectral TIR data with more refined spectral characteristics provide a great deal of information on land surface processes, especially land surface temperature (LST) (Prasanjit Dash et al., 2002). With a large number of channels, hyperspectral TIR can increase the stability of the equation system, and can also

provide more constraints for the separation of surface temperature and emissivity that better fit the true physical properties of the surface, such as spectral smoothing index (Borel, 1997, 1998), correlation index (Cheng et al., 2008), and thus can improve the retrieval accuracy of LST. Moreover, many hyperspectral infrared sensors onboard satellite provide data to further explore the land surface information, such as Atmospheric InfraRed Sounder (AIRS) (Aumann et al., 2003), the Infrared Atmospheric Sounding Interferometer (IASI) (Hilton et al., 2012) and the Cross-track Infrared Sounder (CrIS) (Bloom, 2001). These sensors provide us the opportunity to obtain the surface temperature, and many methods has been proposed to retrieve LST with hyperspectral TIR data. On the basis of existing research, hyperspectral TIR data information is further explored with the target of developing LST inversion models.

1.2 Research states

Nowadays, in the thermal infrared region, accurately retrieving LST, which is tightly coupled with land surface emissivity (LSE), is an ill-posed problem because the number of unknowns is larger than the number of equations (N spectral bands) according to the radiative transfer equation (RTE), even if an accurate atmospheric correction has been achieved. There are always N+1 unknows (N LSEs and one LST) for observing radiance in N bands (N equations). On the basis of this problem, many methods have been proposed to solve the underdetermined equations to separate the LST and LSE and obtain accurate solutions using hyperspectral TIR data.

The research of retrieval surface temperature and emissivity of the multi-spectral TIR remote sensing has laid to the foundation for the study of Hyperspectral TIR LST inversion. Therefore, we will firstly introduce the methods based on the multi-spectral TIR.

- Single-channel method

The single-channel method (Model emissivity method) (Hook et al., 1992) adopts the radiance measured by the satellite sensor in the single channel selected in the atmospheric window, and uses the atmospheric transmittance / radiance code that requires the input of the atmospheric profile to correct the remaining

atmospheric attenuation and radiance. Then LST can be calculated by the radiative transfer equation (RTE). It requires a premise that the LSE is well known or estimated in advance (Chedin et al., 1985; Mushkin et al., 2005; Ottlé and Vidal-Madjar, 1992; Price, 1983; Sobrino et al., 2004; Susskind et al., 1984).

- Split-window algorithm

Split-window algorithm (SW) was firstly proposed by McMillin in 1975 (McMillin, 1975). It doesn't need the synchronous atmospheric profile and only utilizes two adjacent channels centered at 11 and 12 μm to retrieve sea surface temperature (SST). Due to the success of the SW method in estimating SST from spatial measurements, many efforts have been made to extend the SW method to retrieve LST since the 1980s. They discussed the spatio-temporal and spectral variations of LSE, the large difference between LST and air temperature, the total column water vapor (WV) of the atmosphere and the observation zenith angle (VZA), etc., to optimize the SW algorithm and make it more suitable for the inversion of LST (Atitar and Sobrino, 2008; Becker, 1987; Becker and Li, 1990a; Coll et al., 1994; Prata, 1994; Price, 1984; Sobrino et al., 1996, 1994, 1991; Wan and Jeff, 1996). The SW algorithm can achieve higher retrieval accuracy and higher efficiency for some local land surfaces with known surface emissivity, and it has become a widely used surface temperature inversion method.

- Classification-based emissivity method (CBEM)

Classification-based emissivity method (CBEM) establishes the relationship between each surface type and LSE, and then specifies the corresponding type of surface emissivity on the basis of accurate land surface classification information (Snyder et al., 1998). However, the LSE determined by classification cannot accurately reflect the complex land surface types, especially the various types of surface with different geological origins. The emissivity is quite complex, and some errors in the emissivity will cause large retrieval error on temperature.

- NDVI-based emissivity method (NBEM)

This method discusses a statistical relationship between the NDVI derived from the VNIR bands and the LSE in the TIR channels (Van de Griend and OWE, 1993). It needs accurate atmospheric correction. Sobrino et al. (Sobrino et al., 2008)

found that this method lacked of continuity in the LSE values from soil type to vegetation type, because the LSE of these areas is calculated using different formulas.

- Day/night temperature-independent spectral-indices (TISI) method

This method uses the temperature power function of Planck's equation to approximate and express the radiance of a channel as the *nth* power of temperature. Based on this approximation, the ratio of the two channels can remove the temperature term to obtain the TISI index. The TISI index can be used to give the shape of emissivity (Becker and Li, 1990b).

- Two-temperature method (TTM)

The two-temperature method assumes that the LSE are time-invariant on the same day. If there are two observations during the day and night (2 N measurements), the unknows will be N+2 (N channel LSEs and two LSTs). The N LSEs and the two LSTs can be determined (N≥2) (Watson, 1992).

- Physics-based day/night operational method (D/N)

Wan and Li (Wan and Li, 1997) developed a physics-based LST algorithm for simultaneously retrieving surface band-averaged emissivities and temperatures from a combined use of the day/night pairs of MIR and TIR data. This method is based on the day/night TISI based method and TTM method. The statistical regression method and the least-squares fit method were adopted to solve the set of 14 nonlinear equations.

- Gray body emissivity method (GBE)

This GBE method assumes that the emissivity of ground objects in a certain two channels is equal, thereby reducing the number of unknowns to solve the equation. The ill-posedness of the equation formed by two adjacent channels and the assumption that the emissivities of the two channels are equal may be unreliable in actual situations, which makes the method less practical. However, the GBE method is thought to be more applicable to hyperspectral TIR data (Barducci and Pippi, 1996).

- Temperature emissivity separation method (TES)

The TES method (Alan Gillespie et al., 1998) used for Advanced Spaceborne Thermal Emission and Reflection Radiometer (ASTER) data is composed of three modules, namely: normalized specific emissivity (NEM) module, specific emissivity ratio (SR) module and MMD module. It first uses NEM to obtain the estimated surface temperature, then uses SR to obtain the shape of the specific emissivity spectrum, and finally uses MMD to obtain the true value of the specific emissivity. In actual operation, these three steps are an iterative process, and the temperature and specific emissivity are finally obtained.

With the development of hyperspectral thermal infrared study, how to accurately retrieve LST using hyperspectral infrared data is widely discussed. Some indoor or ground-based experiments made great efforts to separate the surface temperature and emissivity for hyperspectral data. 'Planck draping' method (A. Gillespie et al., 1998) thinks that the accurate temperature can give the best fit of the Planck's function to the measured spectra with the assumption that the maximum emissivity is 0.97. Minimize the residual atmospheric emission lines (Balick et al., 2008; Horton et al., 1998) presents a method in which the sample temperature is varied to minimize the residual atmospheric emission lines in the measured field emissivity spectra. With the control of temperature using the heating source, the downwelling radiance is a critical parameter in calculating the emissivity. The non-negative matrix factorization provides an unsupervised linear representation of the data similar to principal component analysis (PCA) by using non-negative coefficients in the calculation of eigenvalues, thus it is widely adopted to determine the downwelling radiance and further calculate the emissivity (Balick et al., 2008; Hubbard et al., 2018; Yousefi et al., 2018).

Nowadays, many methods have been developed to acquire the LST information. After the accurate atmospheric correction, the temperature–emissivity separation (TES) methods commonly add physical constraint to obtain the accurate LST or reduce the numbers of unknows to make the underdetermined problem solvable using data dimensionality reduction technology.

- The iterative spectrally smooth (ISSTES) method

The iterative spectrally smooth (ISSTES) method (Borel, 1998)(Borel, 2008)(Borel, 2003)(Borel, 1997) defined the smoothness for the calculated

emissivity to find the accurate LST because the error of LST will cause the calculated LSE remaining the characteristic of atmospheric emission lines. The iterative spectrally smooth temperature and emissivity separation (ISSTES) algorithm is commonly used based on the assumption that the emissivity spectrum is smoother than the atmospheric spectrum in hyperspectral TIR data.

To avoid the singular value problem of ISSTES method, downwelling radiance residual index (DRRI) (Wang et al., 2008)(Ouyang et al., 2013) was defined to describe the direction and magnitude of the downwelling radiance residual feature with some well-chosen channel groups. Correlation-based temperature and emissivity separation (CBTES) algorithm (Cheng et al., 2008) and stepwise refining temperature and emissivity separation (SRTES) algorithm (Cheng et al., 2010) discuss the relationship between the surface emissivity, surface self-emission and atmospheric downward radiance to optimize surface temperature, and further obtain LSE with this surface temperature.

- Linear emissivity constraint temperature emissivity separation method (LECTES).

LECTES method (Wang et al., 2011) divides emissivity spectrum into some segments with a linear function in each section. This method is via descending dimension of N channels emissivity, thus reducing the number of the unknowns. It successfully turns the underdetermined problem into an overdetermined problem, making the temperature-emissivity separation solvable.

The method is based on the following equations:

$$L_m(\lambda) = L_{sur}(\lambda)\tau(\lambda) + R_{up}(\lambda) \tag{1.1}$$

$$L_{sur}(\lambda) = \varepsilon(\lambda)B(\lambda, T_s) + (1 - \varepsilon(\lambda))R_{down}(\lambda) \tag{1.2}$$

Where, $L_m(\lambda)$ is the at-sensor radiance at wavelength λ, $L_{sur}(\lambda)$ is the at-ground radiance, ε is the LSE, R_{up} is the atmospheric upwelling radiance, R_{down} is the atmospheric downwelling radiance, $B(\lambda, T_s)$ is the Planck function of surface temperature T_s, and τ is the atmospheric transmittance.

When the atmospheric correction has been done, τ, R_{up} and R_{down} are known. In order to make equations solvable, LSE is approximated as a piecewise linear function (M sections), in one segment, the emissivity can be expressed as:

$$\varepsilon(\lambda_i) \approx a_k \lambda_i + b_k \tag{1.3}$$

Where the a_k and b_k are the two sets of coefficients of the M linear functions, $M \leq N/3$. Combining Eq.1.2 with Eq.1.3, we can obtain:

$$F_L = F_B(T) \begin{bmatrix} a \\ b \end{bmatrix} \tag{1.4}$$

Where,

$$F_L = \begin{bmatrix} L_{sur}(\lambda_1) - R_{down}(\lambda_1) \\ \dots \\ L_{sur}(\lambda_m) - R_{down}(\lambda_m) \end{bmatrix},$$

$$F_B(T) = \begin{bmatrix} \lambda_1[B(\lambda_1, T_s) - R_{down}(\lambda_1)] & B(\lambda_1, T_s) - R_{down}(\lambda_1) \\ \dots & \dots \\ \lambda_m[B(\lambda_m, T_s) - R_{down}(\lambda_m)] & B(\lambda_m, T_s) - R_{down}(\lambda_m) \end{bmatrix}$$

Eq.1.4 is overdetermined and solvable because equations are more than the unknowns (N equations in this system, 2 M+1 unknowns). To solve the overdetermined equations which is difficult to obtain the specific analytical solution, an iterative solution process is required. The cost function E is defined using the sum of the squares of the estimated at-ground radiance and the actual one (Eq.1.5):

$$E = \sum_{i=1}^{N} (\langle L_{sur}(\lambda_i) \rangle - L_{sur}(\lambda_i))^2 \tag{1.5}$$

In the iterative process, coefficients of a and b are firstly calculated according to the at-ground radiance and atmospheric downwelling radiation under an estimated reference temperature T_s' to restore the entire LSE. The value of a and b can be calculated using the least squares method when a reference temperature T_s' is given (Eq.1.6):

$$\begin{bmatrix} a \\ b \end{bmatrix} = (F_B(T_s')^T F_B(T_s'))^{-1} F_B(T_s')^T F_L \tag{1.6}$$

Substituting the obtained coefficients into Eq.1.3, estimated LSE at a given temperature (T_s') is calculated. Then, T_s' and the estimate LSE are substituted into the Eq.1.5. According to the Newton iteration method, the temperature estimation change δT is obtained to update T_s'(Eq.1.7):

$$T_s^{k+1} = T_s^k + \delta T_k \tag{1.7}$$

When δT is small enough, it can be considered that the estimated temperature ${T_s}^{k+1}$ at this time is the final retrieval temperature, also regard the corresponding LSE spectrum as retrieval result.

- Artificial neural network (ANN) method.

Many methods present good retrieval accuracy of LST with accurate atmospheric correction, many analyses have been presented in related experiment as mentioned above. However, obtaining accurate atmospheric parameters synchronously with TIR measurements is very difficult, artificial neural network (ANN) method (Aires et al., 2001)(Aires et al., 2002)(Wang et al., 2013) gives solutions to obtain LST without accurate atmospheric correction for hyperspectral thermal infrared data.

Eq.1.1 and Eq.1.2 showed that the at-sensor radiance had a non-linear relationship with the LST. ANN method can learn complex patterns, generalization to noisy environments, and incorporation of both known ANN method ledge and physical constraints (Mas and Flores, 2008). Wang (Wang et al., 2013) applied the ANN method to provide the estimation of LST, LSE and atmospheric profiles. The result showed that there was a 5 K bias between our retrieved LST and the IASI LST Level 2 products.

- Two-step physical retrieval method (TSRM).

The physical simultaneous retrieval methods (Li et al., 1994)(Li et al., 2007)(F. Aires et al., 2002a)(F. Aires et al., 2002b)(Ma et al., 1999)(Ma et al., 2002)(Paul et al., 2012)(Masiello and Serio, 2013) provide some solutions to obtain the LST information. The two-step physical retrieval method (Ma et al., 2002, 2000) is the most representative method and can be described as following:

If we ignore the influence of atmospheric scattering and the sun, to simplify the description, ignoring the wavelength and angle, the RTE can be expressed as (Li et al., 1994; Ma et al., 1999):

$$R = \varepsilon B_s \tau_s - \int_0^{P_s} B d\tau + (1-\varepsilon) \int_0^{P_s} B d\tau^* \tag{1.8}$$

Where R is at-sensor radiance, B is the Planck function of surface temperature, B_s represents the blackbody radiance of the surface temperature. τ is the total

transmittance of the atmosphere above the pressure level p, P_s is surface pressure, ε is emissivity, τ^* indicates the transmittance in the path of reflected radiation.

The first order variation of Eq.1.8 yields

$$\delta R = \varepsilon\tau_s\delta B_s + \left(B_s\tau_s - \int_0^{P_s} B d\tau^*\right)\delta\varepsilon + \varepsilon(B_s - B_a)\delta\tau_s - \int_0^{P_s}\delta B[d\tau - (1-\varepsilon)d\tau^*] + \int_0^{P_s}\delta\tau\, dB - (1-\varepsilon)\int_0^{P_s}\delta\tau^* dB \quad (1.9)$$

If we ignore the deviation of the natural broading of absorbing coefficient of *ith* absorbing constituent relative to that associated with the "guess" atmospheric condition, we have:

$$\tau_w = e^{-\int_0^P g^{-1}k_w q_w dp} \quad (1.10)$$

$$\delta\tau = \tau_w\delta\tau_d + \tau_d\delta\tau_w \approx \tau_d\delta\tau_w = \tau\delta ln\tau_w = \tau\int_0^P \delta lnq_w dln\tau_w \quad (1.11)$$

Where, τ_w is water vapor transmittance, τ_d is dry air transmittance, k_w is absorbing coefficient of water vapor, g is gravitational acceleration, q_w is water vapor content.

Substituting Eq.1.11 into Eq.1.9, we obtain:

$$\delta T_b = W_{T_s}\delta T_s + W_\varepsilon\delta\varepsilon + \int_0^{P_s} W_T\delta T dp + \int_0^{P_s} W_{q_w}\delta lnq_w dp \quad (1.12)$$

Where, T_b is the brightness temperature, T_s is surface temperature.

Eq.1.12 can be expressed as a matrix form:

$$Y = WX \quad (1.13)$$

Where,

$$W = \begin{pmatrix} W_{T_s} \\ W_\varepsilon \\ W_T \\ W_{q_w} \end{pmatrix}, X = \begin{pmatrix} \delta T_s \\ \delta\varepsilon \\ \delta T \\ \delta lnq_w \end{pmatrix}, Y = (\delta T_b)$$

The linearization of the radiation transfer equation is the basic step in the inversion of atmospheric profiles. After linearization, the radiance measured by satellites can be expressed as a linear function of surface temperature, emissivity, and atmospheric temperature and humidity profiles. The principle component-analysis (PCA) technique (Singh, 1993) is used to reduce the number of unknowns for atmospheric temperature, humidity profile and LSEs. The Tikhonov regularization method (Tikhonov and Arsenin, 1977) and the discrepancy principle iteration algorithm (Huang and Li, 2000) are employed to stabilize the ill-posed

problem and obtain the final maximum likelihood solution of the LST with the regularized solution as the initial guess.

1.3 Objectives

Our research adopts hyperspectral infrared data as the main source information and takes surface temperature retrieval as the main research goal to carry out corresponding work with the support of the radiation transfer model and the database of atmospheric profiles and surface emissivity. This study will pay more attention to the following:

（1）Atmospheric correction is a key issue for the retrieval of land surface temperature. Accurate atmospheric profiles are usually unavailable synchronously with TIR measurements, and thus the accuracy of the retrieved LST and LSEs can be degraded. We firstly assumed that atmospheric correction has been completed and we developed a method for separating surface temperature and emissivity based on the LSEC method. The simulation data is used to conduct a comprehensive system sensitivity and accuracy analysis for the proposed algorithm, then we use the ground measurement data to verify the proposed algorithm.

（2）A deep mixture model that can estimate LST without any known atmospheric information for IASI hyperspectral data is developed. This part attempts deep learning techniques to provide LST estimation. The proposed model will be validated with the IASI observations in different seasons.

（3）A physical method is developed to retrieve land surface temperature (LST) for IASI sensor observations. It will attempt a new form to re-linearize RTE to retrieve LST without considering the vertical structure of atmospheric profile using IASI sensor data. In this method, the channel selection is a key issue making the LST inversion accurate. Meanwhile, constructing a multi-layer perceptron neural network model to give the good initial value of the inversion is necessary. Finally, physical constraints are used to reduce the number of parameters to be inversed, and the iterative solution to the linearized radiation transfer equation is

used to obtain the final inversion results. The established model is verified and evaluated with both simulated and real data from the IASI sensor.

1.4 Organization of the thesis

This thesis is composed of six chapters.

For the first chapter, the background of retrieval LST for hyperspectral data is introduced. The review of research states about the LST retrieval method for multispectral and hyperspectral thermal infrared data is also presented in this part.

The second chapter introduces the concepts about the electromagnetic radiation mentioned in our thesis especially the atmospheric radiative transfer theory. Meanwhile, the satellite datasets, atmospheric profile database, emissivity library and atmospheric radiative transfer model used in this thesis are introduced.

The third chapter is devoted to present a proposed temperature and emissivity separation method for hyperspectral thermal infrared data with accurate atmospheric correction. The sensitivity analysis with the simulated dataset and validation with in-situ measurements will be performed.

The fourth chapter is devoted to explore a deep mixture model to provide the LST estimation for satellite level with the IASI brightness temperature product and AVHRR/MetOp LST product. Different regions in different seasons are chosen to validate the retrieval method.

The fifth chapter describes a physical method to retrieve surface temperature for the IASI observations without accurate atmospheric correction. This physical algorithm was tested with both simulated and real data from the IASI sensor.

The sixth chapter makes a conclusion to the previous chapters.

Chapter 2. Basic concepts, models and datasets

2.1 Concepts about electromagnetic radiation

2.1.1 Concepts about electromagnetic radiation

1) Wavelength

Wavelength is the distance that a wave propagates in a vibration period, that is, the distance between two adjacent points of the same phase (such as peaks or troughs) along the wave propagation direction, which is expressed by λ. Commonly used units of wavelength are meters (m), centimeters (cm), millimeters (mm), micrometers (μm), nanometers (nm), etc. The common unit of wavelength is the micrometer (μm) for infrared radiation. Meanwhile, the wavenumber (generally expressed as ν) in the infrared band is often used. Wavenumber refers to the number of wavelengths contained in a unit length in the wave propagation direction, that is, the reciprocal of the wavelength (1/λ). The most common unit of wave number is cm^{-1}. If the wavelength is in unit of μm and the wavenumber is in unit of cm^{-1}, then they satisfy the following relationship:

$$\nu \cdot \lambda = 10000 \tag{2.1}$$

2) Solid angle

The directivity of the radiation field can be described by the solid angle, which is an extension of the two-dimensional angle measurement. The solid angle is defined as theratio of the surface area of a sphere with a sphere radius of r intercepted by a cone to the square of the sphere radius. The symbol is Ω, and the unit is spherical degree (sr). As shown in Fig. 2.1:

$$\Omega = A/r^2 \tag{2.2}$$

Where, A is the area of a small face element perpendicular to the radius of the sphere, and r is the distance between the center and the upper face element of the sphere, that is, the radius of the sphere.

The differential of a solid angle can be expressed as:

$$d\Omega = \frac{dA}{r^2} = sin\theta d\theta d\varphi \tag{2.3}$$

θ and φ are zenith angle and azimuth angle in polar coordinates, respectively (Fig.2.2).

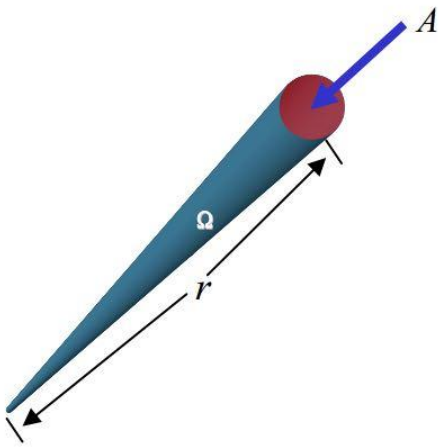

Fig.2. 1. Conceptual illustration of solid angle.

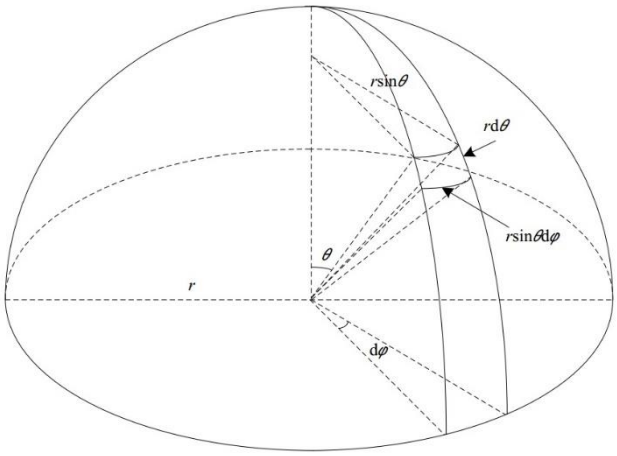

Fig.2. 2. Differentiation of solid angle.

3) Radiance energy

Energy transmitted outward in the form of electromagnetic waves. It is commonly expressed by Q and the unit is joule (J).

4) Radiant flux

The radiant energy that passes through a surface in a unit of time is called the radiant flux through that area. The symbol is ϕ and the unit is $J \cdot s^{-1}$.

$$\phi = dQ/dt \tag{2.4}$$

5) Radiance exitance

Radiation energy radiated from a unit area by a surface radiation source in a unit time. That is, the radiation flux per unit area of the surface radiation source. The symbol is M and the unit is W/m^2.

$$M = d\phi/dA \tag{2.5}$$

6) Irradiance

The radiation energy received by a surface radiation source from a unit area in a unit time, that is, the radiation flux irradiated on the unit area of the object. The symbol is E, the unit is W/m^2.

$$E = d\phi/dA \tag{2.6}$$

7) Radiant intensity

The radiant flux gives out by a point radiation source in a direction per unit solid angle per unit time. The symbol is I, the unit is W/sr.

$$I = d\phi/d\omega \tag{2.7}$$

8) Radiance

Radiance is the radiant flux of a surface radiation source in unit projection area and unit solid angle. The symbol is L, the unit is $W/m^2/sr$.

$$L = d^2\phi/d\omega dA cos\theta \tag{2.8}$$

9) Reflection

When the electromagnetic radiation energy reaches the interface between two different media, the phenomenon that part or all of the incident energy returns to the original media is called reflection. The ratio of the reflected energy to the

incident energy is called the spectral reflectance, referred to as reflectance, which is expressed by $\rho(\lambda)$, and its value is between $0-1$.

10) Transmission

The phenomenon that electromagnetic radiation continues to propagate through the medium is called transmission. The ability of a medium to transmit energy is defined as transmittance (τ), it is defined as the ratio of the electromagnetic radiation energy that passes through an object to the incident energy. Transmittance is a function of wavelength.

11) Absorption

The electromagnetic radiation exchanges energy with the material in the medium, and the electromagnetic energy is converted into heat energy or other forms of energy in the medium. This phenomenon is called absorption. The ability of a medium to absorb electromagnetic radiation can be expressed by absorptance (a), which refers to the ratio of the electromagnetic radiation energy absorbed by an object to the incident energy. Absorbance is a function of wavelength.

The law of conservation of energy imposes:

$$\rho(\lambda) + \tau(\lambda) + a(\lambda) = 1 \tag{2.9}$$

12) Kinetic temperature

Kinetic temperature characterizes the average thermal energy of molecules in the object. The Kinetic temperature of an object can be obtained by placing a temperature measuring instrument (mainly a thermometer) directly on the object or buried in the object (Becker and Zhao-Liang Li, 1995).

13) Radiant temperature

From the physical point of view, the radiant temperature only indicates the surface temperature or skin temperature of the object. The "temperature" mentioned in this work refers to the radiant temperature rather than the Kinetic temperature without other explanations.

14) Brightness temperature

The brightness temperature of an object (Tb) refers to the temperature of the blackbody radiating the same radiation energy as the observed object, that is, the equivalent blackbody temperature.

$$Tb(\lambda) = B_{\lambda}^{-1}(R_{\lambda}(T)) \tag{2.10}$$

where $Tb(\lambda)$ is brightness temperature of the observed object, T is the radiant temperature of the observed object, R is the observed spectral radiance, B is the Planck's function.

2.1.2 Electromagnetic radiation theory

1) Planck's law

Planck's law describes the spectral density of electromagnetic radiation emitted by a blackbody in thermal equilibrium at a given temperature T, when there is no net flow of matter or energy between the body and its environment. $B(\lambda, T)$ is the Planck function at surface temperature T at wavelength λ (Eq.2.11):

$$B(\lambda, T) = \frac{C_1 \lambda^{-5}}{\exp(C_2/\lambda T) - 1} \tag{2.11}$$

Where, the unit of $B(\lambda, T)$ is $W/(m^2 \cdot sr \cdot \mu m)$. The unit of λ and T are μm and K, respectively. C_1=1.191× 10^8 $W \cdot \mu m^4/(sr \cdot m^2)$ and C_2=1.4388× 10^4 $\mu m \cdot K$.

In thermal infrared remote sensing, the wavenumber v is commonly used to describe the spectral range. Therefore, the Planck function can also be expressed as the following equation:

$$B(v, T) = \frac{C_3 v^3}{\exp(C_4 \cdot v/T) - 1} \tag{2.12}$$

Where, the unit of $B(v, T)$ is $W/(m^2 \cdot sr \cdot cm^{-1})$. The unit of v is cm^{-1}. C_3=1.191× 10^{-8} $W/(m^2 \cdot sr \cdot cm^{-4})$ and C_2=1.4388 $cm \cdot K$.

2) Stefan-Boltzmann's law

Stefan-Boltzmann's law describes the power radiated from a blackbody in terms of its temperature. As the radiant temperature of the blackbody increases, the radiated total energy will increase rapidly. The total radiant exitance (M) of the black body has the following quantitative relationship with the blackbody surface temperature (T):

$$M(T) = \sigma \cdot T^4 \tag{2.13}$$

Where, σ is the Stefan–Boltzmann constant: $\sigma = 5.6697 \times 10^{-8}\ W/(m^2 \cdot K^4)$.

3) Wien's displacement law

Wien's displacement law describes the quantitative relationship between the peak wavelength and temperature of blackbody radiation:

$$\lambda_{max} = \frac{b}{T} \tag{2.14}$$

λ_{max} is the wavelength position with the largest spectral radiance, the unit is μm. b is a constant and equal to 2897.8 $\mu m \cdot$ K.

Wien's displacement law shows that the wavelength corresponding to the maximum radiation intensity of a blackbody is inversely proportional to the absolute temperature of the blackbody. The peak wavelength of the radiation of the 300 K (the temperature of the earth's surface is around this value) blackbody is about 9.7 μm, and the peak wavelength of the radiation of the 6000 K (the temperature of the sun's surface is around this value) blackbody is about 0.48 μm.

4) Kirchhoff's law

Under thermal equilibrium conditions, the radiant exitance $M(\lambda, T)$ of any object is proportional to its absorption $\alpha(\lambda, T)$. The proportionality coefficent ($E(\lambda, T)$) is a universal function, depending on wavelength and temperature:

$$\frac{M(\lambda, T)}{\alpha(\lambda, T)} = E(\lambda, T) \tag{2.15}$$

Kirchhoff's law shows that radiative emission capability increases with the increase of absorption of an object. The ratio of the radiant exitance of an object to the radiant exitance of a blackbody at the same temperature is usually defined as the emissivity of the object:

$$\varepsilon(\lambda,T)=\frac{M(\lambda,T)}{E(\lambda,T)} \tag{2.16}$$

For the material in thermodynamic equilibrium, α is equal to its effective emissivity ε. Meanwhile, natural surface is assumed to be opaque ($\tau=0$) in thermal infrared remote sensing, we can get:

$$\rho(\lambda)+\varepsilon(\lambda)=1 \tag{2.17}$$

2.1.3 Atmospheric radiative transfer theory

2.1.3.1 Interaction of electromagnetic radiation and atmosphere

The upper atmosphere (such as the atmosphere above 100 km) has little effect on the transmission of the electromagnetic radiation in the spectral regions frequently used for remote sensing. The lower atmosphere has a greater impact on it. The interaction of electromagnetic radiation with the atmosphere mainly follows two basic physical processes: scattering and absorption.

The phenomenon that electromagnetic radiation changes the direction of propagation due to the influence of particles in the atmosphere (atmospheric molecules or aerosols) is atmospheric scattering. The scattering intensity depends on the size and content of particles, the wavelength of electromagnetic radiation, the thickness of radiation propagating through the atmosphere, etc. In the case of 8-14 μm TIR remote sensing applications, under clear sky conditions, the scattering effect of the atmosphere is very small and is generally negligible.

When electromagnetic radiation passes through the atmosphere, in addition to scattering, it is also absorbed by atmospheric molecules. Atmospheric absorption also attenuates the energy of electromagnetic radiation in the direction of propagation. There are three atmospheric molecules that have the most obvious

absorption of electromagnetic radiation from visible to infrared: (a) Water vapor. The absorption radiation of water vapor is larger than other atmospheric components. The most important absorption bands are in the range of 2.5 ~ 3.0μm, 5.5 ~ 7.0μm and > 27.0μm; (b) Carbon dioxide. Carbon dioxide has strong absorption bands around 2.7, 4.3, and 14.5 μm; (c) Ozone. Ozone has a strong absorption band in the ultraviolet region from 0.22 to 0.32μm, and a strong absorption band (near 9.6μm) in the thermal infrared region.

Considering the combined effects of various gas absorptions, the absorption of the atmosphere is weak, and the atmospheric transmittance is high in some wavebands. These wave band regions that enable electromagnetic radiation energy to pass through are called "atmospheric windows." In the visible-infrared spectrum, the main atmospheric windows include: 0.3 ~ 1.3μm, 1.5 ~ 1.8μm, 2.0 ~ 2.6μm, 3.0 ~ 4.2μm, 4.4 ~ 5.0μm, 8 ~ 14μm, etc.

In the thermal infrared atmospheric window of 8 ~ 14μm, the atmosphere weakens the radiation on one hand, but also emits radiation itself, sometimes the radiation emitted exceeds the radiation absorbed by it. The influence of the atmosphere on the ground thermal radiation will depend on the combined effects of atmospheric absorption and atmospheric emission under specific atmospheric conditions of observation. Gas molecules and suspended particles in the atmosphere will absorb the radiation emitted by ground objects, resulting in a reduction of the energy from the ground to the on-board sensor. On the other hand, gas molecules and suspended particles in the atmosphere can also emit thermal radiation, superimposed on the ground thermal radiation signal, resulting in increased thermal radiation energy received by the on-board sensor. The two processes, whichever is more dominant, will have completely different results. In most cases, the emission of the atmosphere is not sufficient to compensate for its absorption of the surface radiation. At this time, the temperature of the radiation observed by the sensor will be lower than the brightness temperature of the surface. In a few cases, the emission of the atmosphere exceeds its absorption of the surface

radiation. Then, the temperature of the radiation observed by the sensor will be higher than the brightness temperature of the surface.

2.1.3.2 Schwarzschild's Equation

The radiation in the medium transmission will be weakened due to its interaction with the scattering and absorption of substances. Assuming that the radiation intensity I_λ becomes $I_\lambda + dI_\lambda$ after passing through the thickness of d_s in the direction of propagation, then:

$$dI_\lambda = -I_\lambda \rho k_\lambda d_s \tag{2.18}$$

Where, ρ is the density of the medium, k_λ is the mass extinction coefficient.

Besides, the radiation intensity is also enhanced by the emission of radiation and multiple scattering of radiation by the medium. The source function coefficient j_λ is defined to have the same physical meaning as the mass extinction cross section, then the enhanced part of the radiation intensity can be expressed as:

$$dI_\lambda = \rho j_\lambda d_s \tag{2.19}$$

The change of radiation intensity is:

$$dI_\lambda = \rho j_\lambda d_s - I_\lambda \rho k_\lambda d_s \tag{2.20}$$

Define the source function coefficient j_λ as:

$$J_\lambda = j_\lambda / k_\lambda \tag{2.21}$$

Then, Eq.2.20 can be written as:

$$\frac{dI_\lambda}{\rho k_\lambda d_s} = -I_\lambda + J_\lambda \tag{2.22}$$

The effect of atmospheric scattering is usually not considered in thermal infrared remote sensing. When a beam passes through a medium that is in local thermal equilibrium, two processes of absorption and emission occur

simultaneously. Then, the source function defined by (Eq.2.21) is given by the Planck function, expressed as:

$$J_\lambda = B(\lambda, T) \tag{2.23}$$

The radiative transfer equation can be written as:

$$\frac{dI_\lambda}{\rho k_\lambda d_s} = -I_\lambda + B(\lambda, T) \tag{2.24}$$

Multiplying (Eq.2.24) with the factor $k_\lambda \rho ds$, and integrating the thickness ds from 0 to s_1, we can get:

$$I_\lambda(s_1) = I_\lambda(0) e^{-\rho s_1 k_\lambda} \rho j_\lambda d_s + \int_0^{s_1} B[\lambda, T(s)]\, e^{-\rho s k_\lambda} k_\lambda \rho ds \tag{2.25}$$

The first term of the equation represents the radiation attenuation with the medium, and the second term represents the contribution of the medium emission along the entire path. (Eq.2.24) was proposed by Schwarzschild in 1914 in the category of Kirchhoff's law, and the integral solution under the condition of no scattering was derived, so it is also known as the Schwarzschild equation (Liou, 2002).

Here, we define the transmittance of the spectrum from path s to s_1 as:

$$\tau_\lambda(s, s_1) = e^{-\int_s^{s_1} k_\lambda \rho ds} \tag{2.26}$$

2.1.3.3 Radiative transfer equation

Because the atmosphere is not completely transparent, the infrared radiation received by the sensor includes both surface and atmospheric information. Under cloudless conditions, the atmosphere below the troposphere is regarded as the local heat balance. Assuming that the atmosphere is uniform and isotropic, without considering the scattering effect of the atmosphere, the radiance reaching the top of the atmosphere at a certain angle can be expressed as:

$$
\begin{aligned}
L(\lambda,\theta,\varphi) = \varepsilon(\lambda,\theta,\varphi)B(\lambda,T_s)\tau(\lambda,\theta,\varphi,p_s) &+ \int_{P_s}^{0} B\left(\lambda,T_p\right)\frac{\partial\tau(\lambda,\theta,\varphi,p)}{\partial p}dp \\
&+ \int_0^{2\pi}\int_0^{\frac{\pi}{2}} \rho(\lambda,\theta,\varphi,\theta',\varphi')\,L_d(\lambda,\theta',\varphi')\tau(\lambda,\theta,\varphi,p_s)cos\theta' sin\theta' d\theta' d\varphi' \\
&+ \int_0^{2\pi}\int_0^{\frac{\pi}{2}} \rho(\lambda,\theta,\varphi,\theta',\varphi')\,L_d(\lambda,\theta',\varphi')\tau(\lambda,\theta,\varphi,p_s)cos\theta' sin\theta' d\theta' d\varphi' \\
&+ \rho(\lambda,\theta,\varphi,\theta_s,\varphi_s)L_{sun}(\lambda,\theta_s,\varphi_s)\tau(\lambda,\theta_s,\varphi_s,p_s)\tau(\lambda,\theta,\varphi,p_s)
\end{aligned}
\tag{2.27}
$$

where $\theta,\varphi,\theta_s,\varphi_s$ are the viewing zenith angle and azimuth angle of the observation and the sun. θ' and φ' are the zenith angle and azimuth angle of downwelling direction of atmospheric radiance, respectively. L is the measured spectral radiance at the top of the atmosphere (TOA). p_s is the surface pressure level. τ is the atmospheric transmittance from a pressure level to the TOA along the viewing angle. T_p is the atmospheric temperature. ρ is the surface bidirectional reflectance.

The first item on the right represents the surface emission radiation that reaches the top of the atmosphere attenuated by the atmosphere; the second term represents the upward radiation of the atmosphere; the third item represents the downward atmospheric radiation item that reaches the top of the atmosphere through surface reflection; the last item is solar radiation that reaches the top of the atmosphere through surface reflection. In the thermal infrared region, the reflected solar radiation term can be ignored. Assuming the surface as a Lambertian reflector, $\rho = (1-\varepsilon)/\pi$ is also substituted into Eq.2.27. $\frac{1}{\pi}\int_0^{2\pi}\int_0^{\frac{\pi}{2}} L_d(\lambda,\theta',\varphi')\,cos\theta' sin\theta' d\theta' d\varphi'$ is atmospheric downwelling radiance, it is written as $R_{down}(\lambda)$.

$\tau(\lambda,\theta,\varphi,p_s)$ is written as $\tau(\lambda)$.

$L(\lambda,\theta,\varphi)$ is expressed as $L_m(\lambda)$.

$\int_{P_s}^{0} B\left(\lambda,T_p\right)\frac{\partial\tau(\lambda,\theta,\varphi,p)}{\partial p}dp$ is the atmospheric upwelling radiance, it is written as $R_{up}(\lambda)$.

Then we obtain the simplified form:

$$L_m(\lambda) = [\varepsilon(\lambda)B(\lambda, T_s) + (1-\varepsilon(\lambda))R_{down}(\lambda)]\tau(\lambda) + R_{up}(\lambda) \quad (2.28)$$

2.2 Data collection and model

2.2.1 IASI sensor data

IASI is a Fourier transform spectrometer based on the Michelson interferometer, associated with an integrated imaging system (IIS). The Fourier transform spectrometer provides infrared spectra with high resolution and the IIS imager is a broadband radiometer with a high spatial resolution. IASI provides information on the vertical structure of the atmospheric temperature and humidity in an unprecedented accuracy of 1 K and a vertical resolution of 1 km for the purpose of supporting numerical weather prediction. IASI is an across track scanning system with a scanning range of ± 48°20′. Each scanning line contains 30 observation positions towards the earth and two calibrated fields of view. The scanning angle interval between the two observation positions is 3.3 °, and the effective field of view (EFOV) at each observation position also contains a 2 × 2 instantaneous field of view (IFOV). The diameter of each IFOV is 14.65 mrad, and the ground spatial resolution is about12 km at nadir with a satellite altitude of 819 km. IASI sensor onboard MetOp-A satellite observes the land surface and atmosphere through 8461 channels in the infrared region from 645 cm^{-1} to 2760 cm^{-1} at a resolution (unapodized) of 0.25 cm^{-1} for each sounder pixel. Table 2.1 lists the main spectral bands of IASI and their main applications. IASI dataset can be obtained from the European Organization for the Exploitation of Meteorological Satellites (EUMETSAT) (http://www.eumetsat.int).

For the real IASI observation, the instrument noise exists in the measurement and can be simulated by a white Gaussian noise with a noise equivalent temperature (NEΔT) at 280 K (Filipe Aires et al., 2002) (Table 2.2). For a different scene brightness temperature Tb , the standard deviation $st_{T'}(v)$ at the

wavenumber v of the Gaussian noise is computed using the following equation (Filipe Aires et al., 2002):

$$st_{T'}(v) = \frac{\frac{\partial B(Tb = 280, v)}{\partial Tb}}{\frac{\partial B(Tb = Tb)}{\partial Tb}} st_{280}(v) \tag{2.29}$$

Table 2. 1. The main spectral region of MetOp-A/IASI.

Name	Spectral region (cm^{-1})	Applications
R1	650-770	Temperature profile
R2	790-980	Surface and cloud properties
R3	1000-1070	O_3 sounding
R4	1080-1150	Surface and cloud properties
R5	1210-1650	Humidity profile; CH_4 and N_2O column amount
R6	2100-2150	CO column amount
R7	2150-2250	Temperature profile; N_2O column amount
R8	2350-2420	Temperature profile
R9	2420-2700	Surface and cloud properties
R10	2700-2760	CH_4 column amount

Table 2. 2. The radiative noise of IASI channels in noise equivalent differential temperature (NEΔT) at a temperature of 280 K.

Wavenumber (cm^{-1})	NEΔT (K)	Wavenumber (cm^{-1})	NEΔT (K)	Wavenumber (cm^{-1})	NEΔT (K)	Wavenumber (cm^{-1})	NEΔT (K)
650	0.419	1200	0.095	1750	0.170	2300	0.239
700	0.157	1250	0.096	1800	0.200	2350	0.287
750	0.145	1300	0.098	1850	0.224	2400	0.351
800	0.145	1350	0.100	1900	0.250	2450	0.400
850	0.150	1400	0.105	1950	0.240	2500	0.700
900	0.150	1450	0.105	2000	0.130	2550	0.900
950	0.165	1500	0.111	2050	0.135	2600	1.100
1000	0.165	1550	0.116	2100	0.141	2650	1.300
1050	0.176	1600	0.125	2150	0.151	2700	1.600
1100	0.200	1650	0.137	2200	0.172	2750	1.935
1150	0.200	1700	0.160	2250	0.200		

IASI data products include 5 levels from 0 to 4. Level 0 is the raw data of IASI without calibration. Level 1A is the spectrum and corresponding image without apodization. This step includes data decoding, radiometric calibration, spectral calibration, image fusion, geographic calibration and time determination. IASI Level 1B is the product by oversampling the IASI Level 1A spectra. The IASI Level 1B spectra are apodized using the apodization function to obtain the IASI Level 1C spectra. IASI Level 2A product includes atmospheric temperature profile, humidity profile, trace gas distribution, surface temperature and cloud parameters product. IASI Level 2B is a surface characteristic product obtained by the combined processing of IASI and other instrument data on MetOp. These products

may be similar to Level 2A, but have higher accuracy and resolution than Level 2A. Level 3 products are spatially and temporally averaged land surface products. Level 4 is a multi-sensor product, for example, the result of assimilation by meteorological or chemical transmission modes.

The hyperspectral data used in this thesis is the observation radiance obtained from IASI Level 1C data. The format of the download Level 1C data is NATIVE （*.nat）, it can be read using the IDL or Fortran package provided by the EUMETSAT website. Level 1C data includes information such as the angle and time of observation, latitude and longitude. A detailed introduction can be found in (EUMETSAT, 2012).

2.2.2 MetOp-A/AVHRR LST product

The Advanced Very High Resolution Radiometer (AVHRR) LST product is on-board EUMETSAT (European organization for the Exploitation of Meteorological Satellites) polar system satellites (MetOp). This EUMETSAT Polar System (EPS) Daily Land Surface Temperature product provides the day-time retrievals and nigh-time retrievals of LST based on clear-sky measurements. The Satellite Application Facility (SAF) on Land Surface Analysis (LSA) provides AVHRR/MetOp Daily LST product (LSA-002), it is available on a daily basis in a sinusoidal grid centered at (0°N, 0°W), with a resolution of 0.01° by 0.01°. This daily LST was retrieved by the Generalized Split-Window (GSW) algorithm (Wan and Jeff, 1996) based on clear-sky measurements from AVHRR/MetOp. Data distribution are available at the SAF LSA website: http://landsaf.ipma.pt. The download data are coded in HDF5 format, it contains the LST field, quality control information field, sensor viewing angle, time of acquisition, etc.

2.2.3 Field-measured data

The field-measured data were collected from PIRRENE (Program Interdisciplinaire de Recherche sur la Radiométrie en Environnement Extérieur), site of ONERA (Office National d'Etudes et de Recherches Aérospatiales) center of Fauga-Mauzac (Kanani, 2005). These data are nine samples of field thermal

infrared spectra measurement data, which are slate (homogeneous and flat piece of slate), wood (plywood), water, sand1 (Morocco sand), soil (soil from Negev desert), stone (flat rough and homogeneous rock), pstyr (Extruded polystyrene), sand2 (Fontainebleau type sand), and SiC (SiC powder. Grain size ~120μm) (Table 2.3).

Table 2.3. Nine surface materials.

Name	Description
Slate	Homogeneous and flat piece of slate. Composition: SiO_2 (60 %), Al_2O_3 (17 %), Fe_2O_3 (7.6 %), K_2O (3.9 %), MgO (22.5%), …
Wood	Plywood
Water	Water
Sand1	Morroco sand. Red color. Various grain size <750 μm . Composition: SiO_2 (96.3 %), Al_2O_3 (1 %), ...
Soil	Soil from the Negev desert. Various grain size < 2 mm. Composition: SiO_2 (42.2 %), CaO (22.8 %), Al_2O_3 (5.5 %), Fe_2O_3 (2.7 %), ...
Stone	Flat rough and homogeneous roc K. Composition: SiO_2 (77 %), Al_2O_3 (12.6 %), K_2O (4.6 %), Na_2O (3.1%), Fe_2O_3 (1.2 %), ...
Pstyr	Extruded polystyrene
Sand2	Fontainebleau type sand. Various grain size <750 μm . Composition: SiO_2 (98.4 %), Al_2O_3 (0.6 %), ...
SiC	SiC Powder. Grain size ~ 120 μm

2.2.4 Atmospheric profile database and emissivity library

The Thermodynamic Initial Guess Retrieval (TIGR) data set is a climatological library of 2311 representative atmospheric situations selected by statistical methods from 80,000 radiosonde reports (Chedin et al., 1985; Chevallier et al., 1998). Each profile contains 40 levels from the surface to the top of the atmosphere

with the values of the temperature, water vapor and ozone concentrations on a given pressure grid. It is classified into five airmass types (Tropical, temperate -Midlat1-, cold temperate and summer polar -Midlat2-, Northern Hemisphere very cold polar -polar1-, winter Polar -Polar2-) (Chédin et al., 1994). The version of the TIGR database used in this thesis is TIGR 2000 v1.1, which contains vertical profiles of atmospheric temperature, water vapor, and ozone under typical and some extreme atmospheric conditions. TIGR database is stratified by air pressure, with a total of 40 air pressure levels from 1013 hPa to 0.05 hPa.

The Advanced Spaceborne Thermal Emission Reflection Radiometer (ASTER) spectral library (Alice M Baldridge et al., 2009) is used in this thesis, it includes data from three other spectral libraries: the Johns Hopkins University (JHU) Spectral Library, the Jet Propulsion Laboratory (JPL) Spectral Library, and the United States Geological Survey (USGS) Spectral Library. ASTER spectral library includes more than 2300 spectra of materials covering the 0.4–15.4 μm spectral range, it contains minerals, rocks, soils, vegetation, manmade materials, etc. (Meerdink et al., 2019). It is available at http://speclib. jpl.nasa.gov.

2.2.5 Atmospheric radiative transfer model

The operational release for 4A (Automatized Atmospheric Absorption Atlas) radiative transfer model is used to finish the fast simulation of radiative transfer for hyperspectral TIR data. The software 4A/OP is provided for an enhancement by NOVELTIS, in accordance with the convention signed between CNES, LMD/CNRS and NOVELTIS. 4A/OP is a line-by-line model, particularly over the infrared range with a “pseudo-infinite” (high) resolution or with a spectral resolution of the simulated instruments (low resolution)(Scott and Chedin, 1981). The spectral range is between 600 and 3,000 cm^{-1}. The nominal spectral resolution is 5×10^{-4} cm^{-1}. This model can simulate a wide variety of surfaces and earth atmospheric conditions and can be extended to extra-terrestrial atmospheric conditions.

Fig.2.3 demonstrates the model structure and flow chart of the 4A/OP software. The Atlases optical thickness map of gas molecules, reference thermodynamic

parameters, default gas mixture ratio are the fixed input parameters in the program for the 4A procedure. The atmospheric profile corresponding to the user-defined pressure layer, emissivity spectrum, Instrument spectral response function (ISRF) (if required), the aerosol mode (if required), simulation parameters, etc. can be determined by the users. With the support of the above input data, the 4A program is used to calculate the radiance at a single wavenumber, and then the channel radiance is obtained by convolution with the user-defined spectral response function.

The output of 4A is the radiance spectrum in a user-defined spectral domain in the infrared region. Partial derivatives of the radiance with respect to the temperature and gas mixing ratio can be also computed. They allow the model coupling with an inversion algorithm for the atmospheric constituent retrieval from infrared radiance measurements (Chaumat et al., 2009).

4A/OP is run under the Linux / Unix environment. To call the software, the command line needed is:

make -f $MA KEFILEPATH $TARGET INS=$INS CASE=$CASE ATMPROF=$ATMPROF ATM=$ATM RSTR=$RSTR RSCA=$RSCA NUMIN=$NUMIN NUMAX=$NUMAX UNIT=$UNIT

$ MAKEFILEPATH specifies the file name of the makefile; $ TARGET specifies the program that the user needs to run, it contains: runlirespi4a (the infinite spectral resolution mode of the output text file), runlirespc4a (the channel convolution mode of the output text file), runspi4a (an infinite spectral resolution mode that only outputs binary files), runspc4a (a channel convolution mode that only outputs binary files); $ INS specifies the instrument function ISRF; $ CASE specifies the instrument function version (case); $ ATM specify the atmospheric profile database; $ ATMPROF is the index number of an atmospheric profile within the atmospheric profile database; $ RSTR is the user-defined simulation parameter file; $ RSCA is the user-defined aerosol parameter file; $ NUMIN is the beginning of the extraction for the conversion (in wave number, unit cm^{-1});

$ NUMAX is the end of the extraction for the conversion (in wave number, unit cm^{-1}); $ UNIT is Jacobian unit index for Jacobian ASCII outputs.

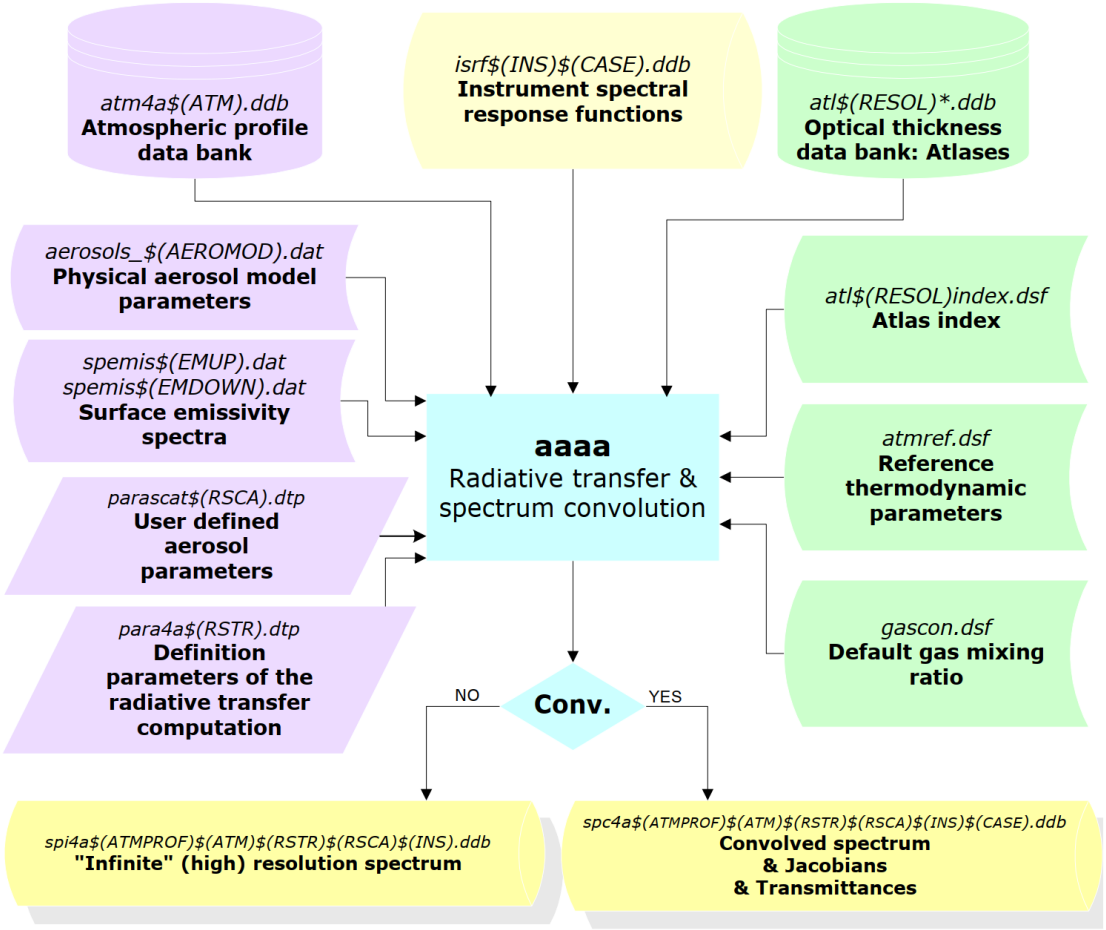

Fig.2. 3. Flow chart of the software 4A/OP (Chaumat et al., 2009).

Chapter 3. Improved LSEC Method for Temperature and Emissivity Separation

3.1 Introduction

Nowadays, many temperature–emissivity separation (TES) methods have been developed to acquire the LST information with the accurate atmospheric correction. One approach is via descending dimension of N channels emissivity, thus reducing the number of the unknowns. Emissivity eigenvectors (EVs) method (Liu et al., 2006) and wavelet transform method (Zhang et al., 2017) enable the projection of the spectral emissivity in a orthogonal basis or frequency domain to further reduce the number of emissivity to separate LST and LSE. Linear spectral emissivity constraint method (LSEC) (Wang et al., 2011) divides LSE into several sections, each section is expressed with a linear function. LSEC successfully turns the underdetermined problem into an overdetermined problem, making the temperature-emissivity separation solvable. Compared with ISSTES method, LSEC method is efficient and easily implemented because there are no singular points in its cost function. If the data include noise, the LSEC method also can produce more accurate results than ISSTES method with good noise-resistant ability (Wang et al., 2011). However, using an equal piecewise linear LSE description (segment length 10 cm^{-1}) will result in some crests or troughs of emissivity being directly covered by straight lines, thus losing their information. If we can get the real or an estimated shape of emissivity and propose a new segmentation scheme according to its shape, the accuracy or the operational efficiency will be improved to some extent.

In this part, an initial-shape-estimation algorithm of LSE is proposed to provide a new LSE segmentation scheme that is subsequently adopted in the separation of LST and LSE for simulated hyperspectral infrared IASI data. Section 3.2 is devoted to the methodological development, describing the theoretical basis and improvement of retrieving LST. Section 3.3 gives the simulated numerical

experiment and sensitivity analysis. Section 3.4 presents the validation with in-situ measurements. Finally, the conclusions are summarized in the last section.

3.2 Methodology

Assuming a cloud-free atmosphere under local thermodynamic equilibrium and neglecting the atmospheric scattering effects, in the TIR region, the radiative transfer equation (RTE) can be written as (Li et al., 2013)

$$L(\lambda,\theta,\varphi)=\varepsilon(\lambda,\theta,\varphi)B(\lambda,T_s)\tau(\lambda,\theta,\varphi,p_s)+\int_{P_s}^{0}B(\lambda,T_p)\frac{\partial\tau(\lambda,\theta,\varphi,p)}{\partial p}dp$$

$$+\int_0^{2\pi}\int_0^{\frac{\pi}{2}}\rho(\lambda,\theta,\varphi,\theta',\varphi')\,L_d(\lambda,\theta',\varphi')\tau(\lambda,\theta,\varphi,p_s)\cos\theta'\sin\theta'd\theta'd\varphi' \quad (3.1)$$

where λ is wavelength. θ and φ are the viewing zenith angle and azimuth angle, respectively. θ' and φ' are the zenith angle and azimuth angle of downwelling direction of atmospheric radiance, respectively. L is the measured spectral radiance at the top of the atmosphere (TOA). ε is the LSE. $B(\lambda,T_s)$ is the Planck function at surface temperature T_s. P_s is the surface pressure level. τ is the atmospheric transmittance from a pressure level to the TOA along the viewing angle. T_p is atmospheric temperature. ρ is the surface bidirectional reflectance. Assuming the surface as a Lambertian reflector, $\rho=(1-\varepsilon)/\pi$ is also substituted into Eq.3.1.

$\frac{1}{\pi}\int_0^{2\pi}\int_0^{\frac{\pi}{2}}L_d(\lambda,\theta',\varphi')\cos\theta'\sin\theta'd\theta'd\varphi'$ is atmospheric downwelling radiance, it is written as $R_{down}(\lambda)$;

$\tau(\lambda,\theta,\varphi,p_s)$ is written as $\tau(\lambda)$;

$L(\lambda,\theta,\varphi)$ is expressed as $L_m(\lambda)$;

$\int_{P_s}^{0}B(\lambda,T_p)\frac{\partial\tau(\lambda,\theta,\varphi,p)}{\partial p}dp$ is the atmospheric upwelling radiance, it is written as $R_{up}(\lambda)$.

Then we obtain Eq.3.2:

$$L_m(\lambda) = [\varepsilon(\lambda)B(\lambda,T_s) + (1-\varepsilon(\lambda))R_{down}(\lambda)]\tau(\lambda) + R_{up}(\lambda), \quad (3.2)$$

When an accurate atmospheric correction has been done (τ, R_{up}, and R_{down} for all bands are known), N equations will contain N unknown emissivities plus one unknown temperature, making the system of equations underdetermined. Many approaches have been developed to overcome the problem of having an underdetermined system of equations. Compared to other published methods, LSEC is simpler and more efficient, with a strong anti-noise ability. In order to make equations solvable and further retrieve LST in LSEC, LSE is approximated as a piecewise linear function (M sections). As shown in Fig.3.1, LSE is divided into M sections and every section can be expressed using a linear function, thus the *ith* channel's emissivity within the *Kth* section can be expressed as a linear function with channel (wavelength) λ_i (Eq.3.3).

$$\varepsilon_K(\lambda_i) \approx a_K\lambda_i + b_K, \; K=1,\ldots,M, \quad (3.3)$$

where a_K and b_K are the two sets of coefficients of the M linear functions.

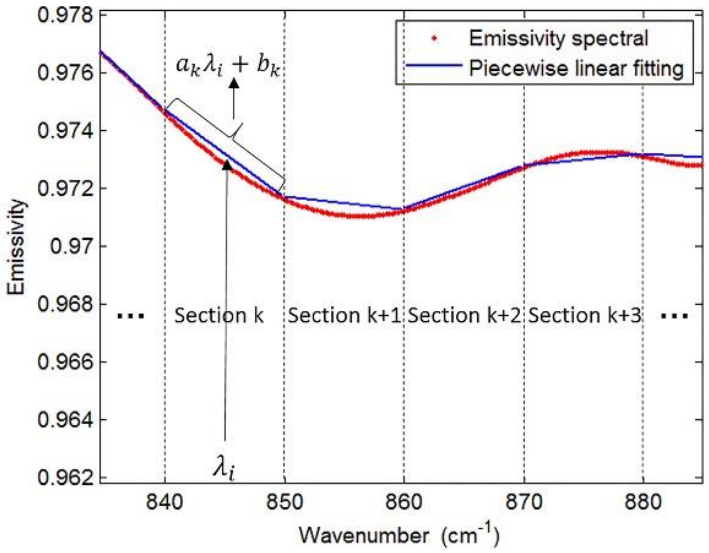

Fig.3. 1. Diagrammatic sketch of piecewise linear emissivity spectra fitting. The red line is an actual emissivity spectrum (from a type of soil), the abscissa is the wavenumber, and the ordinate is the emissivity, while the blue lines are the fitting spectra.

This linear approximation of the segment reduces the number of unknowns, making the system of equations solvable. But accurate atmospheric correction is

necessary to avoid significantly deteriorated and unacceptable accuracy of LST. However, the equal interval scheme, with an equal interval segment length of 10 cm^{-1} as suggested in the LSEC method, causes the loss of some feature points (crest or trough points of the spectrum). Fig.3.2 shows that with a 10cm^{-1} segment length, some crests and troughs on the curve are covered, which means the scheme does not satisfactorily fit the real spectrum curve. Moreover, for a spectrum that resembles a straight line in a wider band, segmentation with 10 cm^{-1} leads to too many segments, which will affect the calculation efficiency.

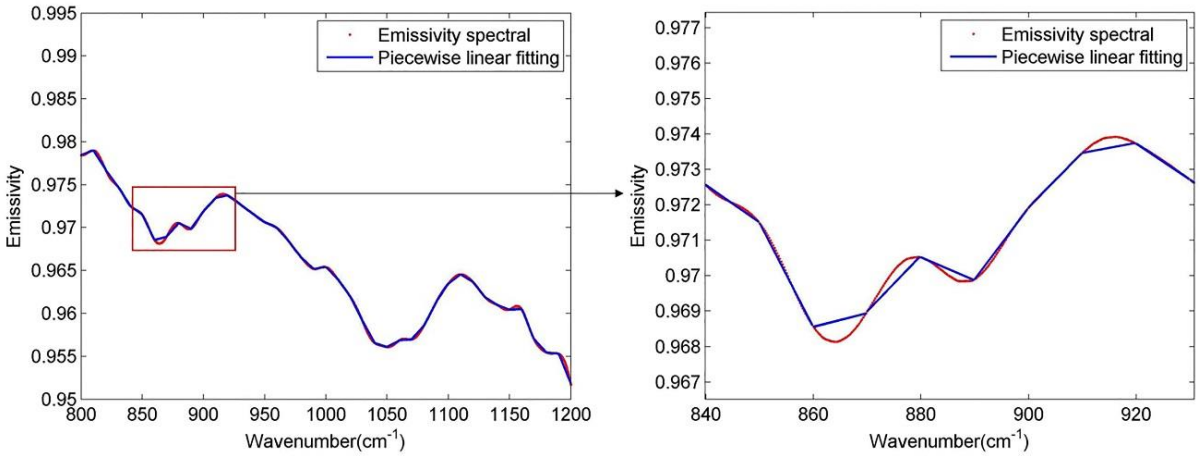

Fig.3. 2. Diagrammatic sketch of piecewise linear emissivity spectra fitting. The red line is an actual emissivity spectrum (from a type of soil), while the blue lines are the fitting spectra.

If the length of segment can be changed according to the variation of the actual emissivity spectrum, the fitting may be further improved in terms of accuracy and speed of operation. Therefore, this work provides a procedure for estimating the initial shape of LSE to keep most of the crest and tough information, then discusses whether the initial-shape-estimation process will lead to a better accuracy. After compensating for the atmosphere (downwelling radiance, upwelling radiance, and transmittance are known), we attempt to estimate the shape of the unknown LSE. $L_{sur}(\lambda)$ is adopted to express $(L_m(\lambda)-R_{up}(\lambda))/\tau(\lambda)$, then Eq.3.4 is another form of Eq.3.2: LSE can be calculated with an initial estimation of LST (T_s).

$$\varepsilon(\lambda) = (L_{sur}(\lambda) - R_{down}(\lambda))/(B(\lambda,T_s) - R_{down}(\lambda)), \quad (3.4)$$

The deviation of LSE caused by the error of estimated LST implies the influence of atmospheric downwelling radiation. That is, when the temperature estimation is biased, the obtained emissivity spectrum will have the spectral characteristics of atmospheric downwelling radiation (absorption line characteristics, showing more twists and turns, not smooth).

A soil emissivity sample (red-orange sandy loam) chosen from the ASTER spectral library is given in Fig.3.3 (red solid line) together with the corresponding estimated LSE. The true LST is varied between −1 and +0.5 K in steps of 0.5 K as the estimated LST value. The ground-level brightness temperature (T_g) that varies in bands (λ) is defined by $B(\lambda,T_g)=L_{sur}(\lambda)$, the maximum T_g value in N bands (max ($T_{g\lambda}$)) is also adopted to be the estimated LST and represented in Fig.3.3. Fig.3.3 shows that the characteristics of the atmospheric downwelling radiation in LSE estimation spectrum will be lower if the estimation of the surface temperature is more accurate, also max ($T_{g\lambda}$) is close to true LST. Finally, max ($T_{g\lambda}$) is adopted to be the estimated LST value, the estimated LSE result calculated from Eq.3.4 is designated as ($\widetilde{LSE}$).

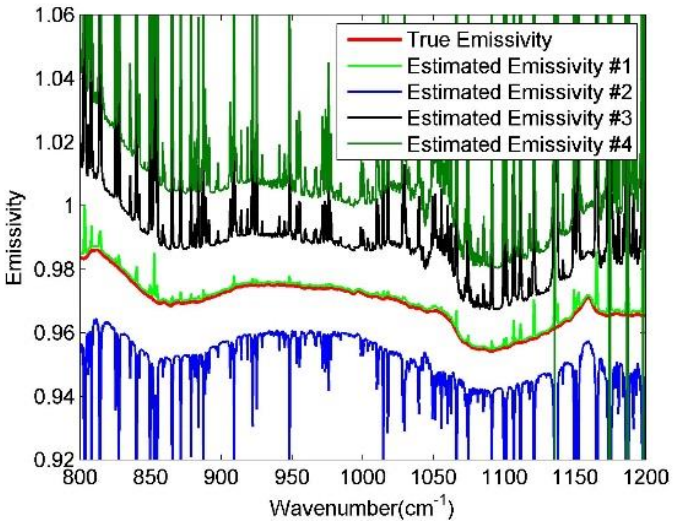

Fig.3. 3. Diagrammatic sketch of soil emissivity estimation. The red dot line is the actual emissivity spectrum, while the other lines are the estimated spectra. Estimated Emissivity #1 represents the estimated spectrum calculated with the max ($T_{g\lambda}$) using Eq.3.4. The true LST is varied with +0.5 K, −0.5 K and −1 K as the estimated LST value, Estimated Emissivity #2, #3 and #4 represent the corresponding estimated spectra.

In order to obtain the LSE shape estimation, a pre-estimate shape procedure (Fig.3.4) is firstly adopted to restore the shape and determine most of the crest or trough information.

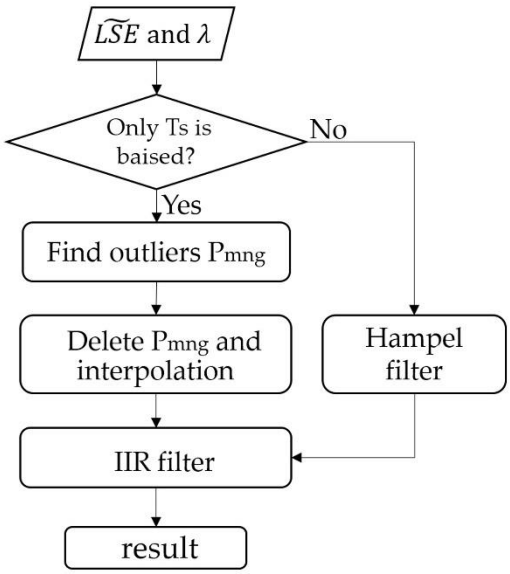

Fig.3. 4. Flow diagram for the pre-estimate shape procedure.

When max ($T_{g\lambda}$) is adopted as the LST estimation in Eq.3.4, the estimated LSE crest or trough position is basically unchanged, except for the channels of peak portion influenced by atmospheric information. Based on this, the purpose of our program is to remove the peaks and then take a smooth overlay to obtain most of the crest or trough positions. The absolute value of first-order difference, abs(Der_LSE), in $\widetilde{LSE}$ between two adjacent channels is firstly calculated. The outliers can be removed by distinguishing the position where abs(Der_LSE) changes sharply, by setting a threshold. The threshold value cannot be set to a fixed value because of the uncertainty of abs(Der_LSE) with different kinds of LSE or max ($T_{g\lambda}$). In this work, the abs(Der_LSE) is sorted in ascending order as the ordinate, then record the ordinal number of each sorted value as the abscissa. Afterwards the range of abscissa is readjusted as [min(abs(Der_LSE)) max(abs(Der_LSE))] with a step delta_m=(max(abs(Der_LSE))−min(abs(Der _LSE)))/length(abs(Der_LSE)), where length(abs(Der_LSE)) is the number of abs(Der_LSE). When the origin is connected to each point (abs(Der_LSE)) on the difference curve, every obtained straight line has an included angle (θ_{sig}) with the

abscissa. This definition makes all the abs(Der_LSE) data lines fall within the 45-degrees included angle (dotted line in Fig.3.5 with the horizontal axis), which is uniformly defined for comparison. If θ_{sig} is larger than the mean value of θ_{sig} multiplied by A (a constant), the corresponding Der_LSE value set is defined as Pm, also recording the channel position i. According to a large amount of data testing, A is set to 0.414.

Using only the first-order difference will cause a misjudgment of the outliers, it will eliminate the peaks and troughs that originally exist in the wider wavelength range of the true LSE. Therefore, the absolute value of second-order difference between the elements of $\widetilde{LSE}$ is used. The processing flow is the same as that of first-order difference method previously mentioned above but allows determining a second outliers set, to be referred to here as P_n. After two treatments to obtain the outliers, we take the intersection of the two types of outliers, resulting in a set to be called P_{mn}. At the same time, when the number of channels between each two adjacent positions ($P_{mn}|_i$ and $P_{mn}|_{i+a}$, where a is a constant) is less than five channels (a<5), all channels between two adjacent positions will be considered as outliers, to be referred to as P_g. Finally, the outlier is the union of P_g and P_{mn}. Afterwards, the trajectory of the curve is obtained via spherical linear interpolation after the outliers are removed. The interpolated data have a small amount of noise and are designed to be processed by a 12-stage infinite impulse response (IIR) zero-phase delay low-pass filter (Widmann et al., 2015).

When the data contain at-ground radiance error (random noise) and downwelling radiance error, the estimated emissivity loses some shape information. In that case, the Hampel filter is adopted. The Hampel filter block detects and removes the outliers of the input signal by using the Hampel identifier (Pearson, 2002). The Hampel identifier is a variation of the three-sigma rule of statistics, which is robust against outliers. For each sample of the input signal, the block computes the median of a window composed of the current sample and (Len−1)/2 adjacent samples on each side of the current sample (Len is the window length you specify through the window length parameter). After the correction of the IIR zero-phase delay low-pass filter, the Hampel filter further smooths the

curve. Fig.3.6 shows the result of the pre-estimate shape algorithm of the soil spectrum mentioned in Fig.3.2. When the pre-estimate shape algorithm is finished, we can get a new segmentation scheme based on the recovered LSE shape and further use the LSEC algorithm to retrieve LST and LSE, also we henceforth refer to this pre-estimate shape of the LSEC algorithm as the PES-LSEC method.

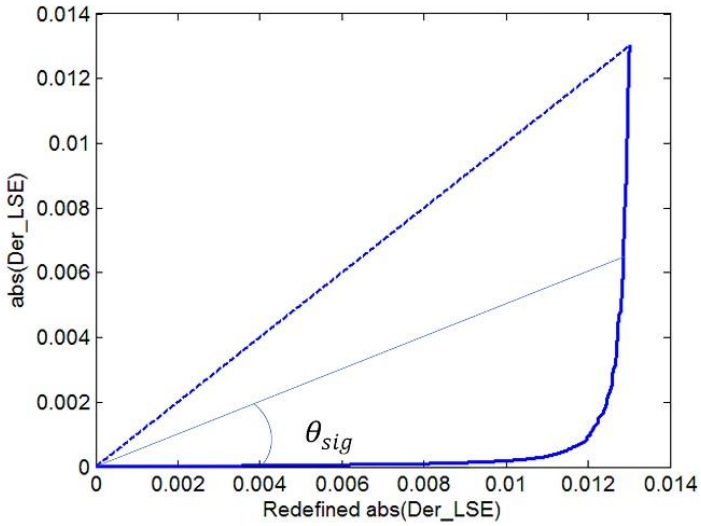

Fig.3. 5. Diagrammatic sketch of Der_LSE.

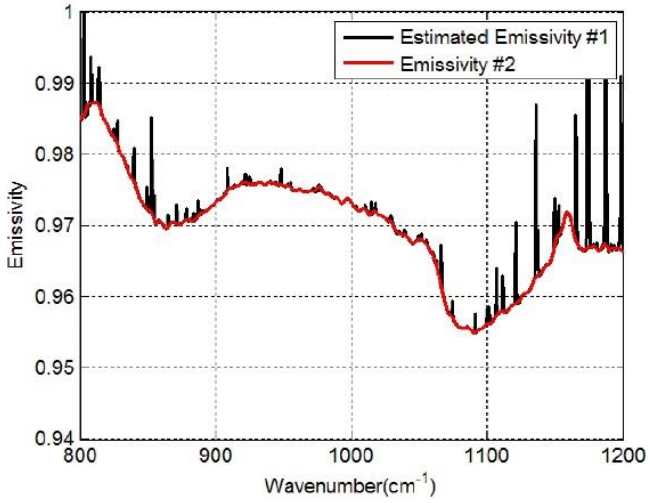

Fig.3. 6. Estimated Emissivity #1 represents the estimated LSE calculated with the max ($T_{g\lambda}$) using equation 4 (Black line). Red line (Emissivity #2) is the estimated shape of LSE using the pre-estimate shape procedure.

3.3 Experiments with the simulated data

3.3.1 Simulated dataset

The PES-LSEC method is tested with simulated data and in-situ data. The simulated data are prepared using in a simulation model (4A/OP) with spectral (ASTER library) and climatological libraries to produce the necessary elements in Eq.3.2. In-situ data are used for the evaluation of the PES-LSEC method.

To simulate the hyperspectral thermal infrared variables in Eq.3.2, the 4A/OP model is adopted to calculate the transmittance, upwelling radiance, and downwelling radiance using input atmospheric profiles and the emissivity database. In this experiment, the spectral range is 800 cm^{-1}–1200 cm^{-1}, with a spectral resolution of about 0.5 cm^{-1} and sampling interval of 0.25 cm^{-1}. The spectral response function is the same as that of the IASI sensor.

The input atmospheric profiles are obtained from the TIGR data set. The selected 946 clear sky atmospheric profiles are used for simulation experiments, while the bottom atmospheric temperature of the profiles is adopted as LST. Meanwhile, 65 spectra (52 soil types, 4 vegetation types, 9 water/snow/ice types) from the ASTER spectral library are collected to describe most of the features appearing in the terrestrial ecosystem (Fig.3.7).

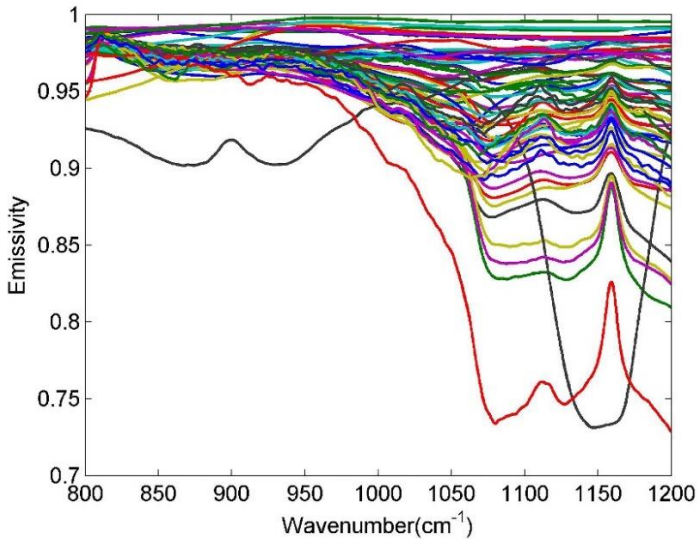

Fig.3. 7. Selected emissivity spectra from the ASTER spectral library.

3.3.2 Sensitive analysis

The required inputs for the algorithm are the ground-leaving radiance and atmospheric downward radiance, which are available after the atmospheric correction process. Atmospheric correction is a key issue, and there are always errors associated with it. The errors related to these two quantities can propagate into the derived surface temperature and emissivity. The potential errors include random instrumental noise, instrument calibration error, and atmospheric downward radiance error. In this work, because we deal mainly with the at-ground level, only the at-ground radiance error and downwelling radiance error are discussed. Different levels of noise NEΔT (NEΔT = 0.0, 0.1, 0.2, 0.3, 0.4, and 0.5 K) were added to the simulated at-ground radiance. As shown in Fig.3.8, the PES-LSEC method does not greatly improve the retrieval accuracy of LST nor of LSE, with NEΔT = 0.0, 0.1, 0.2, compared to that of LSEC. Whereas, when NEΔT increases to 0.5 K, RMSEε with the PES-LSEC method is 0.0045, and RMSET is 0.07 K. The PES-LSEC method has a similar performance to that of the LSEC method for the retrieval error on LST but improves the accuracy of the LSE error. When the at-ground spectral radiance error is added to the simulated data, the random error results in partial shifts of the crests and troughs, leading to a loss of most information. Our pre-estimate shape procedure can reconstruct the basic trend of the curve, which is similar to that of the actual emissivity and is relatively smooth. This smoothed curve leads to a significant reduction in the number of segments but a large error increase in LSE and LST. However, when the number of segments is increased to be similar to the number of segments of the LSEC scheme, the performance is nearly the same in terms of the LSEC accuracy.

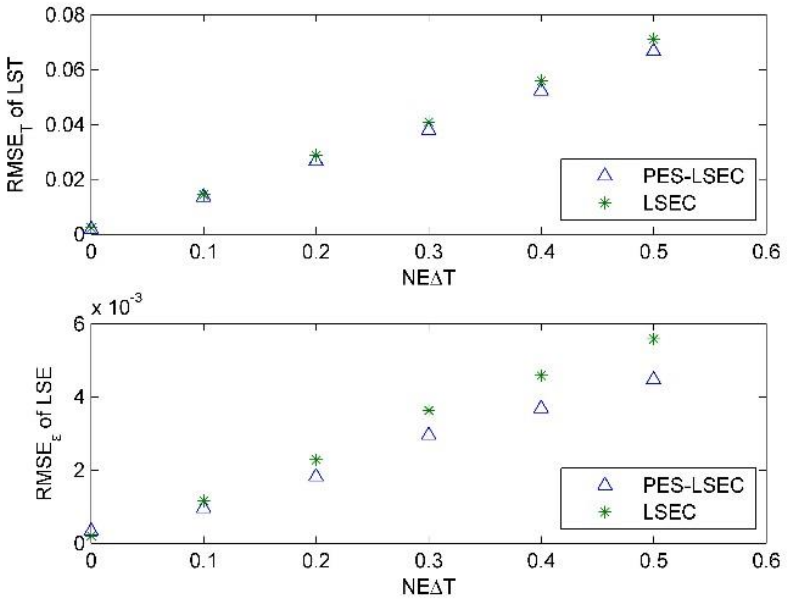

Fig.3. 8. Comparison of retrieval emissivity spectrum and actual emissivity spectrum.

To investigate the influence of the atmospheric downward radiance error on the accuracies of land surface temperature and emissivity retrieval, the moisture profiles from the TIGR database were multiplied by 80% and 120%, leaving the shape of the humidity profile unchanged, but generating the simulated downwelling radiance with error. Fig.3.9 shows the retrieval accuracy of LSE in each band when the moisture profiles is not biased. When the moisture profiles are shifted by 0.8 and 1.2, $RMSE_T$ are 1.11 K and 1.14 K, respectively, using the PES-LSEC method. When only the LSEC method is used, $RMSE_T$ are 1.2 K and 1.4 K, respectively. $RMSE_{\varepsilon,j}$ of the PES-LSEC method in each band is mostly below 0.02 when the moisture profiles are shifted by −20% and is mostly less than 0.04 when the moisture profiles are shifted by +20% (Fig.3.9), better than the LSEC retrieval results. Compared with the ISSTES method, LSEC and PES-LSEC show good noise-resistant ability especially in the 1050–1200 cm^{-1} region. However, with the influence of the moisture profile error, the atmospheric downward radiance error still has a bigger effect on LST and LSE retrieval with the PES-LSEC method.

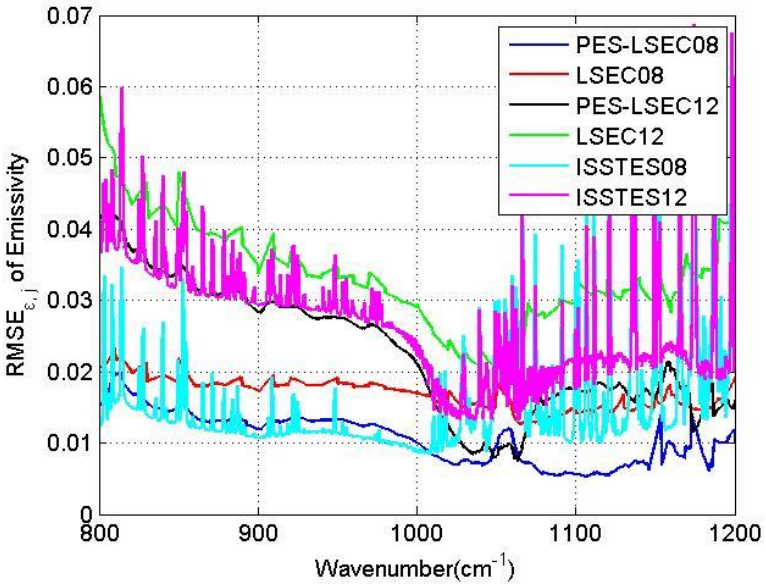

Fig.3. 9. $RMSE_{\varepsilon,j}$ for the 800–1200 cm^{-1} region. The blue and black lines are the retrieval results of the PES-LSEC method with the scale factors of moisture profile being −0.2 and 0.2, respectively. The red and green lines are the LSEC results with the scale factors of moisture profile −0.2 and 0.2, respectively. ISSTES08 and ISSTE12 present the RMSEε,j of emissivity using ISSTES method with the scale factors of moisture profile −0.2 and 0.2, respectively.

3.3.3 Results

For LST and LSE retrieval results, the temperature bias and root-mean-square error are adopted to characterize the method accuracy:

$$\Delta Ts = T_{ret} - T_{true}, \tag{3.5}$$

where ΔTs is the difference between the retrieved temperature (T_{ret}) and the actual temperature (T_{true}). $RMSE_T$ is the root-mean-square error of the retrieved LST and actual LST, while N_D is the number of total samples.

$$RMSE_T = \sqrt{\frac{\sum_{i=1}^{N_D} (T_{ret,i} - T_{true,i})^2}{N_D}}, \tag{3.6}$$

$$RMSE_{\varepsilon,j} = \sqrt{\frac{\sum_{i=1}^{N_D} (\varepsilon_{ret,i,j} - \varepsilon_{true,i,j})^2}{N_D}}, \tag{3.7}$$

$$RMSE_{\varepsilon} = \sqrt{\frac{\sum_{i=1}^{N_D} \sum_{j=1}^{N_M} (\varepsilon_{ret,i,j} - \varepsilon_{true,i,j})^2}{N_D \cdot N_M}}, \quad (3.8)$$

$RMSE_{\varepsilon,j}$ is used to evaluate the algorithm emissivity retrieval accuracy (rmse) in each band, where ε_{ret} is the retrieved emissivity, ε_{true} is the true emissivity. N_M is the number of bands, the rmse of the retrieved and actual emissivity difference ($RMSE_{\varepsilon}$) can be described using Eq.3.8.

The prepared data are firstly processed using the pre-estimate shape procedure under the condition that only LST was biased. Fig.3.8 shows the initial shape estimate results of three types of land surface (red-orange sandy loam, sea water, and green grass): the reconstructed data (Emissivity #2, red lines) have a similar tendency to that of the true LSE (green lines). Furthermore, most of the crest and trough positions of true LSE are preserved, which is crucial for subsequent segmentation processing. Secondly, the first and second derivatives are used to identify the inflection points to provide new segmentation schemes for the aforementioned three spectra demonstrated in Fig.3.8 (black points). Afterwards, the non-equal-interval LSE segmentation scheme was integrated into the LSEC algorithm (PES-LSEC method) to obtain the retrieval emissivity shown in Fig.3.8 (blue lines). As expected, the new segmented scheme according to the position of inflection points better fits the true LSE curves and draws satisfactory results. These examples present the condition that max ($T_{g\lambda}$) is close to true LST using one typical atmospheric profile, so the Emissivity #2 (red lines) shows a good agreement with the true emissivity. When the deviation between max ($T_{g\lambda}$) and Ts is large, the identified red line does not exactly match the true curve shape, but it can keep most of the inflection point information that provides satisfactory emissivity result after using the PES-LSEC method. Also, we can find the crest and trough positions are larger than the real values for some emissivity spectra, for example the green grass in the 1150 cm−1200 cm^{-1} region. This is a normal phenomenon, because some small outliers are retained without reaching the set threshold. This will cause a slight increase in the number of LSE segments and in the computation time. Nevertheless, the retrieval accuracies of LST and LSE will be improved to some extent in the linear emissivity spectra fitting process.

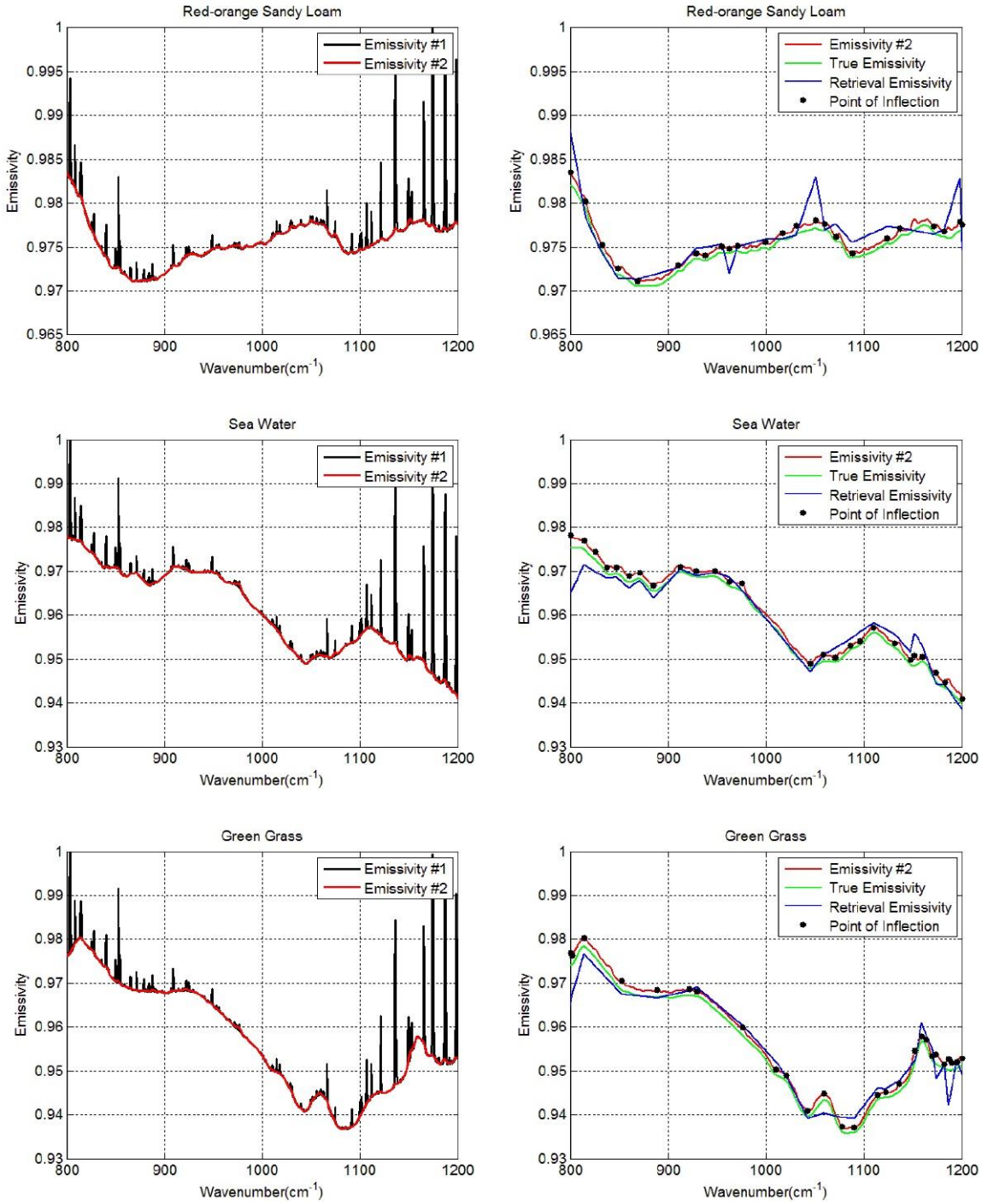

Fig.3. 10. Retrieval results of three spectra (red-orange sandy loam, sea water, and green grass) using PES-LSEC method. The calculation results of equation (4) with max ($T_{g\lambda}$) are drawn in black lines (Emissivity #1). Red lines (Emissivity #2) are the estimated shape of LSE using the pre-estimate shape procedure. Black points are the identified inflection points. Green lines are the true emissivity values used in the simulation. Blue lines are the final retrieval results of emissivity using PES-LSEC method.

Table 3. 1. Retrieval accuracies of LSE and LST using LSEC and PES-LSEC method.

	LSEC method		PES-LSEC method	
	RMSEε	RMSET (T)	RMSEε	RMSET (T)
Red-orange sandy	6.2 e^{-5}	5.5 e^{-4}	4.4 e^{-5}	3.1 e^{-4}
Sea water	1.9 e^{-4}	1.0 e^{-3}	8.7 e^{-5}	5.2 e^{-4}
Green grass	2.1 e^{-4}	8.1 e^{-4}	1.2 e^{-4}	3.8 e^{-4}

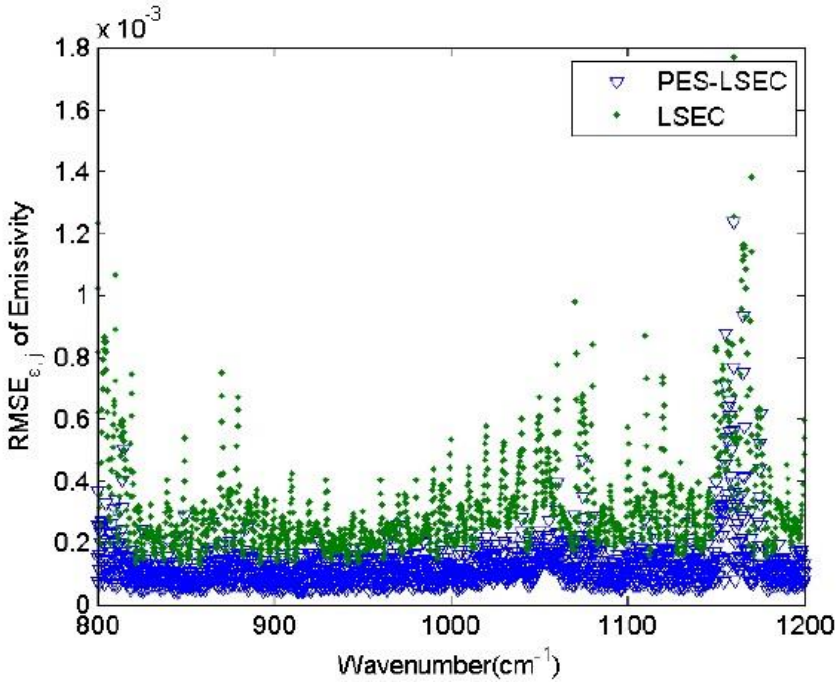

Fig.3. 11. $RMSE_{\varepsilon,j}$ of the two methods.

Table 3.1 represents the retrieval accuracy of LSEC and PES-LSEC method for three land surface type (red-orange sandy loam, sea water and green grass) corresponding to Fig.3.10. The rmse of the retrieved emissivity and LST with the PES-LSEC method are better than LSEC method, but slightly. When all 946 atmospheric profile types and 65 emissivity spectra for the PES-LSEC method are considered, the $RMSE_T$ is 0.001, which is smaller than the LSEC retrieval accuracy (0.005). ΔTs is within [−6.0 e^{-3}, 6.0 e^{-3}] K. The root-mean-square error in each channel ($RMSE_{\varepsilon,j}$) is shown in Fig.3.11 for the two methods LSEC and PES-LSCE. In the 800-1200 cm^{-1} region, with the PES-LSCE method, $RMSE_{\varepsilon,j}$ is smaller than

0.0014, and smaller than for the LSEC method (0.0012). When the errors of at-ground radiance and downwelling radiance are not considered, our method has a better performance on the shape estimation, providing a reasonable segmentation scheme and a smaller retrieval error.

3.4 Validation with the in-situ data

In order to validate the proposed separation method of LST and LSE, the in-situ data from PIRRENE was used. Fig.3.12 gives the average emissivities of the 9 samples that were measured at different times (3, 4, 7, 8, 9, 10, 13, 15, and 16 o'clock) for two days. A detailed description of the ground test can be found in (Kanani, 2005; Kanani et al., 2007a).

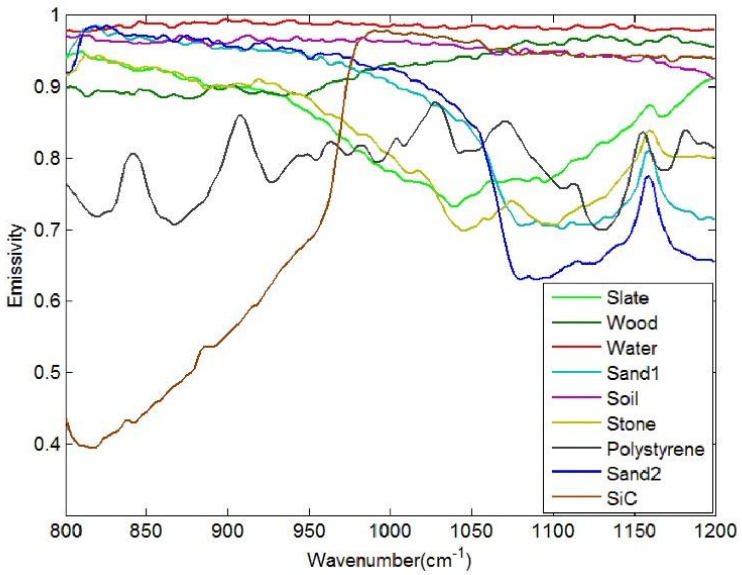

Fig.3.12. Emissivity spectra of 9 samples.

In the field-measured experiment, the data obtained via direct measurement include: 1) nine samples and labsphere infragold plate leaving-surface spectral radiances measured by the BOMEM (MR254) spectrometer (the spectral resolution is 4 cm^{-1}, and the sampling interval is 2 cm^{-1}); 2) nine sample temperatures measured by the broadband long-wave infrared radiometer (KT19); 3) infragold plate temperature measured by the thermocouple; 4) reflectance of infragold plate and nine sample emissivities measured in laboratory. Directly measured data needs to be initially processed to obtain the downwelling radiation. Meanwhile, in

order to be able to compare them with the actual temperature of the sample, the true value of the sample temperature must also be calculated from KT19 measurements. Therefore, preprocessing of measured data is essential, the detailed process can be found in (Kanani, 2005; Kanani et al., 2007b).

Because the resolution is different from that of the simulated data, the parameter A in the pre-estimate shape procedure is reset to 2. To validate the accuracy of the retrieval LSE, an index $Mean_{\varepsilon t}$, is used to analyze the emissivity retrieval accuracy of algorithm, the equation is:

$$Mean_{\varepsilon t} = \frac{\sum_{i=1}^{N_D} \sum_{j=1}^{N_M} |\varepsilon_{ret,i,j} - \varepsilon_{true,i,j}|}{N_D \cdot N_M}, \tag{3.9}$$

Where $\varepsilon_{ret,i,j}$ is the retrieved emissivity of the *ith* sample at wavenumber j, $\varepsilon_{true,i,j}$ is the actual emissivity of the *ith* sample at wavenumber j.

$RMSE_T$ of the PES-LSEC method is 0.9 K better than the LSEC's accuracy (1.1 K). $Mean_{\varepsilon t}$ of the PES-LSEC method and LSEC method are 0.01 and 0.012, respectively. Retrieval results of the nine sample emissivity spectra using LSEC and PES-LSEC method are shown in Fig.3.13. To clearly demonstrate the performances of the LSEC and PES-LSEC methods, ΔTs of two separation algorithms and RMSEε for each sample are drawn on Fig.3.14 and Fig.3.15, respectively. The inversion value and the measured value for LSE are found to be in good agreement to a large extent, and LSE values of most samples are slightly overestimated. Also, PES-LSEC method's errors with the nine samples follows the LSEC retrieval emissivity to a certain degree. PES-LSEC method shows good performance in identifying the inflection point, for the polystyrene sample, PES-LSEC better preserves the crest and trough position around 1050 cm^{-1}, 1113 cm^{-1}, 1170 cm^{-1} and 1180 cm^{-1} channel than LSEC method, thus improving the accuracy to some extent. Soil, wood, Morocco sand and water also present a certain degree of improvement. In addition, PES-LSEC method achieves similar accuracy with the LSEC using large segmentation interval. The sample's spectrum of slate, stone and SiC are relatively smooth, so large segments are identified. For example, in the 920–1000 cm^{-1} interval, the slate and stone spectra are only divided into two

segments, SiC is only divided into 3 segments in the range of 1020-1190 cm^{-1}. For these three samples in Fig.3.15, we can find the accuracy of the PES-LSEC and LSEC methods are basically the same. This is mainly because PES-LSEC method uses a segmentation scheme with large segments, and some small peak-to-valley information are ignored, resulting in less improvement of the precision. As suggested in the LSEC method, 5 channels in one segment can better fits the LSE even if some peak points are lost.

There are still some other problems when comparing the retrieval results with the laboratory emissivity. For example, the uncertainty of the sample emissivity laboratory measurement may cause a deviation from the land surface temperature calculated via KT19. Meanwhile, the instantaneous fields of view (IFOV) of BOMEM and KT19 are not the same, resulting in different observation sample areas. The heterogeneity and non-isothermality of the sample itself also cause differences in the temperature observations. Generally, the PES-LSEC method has a good performance with in situ data, it keeps most of the crest and tough information of emissivity. The LST retrieval accuracy of most samples is within 1 K. Wood, polystyrene, and SiC present a bigger $RMSE_{\varepsilon}$ than other samples, and the retrieved emissivities are basically consistent with the tendency of laboratory LSE.

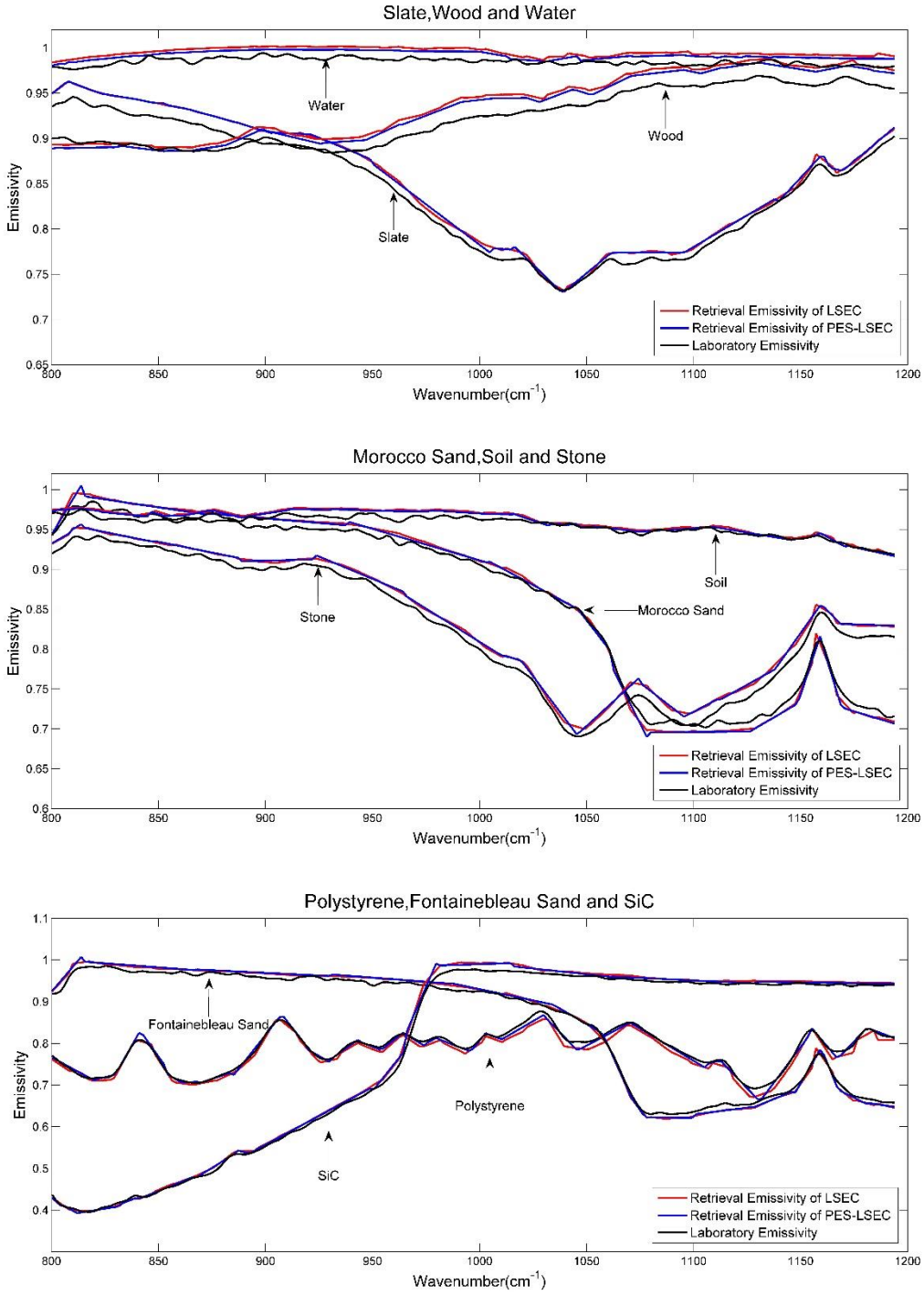

Fig.3.13. Laboratory emissivities of the nine samples and retrieved emissivities using LSEC and PES-LSEC method.

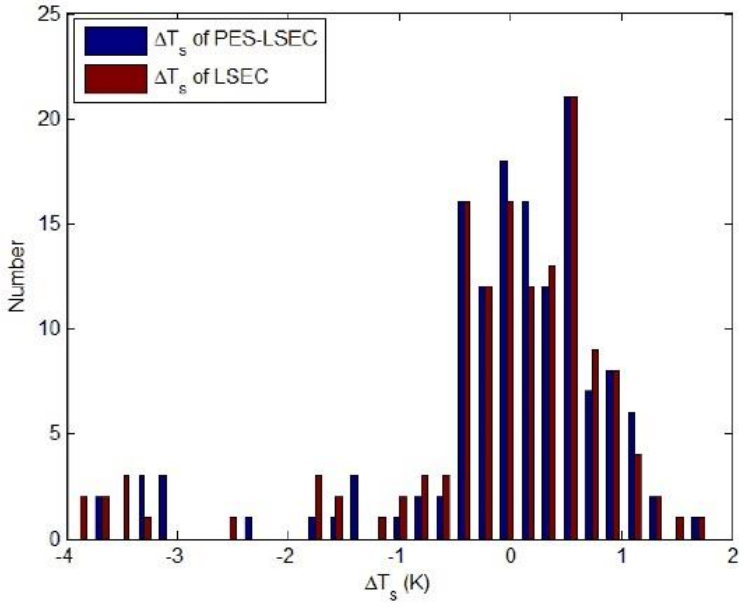

Fig.3.14. ΔT_s of nine samples.

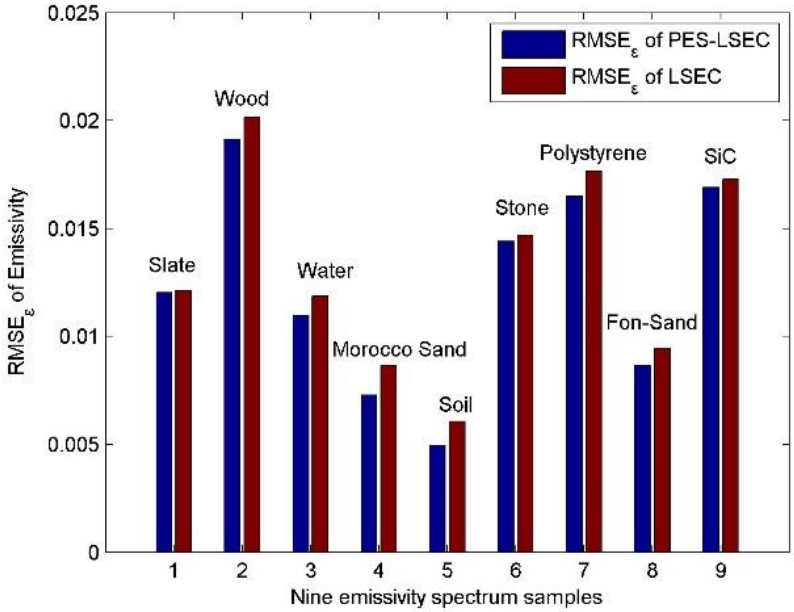

Fig.3.15. $RMSE_\varepsilon$ of nine emissivity spectrum.

3.5 Summary and Conclusion

A temperature and emissivity separation method (PES-LSEC method) was proposed based on the linear constraint of LSE to reduce the number of unknowns, making the underdetermined equation solvable with accurate atmospheric correction. In this work, a pre-estimate shape method was first adopted to provide

the basic tendency of LSE and determine relatively accurate crest and trough positions, producing a better non-equal-interval segmentation scheme. The PES-LSEC method is then used to separate the LST and LSE.

The numerical experiments are first used to investigate the accuracy of the algorithm and to carry out sensitivity analyses. A total of 946 atmospheric profiles from the TIGR database and 65 natural surface materials from the ASTER spectral library are combined together to generate the simulated data set. When noise of NEΔT = 0.5 K is added to the at-ground radiance of simulated data, $RMSE_\varepsilon$ and $RMSE_T$ are 0.0045 and 0.07 K, respectively. When the moisture profiles are shifted by ±0.2, $RMSE_T$ are 1.11 K and 1.14 K, respectively. $RMSE_{\varepsilon,j}$ of the retrieved emissivities of the PES-LSEC method are mostly below 0.02 and 0.04 in each channel, which is better than the LSEC retrieval results.

The results of the sensitivity analysis show that at-ground radiance error equivalent of 0.5 K has a significant influence on emissivity retrieval and a relatively small influence on surface temperature retrieval, in comparison with those for the LSEC method. The atmospheric downward radiance error has big impacts on temperature and emissivity estimation, but our algorithm can achieve better retrieval accuracy of temperature and emissivity than those of the LSEC method.

The PES-LSEC algorithm is also used to retrieve surface temperature and emissivity with in situ measurements. With initial-shape estimation, more accurate and less segmentation schemes were given to obtain a better accuracy than that of the LSEC method. The crest and tough information of LSE are better preserved using PES-LSEC method. As for the LST and LSE retrieval accuracies, they have been improved to some extent. For most of samples, the errors of LST are within 1 K, and the root-mean-square-error of LSE of every sample has been found to be less than 0.02.

Finally, even though we assume that the atmospheric effects of the remotely sensed data have been successfully corrected, our method fits only for the at-ground level, and a new step will be to reach the satellite level. The unknown errors of upwelling radiance and transmittance of the atmosphere will make the pre-estimate shape procedure invalid and unable to determine the basic tendency of

emissivity. Therefore, studies are still to be done in the future, for example, on how to determine the shape of the LSE at the satellite level to separate LST and LSE. Tests with neural network technology show that the constructed network strongly relies on the sample spectral library of emissivity. The more comprehensive the land surface type information covered by the spectral library, the more accurate the estimated LSE. Moreover, accurate atmospheric correction is necessary in our method, therefore how to accurately correct for the atmospheric effects is another issue to improve the LST retrieval accuracy.

Chapter 4. Deep Mixture Model-Based LST Retrieval from Hyperspectral Thermal IASI Sensor

4.1 Introduction

In fact, it's difficult to obtain accurate atmospheric parameters synchronously with TIR measurements. Therefore, some methods are dedicated to providing LST using hyperspectral thermal infrared data without accurate atmospheric correction. Currently proposed ANN methods (Aires et al., 2001)(Filipe Aires et al., 2002)(Wang et al., 2013) for hyperspectral LST inversion are mostly training the limited simulation dataset with one or two hidden layers, which obviously results in low accuracy when applied to satellite data as the simulated data set does not contain all the actual land and atmospheric conditions for satellite data. Deep learning is characterized by neural network involving usually more than two layers and can learn the representative and discriminative features in a hierarchical manner from the dataset. It's greatly effective in object detection (Girshick et al., 2016), image recognition (He et al., 2016) and semantic segmentation (Zhang et al., 2018) for remote sensing. Using deep learning to learn actual satellite data, the accuracy of inversion LST may be improved. However, there are few studies to retrieve LST using hyperspectral thermal infrared data with the deep learning technology. Therefore, in this work, a deep mixture model is discussed and applied to the IASI sensor hyperspectral data to retrieve LST.

This section is organized as follows. The datasets and methodology are presented in section 4.2 and section 4.3, respectively. Section 4.4 analyzes the retrieval result for the training satellite datasets. In Section 4.5, the validation of this method is presented. Finally, the discussion and conclusion are summarized in Section 4.6.

4.2 Datasets

The chosen study areas are located in northern and southern Africa with a variety of land surface coverages and many clear-sky days. The latitude and longitude range of the selected areas are mainly determined by the scanning trajectory of the IASI sensor. The selected northern area and southern area are located on Algeria and South Africa, respectively. Fig.4.1 shows the research areas.

(a) The selected northern area on the Algeria; (b) The selected southern area on South Africa.

Fig.4. 1. Research areas.

IASI observations with different Sensing Start/Stop Times and different viewing zenith angles (VZAs) were collected to train this neural network. In this work, IASI Level 1C product (brightness temperature, Tb) covering all spectral samples was adopted as the input training data of CNN. The AVHRR/MetOp LST product was used as the training target of this deep learning model. We did not choose the commonly used Moderate-resolution Imaging Spectroradiometer (MODIS) LST products as training data for deep learning, because MODIS sensor and IASI sensor on-board on different satellites have a time difference for the research area. AVHRR/MetOp LST product was reprojected according to the mathematic construction of the sinusoidal projection to obtain its latitude and longitude (Snyder, 1987), then it was resampled to the same pixel size for each IASI LEVEL 1C product using spatial-average value.

The time span of the IASI brightness temperature product and AVHRR/MetOp Daily LST product for the training dataset is from January 2016 to December 2018. These three years of datasets were obtained to train and learn

the constructed deep mixture model, the other times data were selected to validate the retrieval accuracy of the model.

4.3 Methodology

The RTE can be expressed as follows (Li et al., 2013):

$$L(\lambda) = \varepsilon(\lambda)\tau(\lambda)B(\lambda, T_s) + (1 - \varepsilon(\lambda))L_{down}(\lambda)\tau(\lambda) + L_{up}(\lambda) \quad (4.1)$$

Where $L(\lambda)$ is the at-sensor radiance at wavelength λ, ε is the surface emissivity, τ is the atmospheric transmittance, L_{up} is the atmospheric upwelling radiance, $L_{down}$is the atmospheric downwelling radiance, $B(\lambda, T_s)$ is the Planck function at surface temperature T_s at wavelength λ (Eq.4.2).

$$B(\lambda, T_s) = \frac{C_1\lambda^{-5}}{\exp(C_2/\lambda T_s) - 1} \quad (4.2)$$

Where, C_1=1.191× 10^8 $W \cdot \mu m^4/(sr \cdot m^2)$ and C_2=1.439× 10^4 $\mu m \cdot K$.

$L(\lambda)$ can be expressed as $B(\lambda, T_b)$, the Planck function at brightness temperature T_b. From Eq.4.2, we know that is a complex nonlinear relationship exists between brightness temperature and surface temperature. Consequently, a deep mixture model that can learn complex pattern was employed to retrieve LST directly.

4.3.1 Channel selection

Due to the large amount of data for deep learning training and the strong correlation between channels for hyperspectral data, selection of an optimal subset of the IASI channels is one of the most important factors that affects the computation efficiency and the retrieval accuracy in actual inversion. Many channel selection schemes considering IASI sensor have been proposed according to different kinds of purposes (Martinet et al., 2014)(Ventress and Dudhia, 2014)(Liu et al., 2009)(Collard and Matricardi, 2005)(Collard, 2007), for example atmospheric profiles and cloud properties.

In this work, the smallest number of channels which convey the essential information on the target surface parameters was identified. Considering that some mid-infrared channels are greatly affected by the sun, we only consider 645-1600 cm^{-1} channel in the thermal infrared region. Aires (Filipe Aires et al., 2002)

analyzed the wavelength sensitivity to Ts variations with a channel selection process that defined sensitivity as the mean variation $L(\lambda)$ for 1 K change of Ts. Therefore, for the 645-1600 cm^{-1} spectral region, 245 channels sensitive to the surface characteristics are selected with a threshold of 80 % which realizes a good compromise according to Aires's selection procedure (Fig.4.2).

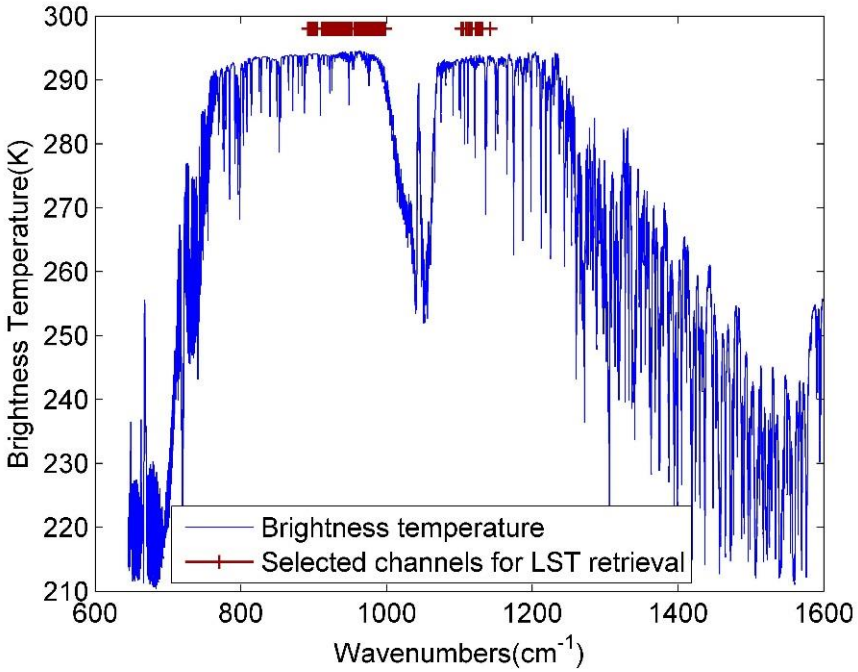

Fig.4. 2. Selected Channels for IASI data.

4.3.2 Deep mixture model

Deep neural networks (DNN) (Bengio, 2009; Schmidhuber, 2015; Szegedy et al., 2013) and convolutional neural networks (CNN) (Valueva et al., 2020) have significant effects on nonlinear regression problems with large amounts of data. The long-term short-term memory network (LSTM) model (Hochreiter and Schmidhuber, 1997) also has an effect on nonlinear regression of data with temporal relationships, but the effect is not obvious. Combining DNN, CNN and LSTM, these three models can evaluate the characteristics of the data set from global features, local features and time-domain predictions, covering most of the features of the data set. Combining the data of the same dimensions output tensor by the three models into one tensor data and forwarding it, the effect of evaluating and predicting the existing data set will be much higher than that of the single

model. Therefore, this work will use a mixture of these three types of models to invert the surface temperature. Fig.4.3 demonstrates the architecture of the constructed deep mixture model.

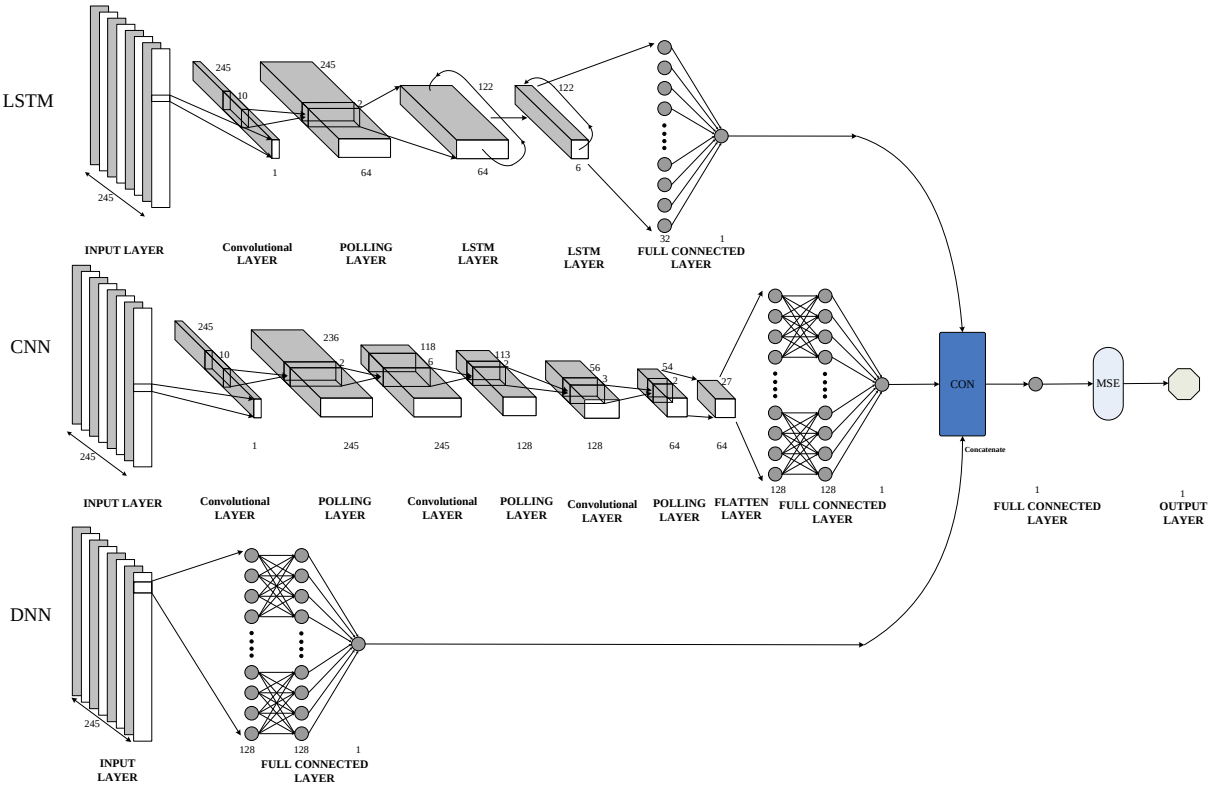

Fig.4. 3. The architecture of the constructed deep mixture model.

The input layer for a CNN ensures that the pixel size is uniform at 1 × 245, which means each satellite brightness temperature pixels have 245 bands; that is, the size of each sample is 1 × 245.

DNN is an artificial neural network (ANN) with multiple layers (≥3). In this part, the deep neural network model uses a three-layer structure, and the hidden layer contains 128, 128, and 1 neuron, respectively. Sigmoid function, tanh function and rectified linear unit (ReLU) function (Nair and Hinton, 2010) are typical activation functions. In this part, the activation function $f(\cdot)$ adopted ReLU function which trains the neural network faster without a significant penalty to generalization accuracy (Krizhevsky et al., 2012). With the ReLU function, the output does not tend to saturate as the input gradually increases.

This DNN model breaks the spatial information of the data set, compresses the entire data set into a single vector, obtains the global feature information through the calculation of the weight, and forwards it forward, and finally gets a

global feature. Therefore, DNN can be used to obtain global large feature information of satellite image data in a single area.

As a feed-forward artificial neural network, CNN consisted of convolutional layers, pooling layers and fully-connected layers for the multilayer structure (Yu et al., 2017). It uses local connections to effectively extract information from data and reduce the number of parameters by sharing the weights. The number of the alternately arranged convolutional layers and pooled layers can be adjusted according to the retrieval target. The convolutional layer is used to learn feature representations of the inputs data as a core part. The feature for the lth layer (convolution layer) is obtained using convolution and activation operations with trainable parameters (i.e., the weight term W_k and bias term b_k) and activation function $f(\cdot)$. The trainable parameters are initialized randomly subject to a uniform distribution. Mathematically, the feature value in the k-th feature of l-th layer, X_k^l is calculated by the following equation:

$$X_k^l = f(\sum_{i=1}^{K} W_{(i,k)}^l \cdot X_i^{l-1} + b_k^l) \tag{4.3}$$

Here X_i^{l-1} is K features for the $(l-1)$th layer $(i = 1,2,\dots,K)$. The convolution kernel W_k^l is a weight matrix whose size and number are manually specified. The three convolutional layers contain 245, 128, and 64 convolution kernels, respectively, and the corresponding convolution window widths are 10×1, 6×1, and 3×1. The activation function $f(\cdot)$ adopted ReLU function. The pooling layer, usually placed between two convolutional layers, performs a down-sampling operation to achieve shift-invariance. In this part, the max-pooling operations (Boureau et al., 2010) was adopted. The pooling kernel is set to a matrix size of 2. At last, the high-level reasoning of the neural network is done via a fully connected layer with three sets of convolution and pooling layers in this architecture. Neurons in a fully connected layer have connections with all activations in the previous layer. To maintain the stability of the CNN, the neural network node activation function at the fully connected level also uses the ReLU function.

CNN retains the spatial information of the data set, intercepts it into multiple local sub-data sets, obtains its corresponding feature information by refining the weights of the sub-data sets, and forwards them one by one. Finally, the spatial

structure is restored and integrated according to the local features of the obtained sub-dataset for evaluation. Therefore, CNN can be used to capture the details of satellite data in a single region.

LSTM is a recurrent neural network model that can learn long-term dependencies and is used to process and predict important events with very long intervals and delays in time series. Therefore, we use LSTM to analyze and predict satellite data in a single area in the time domain. In this part, the LSTM model is created according to the CONVOLUTIONAL, LONG SHORT-TERM MEMORY, FULLY CONNECTED DEEP NEURAL NETWORKS (CLDNN) model (Sainath et al., 2015) (Fig.4.4). The general structure of the CLDNN is that the input layer is a time-domain-related feature. It connects several layers of CNN to reduce the frequency domain change, the CNN output is poured into several layers of LSTM to reduce the time domain change, and the output of the last layer of LSTM is input to full connected the DNN layer, which maps the feature space to an output layer that is easier to classify.

The CNN part of the LSTM model created in this work uses a one-dimensional convolution layer (time-domain convolution), 64 feature maps, and a time-frequency domain filter with a size of 9×1. The input shape size of this layer is 245×1, the pooling layer between the layers adopts the max-pooling strategy (Boureau et al., 2010), and the pooling size is 2×1. The inter-layer dataset is processed for batch normalization (Ba et al., 2016; Ioffe and Szegedy, 2015; Santurkar et al., 2018). The CNN layer is followed by 2 LSTM layers, the first LSTM layer uses 6 cells, the input shape size of this layer is 122×64, the output shape size is 122×6. The second LSTM layer uses 32 cells, and the input shape size of this layer is 122×6, the output shape size is 32×1. The output of LSTM was connected to two fully connected layers with 32 and 1 neurons, respectively.

The output tensors from the DNN, CNN, and LSTM model are spliced into a tensor, which is then passed to the output layer of this mixed model through a fully connected layer with a single neuron. The three models are fused into a mixed model to process complex satellite observations and perform corresponding surface temperature inversion. The combination of the three models uses the Mean square error (MSE) as a loss function, and the layers' functional Equation is as follows:

$$MSE(y, y') = \frac{\sum_{i-1}^{n}(y_i - y_i')^2}{n} \tag{4.3}$$

Where, y_i is the target answer of the i-th data in a training batch, and y_i' is the retrieval value given by the deep mixture model. The Adam (adaptive moment estimation) algorithm (Da, 2014) was adopted as a gradient descent algorithm for this deep mixture model backpropagation stage. Adam is straightforward to implement and requires little memory. Adam is known to be robust and well-suited to a wide range of non-convex optimization problems in the field of machine learning (Daxini and Prajapati, 2020).

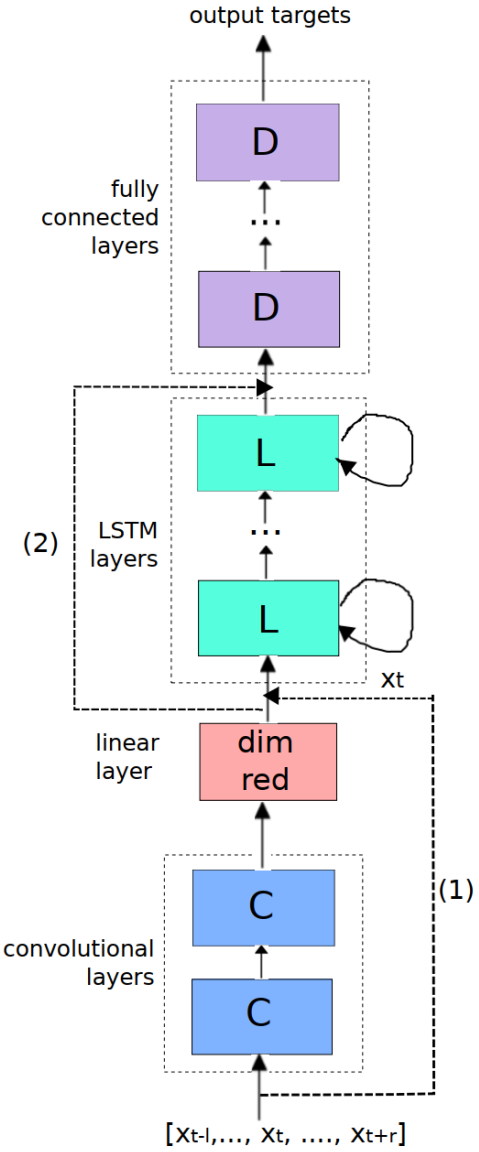

Fig.4. 4. CLDNN Architecture (Sainath et al., 2015).

4.4 Results

To evaluate the accuracy and practicability of deep LST retrieval, the IASI brightness temperature and AVHRR/MetOp Daily LST products were established as the training and test datasets. For the training dataset of the research area, 90% dataset was adopted as the training data, and 10% dataset was used as the test dataset of this deep mixture model. To validate the deep method retrieval accuracy, RMSE is adopted: it represents the root mean square error of the retrieved LST and actual LST. The histogram of the residuals between the values retrieved using deep mixture model and the AVHRR/MetOp Daily LST products was demonstrated. The residuals between the retrieved LST and the AVHRR/MetOp Daily LST products for the selected two areas are mainly located at ±5 K (Fig. 4.5). RMSE indicated that the LST in Algeria and South Africa could be retrieved with an accuracy of <2 K and 2.5 K, respectively, using this deep mixture model validated with the test dataset. The RMSE of LST for South Africa is large than northern Africa LST retrieval result. One possible reason is that the selected area for South Africa land surface types is more heterogeneous than the selected northern Africa, the surface of northern Africa is more uniform. In the following sections, this deep mixture mode with good estimation will be used to provide the LST estimation for the data at other times.

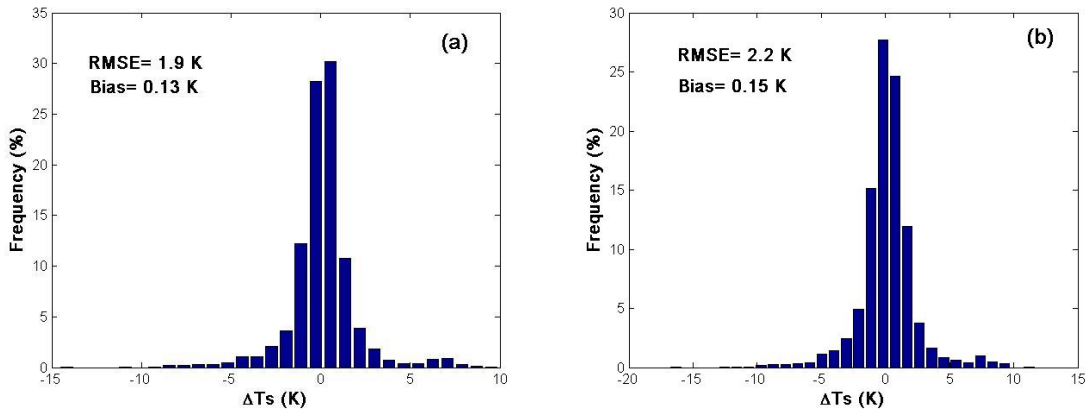

Fig.4. 5. The histogram of the residuals between the values retrieved using deep mixture model and the AVHRR/MetOp Daily LST products. (a) for northern Africa; (b) for southern Africa.

4.5 Validation

The constructed deep mixture model aforementioned was applied on other times IASI real observations to give the LST estimation. Four seasons IASI Tb data in the selected two areas are adopted to validate the retrieval accuracy of LST. For the research area on northern Africa, the daytime data and nighttime data were obtained on March 1, 2019 (at 09:21:40–09:24:09 UTC and 20:35:24–20:38:04 UTC). For the research area on southern Africa, the nighttime data and daytime data were obtained on December 1, 2019 (at 07:38:01–07:39:36 UTC and 20:00:09–20:01:44 UTC). The selected two areas are mostly clearly-sky on these days. Fig.4.6 and Fig.4.7 show the inversion value of LST with the deep mixture model for the daytime and nighttime data of the selected two areas.

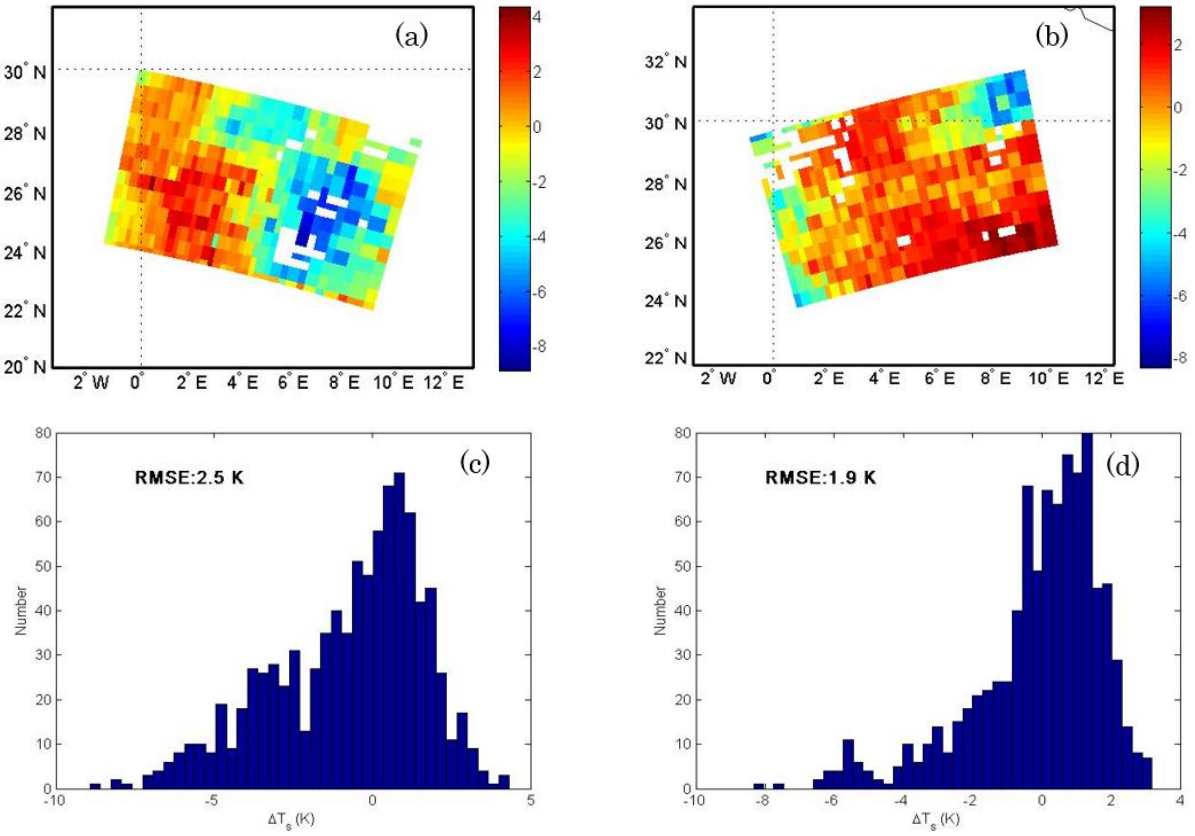

Fig.4. 6. Retrieved LST for the northern Africa on March 1, 2019. (a) The difference between the retrieval LST and AVHRR/MetOp Daily LST product for the daytime data. (b) The difference between the retrieval LST and AVHRR/MetOp Daily LST product for the nighttime data. (c) Histogram of the residuals between the retrieval LST and AVHRR/MetOp Daily LST product for the daytime data. (d) Histogram of the residuals between the retrieval LST and AVHRR/MetOp Daily LST product for the nighttime data.

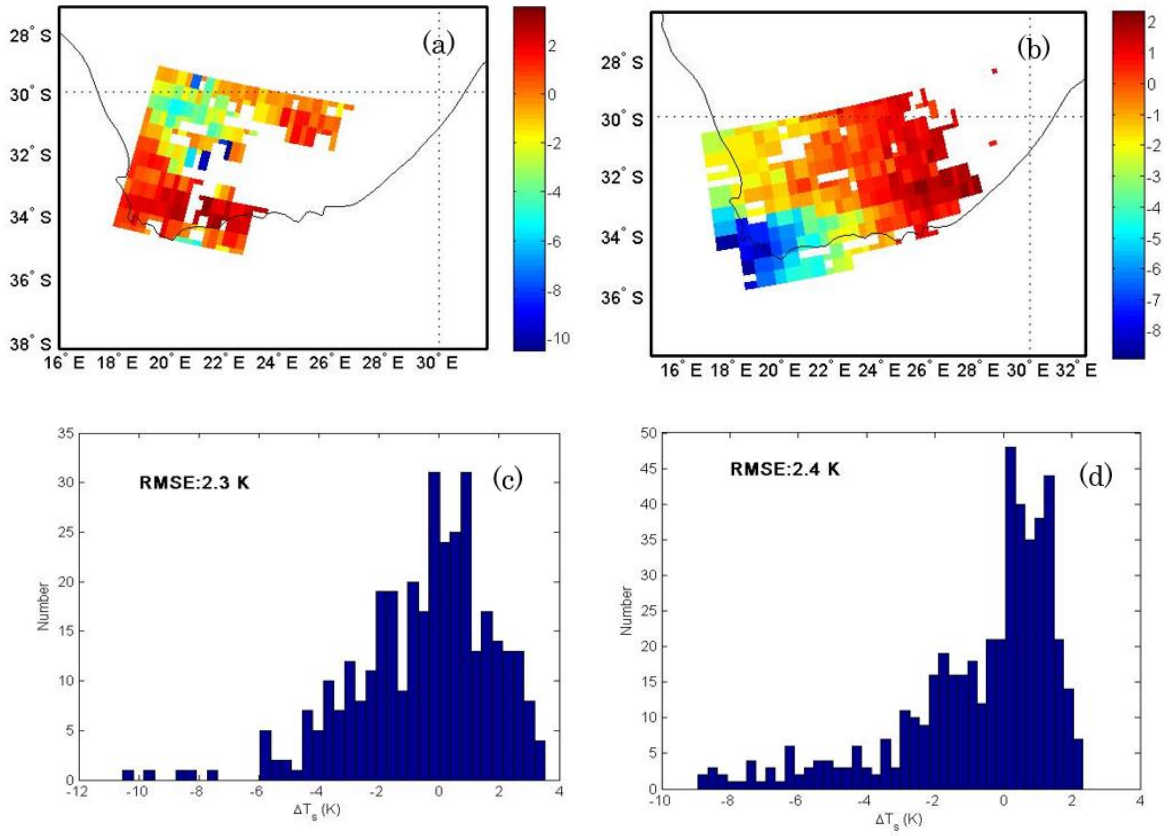

Fig.4. 7. Retrieved LST for the southern Africa on December 1, 2019. (a) The difference between the retrieval LST and AVHRR/MetOp Daily LST product for the daytime data. (b) The difference between the retrieval LST and AVHRR/MetOp Daily LST product for the nighttime data. (c) Histogram of the residuals between the retrieval LST and AVHRR/MetOp Daily LST product for the daytime data. (d) Histogram of the residuals between the retrieval LST and AVHRR/MetOp Daily LST product for the nighttime data.

Compared with AVHRR/MetOp LST product, the LST could be retrieved with an accuracy of < 3 K for March in northern Africa (Fig.4.6a, Fig.4.6b, Fig.4.6c and Fig.4.6d) and < 2.5 K for December in southern Africa (Fig.4.7a, Fig.4.7b, Fig.4.7c and Fig.4.7d). The LST retrievals at night had an accuracy of < 2.5 K compared with AVHRR/MetOp LST product and were better than those from during the day for northern Africa. One possible reason for this result is that surface temperature is more uniform for nighttime. However, for the southern Africa, the retrieval RMSE of LST for the nighttime is slightly larger than the daytime data. This is mainly due to the small number of clear-sky pixels for the daytime data. It can be concluded that this deep learning model can provide relatively accurate LST estimation.

4.6 Summary and Conclusion

This part introduced a deep mixture model to provide LST estimation for IASI hyperspectral data. The relationship between the IASI observations (brightness temperature) and the LST was learned by deep learning. The constructed deep mixture model combines the advantages of Deep Neural networks (DNN) and Convolutional Neural network (CNN) for extracting features of training data and Long Short-Term Memory (LSTM) model for sequence prediction.

For the training dataset of the research area, 90% dataset was adopted as the training data, and 10% dataset was used as the test dataset of this deep mixture model. The results showed that RMSEs of LST were < 2.5 K. This method was also applied to other times IASI real observations. RMSEs of LST for the selected areas are < 3 K validating the corresponding AVHRR/MetOp LST product. Therefore, our constructed deep mixture model can be used to determine LST with a good retrieval accuracy. The accuracy of the validation result for 2019 is mostly lower than the training dataset, this is mainly because the mean and variance of the training dataset (2016-2018, three years) has a small deviation with the 2019 validation data. This will affect the results of deep learning model inversion. Collecting training data on a large time scale may improve the accuracy of the validation, thus it can be discussed in future limited by the time of data collection and calculation processing. Compared to the PES-LSEC method in third section, it does not require any atmospheric information but it needs a large amount of satellite data to train and learn for the network. Therefore, it takes a lot of time to collect and process data. If we want to discuss the LST retrieval for large-scale area, high requirements on data volume and computing performance are problems. Furthermore, the retrieval accuracy was only validated with the AVHRR/MetOp LST product, more satellite data products and ground measurement data could be collected to further discuss the evaluation problems.

Chapter 5. LST Retrieval from Hyperspectral Thermal IASI Sensor Using a physical method

5.1 Introduction

Obtaining accurate atmospheric parameters synchronously with TIR measurements is very difficult. How to obtain the LST information without accurate atmospheric correction is a key issue. Nowadays, regression retrieval method (Goldberg et al., 2003; Zhou et al., 2011, 2002), multi-channel method (Zhong et al., 2016, 2015), artificial neural network (ANN) method (Aires et al., 2001; Aires et al., 2002; Chen et al., 2019; Wang et al., 2013) and the physical retrieval methods (Aires et al., 2002a, 2002b; Li et al., 1994, 2007; Ma et al., 2002, 2000, 1999; Masiello and Serio, 2013; Paul et al., 2012) provide solutions to obtain the LST without accurate atmospheric correction from hyperspectral thermal infrared data. The regression retrieval method considers the linear/nonlinear empirical relation between the LST and brightness temperature at the top of atmosphere. It is computationally efficient for near real-time applications and can be used as the first estimate for the physical retrieval (Péquignot et al., 2008). The multi-channel method with a small number of channels can be used to estimate the LST, but it requires that the minimum channel LSE in the spectral interval of 800–950 cm–1 is larger than 0.95 and has not been extended for off-nadir measurements (Zhong et al., 2016). To simultaneously retrieve the LST, LSE, and atmospheric parameters, the representatives of these ideas are ANN method (Wang et al., 2013) and the two-step physical retrieval method (Ma et al., 2002, 2000). The ANN can learn and recognize complex nonlinear patterns and establish more complex relationships between independent and dependent variables without information about complex physics mechanisms (Mas and Flores, 2008). However, architecture-related parameters are still required to test different problems, although one or two hidden layers are enough for most problems (Sontag, 1992). The two-step physical retrieval method is based on an RTE linearized using

the tangents around the initial estimates of the LST, LSE, and atmospheric parameters. Principal component analysis in combination with the Tikhonov regularization method can be utilized to reduce the number of unknowns and stabilize the ill-posed problem (Smith and Woolf, 1976)(Ma et al., 2000). This method yields good LST estimates after updating the initial estimates, but it considers the complex vertical structure of the atmospheric profile. In this paper, a new simple two-step physical retrieval method is proposed, which can be used to relinearize the RTE to obtain an LST with good accuracy from IASI data. The application of this new method to IASI observations (brightness temperature) shows that the LST can be retrieved without any prior land surface and atmospheric information.

The methodology is presented in section 5.2. Section 5.3 describes the simulated numerical experiment and sensitivity analysis. In Section 5.4, this method is applied to satellite data, the validation is presented. Finally, the conclusions are summarized in Section 5.5.

5.2. Methodology

Following the concept of the two-step physical retrieval method, we only consider the inversion of the surface temperature but not the retrieval of the atmospheric profile. Therefore, we only pay attention to the effect of the atmosphere on the inversion of the surface temperature. Instead of the temperature and humidity of each layer of the profile, the parameters for atmospheric equivalent temperature (Ta) and water vapor content (q) were utilized to simplify the retrieval method.

5.2.1 Linearized form of the RTE

The at-sensor radiance R_λ at wavelength λ can be described as the following equation (Li et al., 2013):

$$R_\lambda = \varepsilon_\lambda B_\lambda^{Ts} \tau_\lambda + R_\lambda^{up} + (1-\varepsilon_\lambda) R_\lambda^{down} \tau_\lambda \quad (5.1)$$

Where ε_λ is the LSE, B_λ^{Ts} is the Planck function B at surface temperature Ts, τ_λ is the atmospheric transmittance, R_λ^{up} is the atmospheric upwelling radiance,

R_λ^{down} is the atmospheric downwelling radiance. Eq.5.1 can be further approximated as (Qin et al., 2001):

$$B_\lambda^{Tb_\lambda} = \varepsilon_\lambda B_\lambda^{Ts}\tau_\lambda + (1-\tau_\lambda)B_\lambda^{Ta_\lambda} + (1-\varepsilon_\lambda)\tau_\lambda(1-\tau_\lambda^{50})B_\lambda^{Ta_\lambda} \tag{5.2}$$

Where, $B_\lambda^{Tb_\lambda}$ is the Planck function B at brightness temperature Tb_λ. $B_\lambda^{Ta_\lambda}$ is the Planck function B at atmospheric equivalent temperature Ta_λ. τ_λ^{50} is the atmospheric transmittance with the viewing zenith angle 50°. The first order variation of Eq.5.2 yields:

$$\begin{aligned}\delta B_\lambda^{Tb_\lambda} = {} & \delta B_\lambda^{Ta_\lambda}(1-\tau_\lambda^{50}\tau_\lambda-\varepsilon_\lambda\tau_\lambda+\varepsilon_\lambda\tau_\lambda^{50}\tau_\lambda) + \delta\varepsilon_\lambda(B_\lambda^{Ts}\tau_\lambda-\tau_\lambda B_\lambda^{Ta_\lambda}+B_\lambda^{Ta_\lambda}\tau_\lambda\tau_\lambda^{50}) + \delta B_\lambda^{Ts}(\varepsilon_\lambda\tau_\lambda) \\ & +\delta\tau_\lambda(\varepsilon_\lambda B_\lambda^{Ts}-\tau_\lambda^{50}B_\lambda^{Ta_\lambda}-\varepsilon_\lambda B_\lambda^{Ta_\lambda}+\varepsilon_\lambda\tau_\lambda^{50}B_\lambda^{Ta_\lambda}) + \delta\tau_\lambda^{50}(\varepsilon_\lambda B_\lambda^{Ta_\lambda}\tau_\lambda-\tau_\lambda B_\lambda^{Ta_\lambda})\end{aligned} \tag{5.3}$$

τ_λ and τ_{50} are approximated as $a_\lambda * e^{\frac{-k_\lambda q}{\cos\theta}}$ and $a_\lambda * e^{\frac{-k_\lambda q}{\cos 50^\circ}}$, respectively. Where, q is water vapor content. θ is viewing zenith angle. a_λ and k_λ are fitting coefficient and extinction coefficient, respectively, which are wavelength-dependent. Setting $\alpha_\lambda = \frac{\partial B_\lambda/\partial Ta_\lambda}{\partial B_\lambda/\partial Tb_\lambda}$, $\beta_\lambda = \frac{\partial B_\lambda/\partial Ts}{\partial B_\lambda/\partial Tb_\lambda}$, then Eq.5.3 can be written as:

$$\delta Tb_\lambda = W_{Ta_\lambda}\delta Ta_\lambda + W_{\varepsilon_\lambda}\delta\varepsilon_\lambda + W_{Ts_\lambda}\delta Ts + W_{q_\lambda}\delta q \tag{5.4}$$

where,

$$W_{Ta_\lambda} = \alpha_\lambda(1-\tau_\lambda^{50}\tau_\lambda-\varepsilon_\lambda\tau_\lambda+\varepsilon_\lambda\tau_\lambda^{50}\tau_\lambda) \tag{5.5a}$$

$$W_{\varepsilon_\lambda} = \frac{1}{\partial B_\lambda/\partial Tb_\lambda}(B_\lambda^{Ts}\tau_\lambda-\tau_\lambda B_\lambda^{Ta_\lambda}+B_\lambda^{Ta_\lambda}\tau_\lambda\tau_\lambda^{50}) \tag{5.5b}$$

$$W_{Ts_\lambda} = \beta_\lambda(\varepsilon_\lambda\tau_\lambda) \tag{5.5c}$$

$$\begin{aligned}W_{q_\lambda} = {} & -\frac{k_\lambda/\cos\theta}{\partial B_\lambda/\partial Tb_\lambda}(\varepsilon_\lambda B_\lambda^{Ts}\tau_\lambda-\tau_\lambda^{50}B_\lambda^{Ta_\lambda}\tau_\lambda-\varepsilon_\lambda B_\lambda^{Ta_\lambda}\tau_\lambda+\varepsilon_\lambda\tau_\lambda^{50}B_\lambda^{Ta_\lambda}\tau_\lambda) \\ & -\frac{k_\lambda/\cos 50^\circ}{\partial B_\lambda/\partial Tb_\lambda}(\varepsilon_\lambda B_\lambda^{Ta_\lambda}\tau_\lambda\tau_\lambda^{50}-\tau_\lambda B_\lambda^{Ta_\lambda}\tau_\lambda^{50})\end{aligned} \tag{5.5d}$$

Finally, for the given observation with N channels (wavelength $\lambda_i, i = 1, \dots, N$), the system of N equations can be expressed in its matrix form as:

$$\delta y = W\delta x \tag{5.6}$$

where,

$$\delta y = \begin{bmatrix}\delta Tb_{\lambda_1} \\ \vdots \\ \delta Tb_{\lambda_N}\end{bmatrix}, \tag{5.7a}$$

$$W = \begin{bmatrix} W_{Ta_{\lambda_1}} & \cdots & 0 & W_{\varepsilon_{\lambda_1}} & \cdots & 0 & W_{Ts_{\lambda_1}} & W_{q_{\lambda_1}} \\ \vdots & \ddots & \vdots & \vdots & \ddots & \vdots & \vdots & \vdots \\ 0 & \cdots & W_{Ta_{\lambda_N}} & 0 & \cdots & W_{\varepsilon_{\lambda_N}} & W_{Ts_{\lambda_N}} & W_{q_{\lambda_N}} \end{bmatrix}, \tag{5.7b}$$

$$\delta x = \begin{bmatrix} \delta Ta_{\lambda_1} & \cdots & 0 \\ \vdots & \ddots & \vdots \\ 0 & \cdots & \delta Ta_{\lambda_N} \\ \delta\varepsilon_{\lambda_1} & \cdots & 0 \\ \vdots & \ddots & \vdots \\ 0 & \cdots & \delta\varepsilon_{\lambda_N} \\ \delta Ts & \cdots & \delta Ts \\ \delta q & \cdots & \delta q \end{bmatrix}. \tag{5.7c}$$

The above linearized form Eq.5.6 is always underdetermined regardless of the number of channels (2N+2 unknowns for N channels). To make the system of equations solvable, it is necessary to reduce the number of unknowns. Because there is a strong correlation between the channels for Ta and emissivity, PCA is commonly used to reduce the dimensions of Ta and LSE by using eigenvalues and eigenvectors (Singh, 1993). Finally, Eq.5.6 can be expressed as the following Eq.5.8:

$$\delta y = W\delta x = WVf = W^D f \tag{5.8}$$

where, the terms V and f are the eigenvector matrix and coefficient vector of δx, respectively. Many simulated Ta and spectral LSE values are employed to derive a statistical covariance matrix to obtain the eigenvectors of Ta and LSE (m eigenvectors for Ta and t eigenvectors for q). The eigenvector of LST and q is assumed to be a unit vector. Therefore, the corresponding coefficient vector f contains m coefficient vectors of Ta, t coefficient vectors of emissivity, one for LST and one for q.

To stabilize this ill-posed problem, Tikhonov regularization estimate (Tikhonov and Arsenin, 1977) can be used, which is the solution to the following minimization problem:

$$argmin \parallel \delta y - W^D f \parallel_2^2 + \gamma^2 \parallel Lf \parallel_2^2 \tag{5.9}$$

Where, γ is a regularization parameter given by the L-curve method (Hansen and O'Leary, 1993), L is a side constraint matrix. The second term in Eq.5.9 is called the "regularizer" or "side constraint" and captures prior knowledge about the expected behavior of f. When the initial estimates of atmospheric and surface parameters have been updated using Tikhonov regularization, we can further

optimize the solution of the equation by iterative methods. The discrepancy principle iteration algorithm (Huang and Li, 2000) is used with the regularized solution as the initial guess to obtain the final maximum likelihood solution of the LST. A detailed introduction about the discrepancy principle (DP) iteration can be found in (Huang and Li, 2000).

Compared to the two-step physical method (Ma et al., 2002, 2000) that takes into account the stratified atmospheric profile, our proposed physical method adopted Ta and q to explore the total impact on LST. The RTE was tangent-linearized around the initial guess with respect to the surface temperature, LSE, Ta and q, which is simpler with the aim of retrieving surface temperature.

5.2.2 Channel selection

Because of the large amount of data and the strong correlation between channels for hyperspectral data, channel selection is one of the important factors that affects the computation efficiency and the retrieval accuracy in real inversion. For the IASI sensor data that we discussed, (Collard, 2007; Collard and Matricardi, 2005) provide a conservative but near-optimal set of channels for the physical retrieval of the atmospheric state. Many channel selection schemes have been proposed for the IASI for different purposes (Liu et al., 2009; Martinet et al., 2014; Ventress and Dudhia, 2014). The selection of an optimal subset of IASI channels is an established approach to reduce the significant computational costs of data processing and to identify the smallest number of channels that convey essential information about the target surface parameters.

Initial estimation was utilized to select retrieval channels for each simulated observation for the physical method. Aiming at providing an accurate LST retrieval result, the channel selection scheme must be conducted to the LST retrieval. In this study, the specific channel selection scheme dynamically varies depending on the LST weight value W_{Ts_λ} of the weight matrix (W) calculated from the initial estimate; channels with larger LST weights were selected. In total, 765 channels sensitive to the surface characteristics were selected with large W_{Ts_λ}(top 20%), representing a good compromise. Although several mid-infrared channels were selected in IASI technical documentation, we only utilized the 645–1600 cm–

[1] channel in the thermal infrared region considering that most of these channels are significantly affected by the sun.

5.3. Experiments with simulated data

5.3.1 Simulation of IASI Radiances

To evaluate the proposed method, the simulated datasets are used to fulfill and analyze this physical algorithm in this section. The parameters in the linearized process of RTE can be simulated using the hyperspectral atmospheric radiative transfer model 4A/OP (Chaumat et al., 2012; Scott and Chedin, 1981) with the input atmospheric profiles selected from the TIGR data set, and the input emissivity spectrum from the ASTER spectral library (A. M. Baldridge et al., 2009). In this experiment, only clear-sky atmospheric profiles were taken into account. Thus, the relative humidity of each layer of the atmosphere profile greater than 90% was considered to be cloudy (Galve et al., 2008). Finally, 946 atmospheric profiles, with the bottom atmospheric temperature ($T_{\_bat}$) varying between 230 K and 320 K and q ranging from 0.1 to 6.5 g/cm^2 were selected from TIGR database (Fig.5.1). 65 emissivity spectra (52 soil types, 4 vegetation types, 9 water/snow/ice types) were chosen to describe most of the land surface features (Fig.5.2). To make the simulation more representative, the LST was given by the $T_{\_bat}$ of profiles that varied from $T_{\_bat}$ –10 K to $T_{\_bat}$ +15 K in steps of 5 K for $T_{\_bat} < 280$ K, and from $T_{\_bat}$ –5 K to $T_{\_bat}$ + 20 K in steps of 5 K for $T_{\_bat} \geq 280$ K. Finally, 737880 different situations were obtained.

4A/OP is a line-by-line model that realizes the fast simulation of the radiative transfer with a “pseudo-infinite” (high) resolution especially suitable for the IASI sensor simulation in the infrared range. It can simulate the atmospheric upwelling radiance, downwelling radiance and transmittance with a certain observation geometry, and then combine the surface temperature and emissivity to calculate the observed brightness temperature using the RTE. At present, our physical method only discusses simple near-vertical observation without considering the angular dependence of the top of atmosphere radiance. Therefore, the simulated datasets only include satellite near-vertical observations.

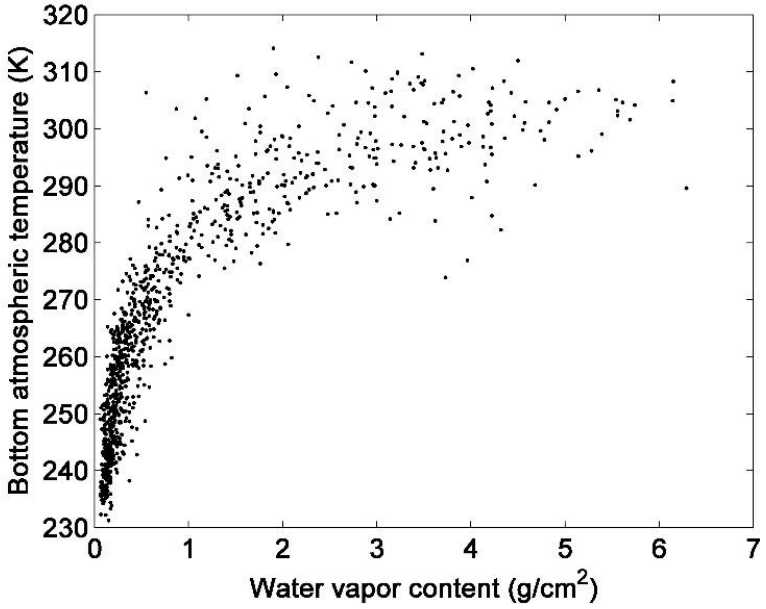

Fig.5. 1. The scatter plot of the bottom atmospheric temperature and water vapor content for the selected atmospheric profiles.

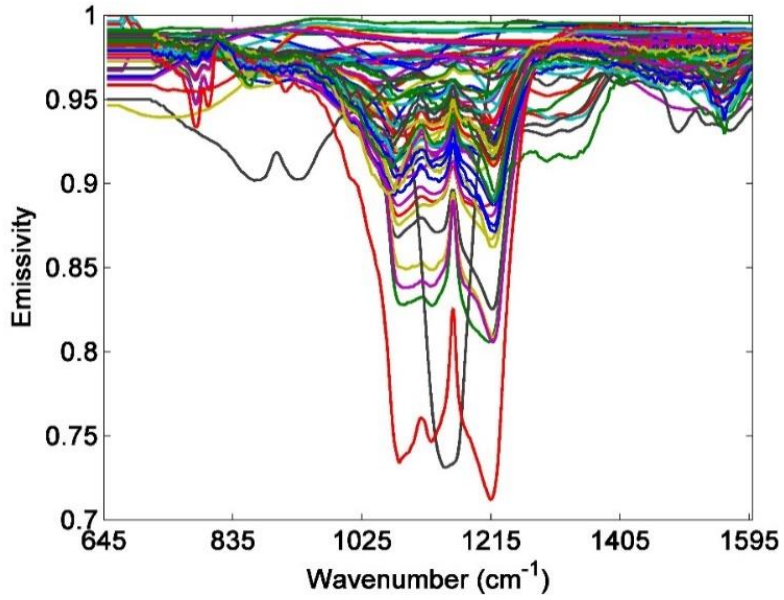

Fig.5. 2. Selected emissivity spectra from the ASTER spectral library.

The spectral range of the simulated data sampled at 0.25 cm^{-1} (3821 bands) is 645–1600 cm^{-1}. The instrument Spectral Response Function was set to be the same as IASI sensor (Tournier and Camy-Peyret, 2003). For the real IASI observation, the instrument noise existed in the measurement and can be simulated by a white Gaussian noise with a noise equivalent temperature (NEΔT) at 280 K (Filipe Aires et al., 2002). At last, this instrument noise was added to the simulated observed

brightness temperature as parameter Tb_λ. The flow diagram for dataset simulation is demonstrated in Fig.5.3.

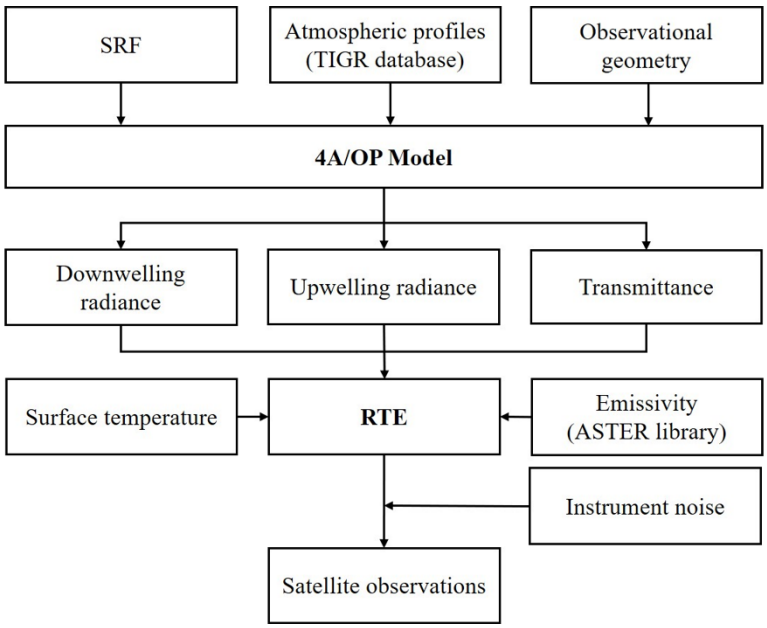

Fig.5. 3. Flow diagram for dataset simulation.

5.3.2 Initial estimates

As shown in Eq.5.4, the linearized RTE must be physically solved using an initial value close to the true value. The initial geophysical parameters serve as first estimates to constrain the numerical solution (Eq.5.9) to obtain physically reasonable results. Two methods can be used to obtain the initial estimates, that is, regression and ANN, which both are statistical or nonphysical retrieval methods (Motteler et al., 1995). The initial estimate is essential for the first calculation of the matrix W; it provides the optimal subset of IASI channels in our proposed method. Compared with the regression method, although the initial value based on the ANN easily generates singular values, its retrieval accuracy is higher (Motteler et al., 1995). Therefore, ANN retrieval was utilized to provide initial estimates in this study (Eq.5.9).

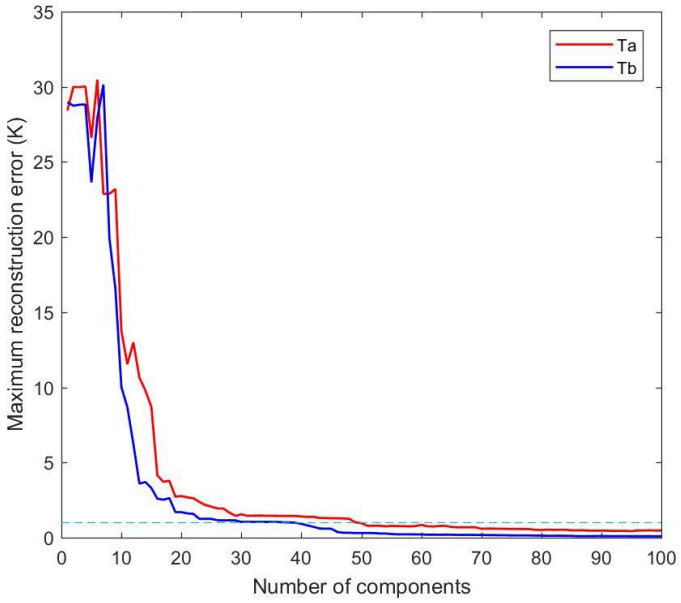

Fig.5. 4. Maximum reconstruction error with different numbers of components for Ta_λ and Tb_λ in the range of 645–1600 cm^{-1}. The blue line represents the maximum difference between the reconstructed brightness temperature and Tb_λ for all channels and the red line is the maximum difference between the reconstructed atmospheric equivalent temperatureand Ta_λ for all channels with different numbers of eigenvectors.

The instrument noise exists in the measurement for the real IASI observation, it can be simulated by a white Gaussian noise with a noise equivalent temperature (NEΔT) at 280 K. The simulated Tb_λ and Ta_λ with 946 atmospheric profiles are processed with the PCA technology to achieve data compression and noise reduction. We analyze the maximum errors produced by compressing Tb_λ and Ta_λ datasets in 645–1600 cm^{-1} with different numbers of eigenvectors. The results show that 40 principal components for Tb_λ and 50 principal components for Ta_λ can limit the reconstructed maximum error to 1 K (Fig.5.4). Finally, 40 principal component (PC) coefficients of Tb_λ were used as the input layer neurons of network and 50 PC coefficients for Ta_λ, one for LST, and one for q were combined as the output layer neurons (Fig.5. 5). Based on Kolmogorov's theorem, the number of hidden layer nodes is $2n + 1$, where n is the number of input layer nodes (Kolmogorov, 1957). Therefore, the constructed neural network contains 81 nodes of the hidden layer. Levenberg–Marquardt backpropagation was utilized to update the weights and biases initialized by the Nguyen–Widrow algorithm (Pavelka and

Procházka, 2004). The results of many experiments showed that a neural network with a hidden layer can solve most of the problems (Sontag, 1992). Therefore, we adopted one hidden layer to test and train this network. A multi-Layer perceptron with one hidden layer was constructed to give the initial estimates of Ts, q and Ta_λ. Tests using a large dataset show that, in contrast to the shape of Ta, the LSE shape of the constructed neural network inversion is mostly incorrect if the samples used for the validation are not part of the training dataset. Therefore, for simplicity, the initial LSE of each channel was assumed to be 0.97. The constant initial LSE (0.97) has a small effect on the results of the LST inversion (a detailed discussion is provided in 5.3.3.1).

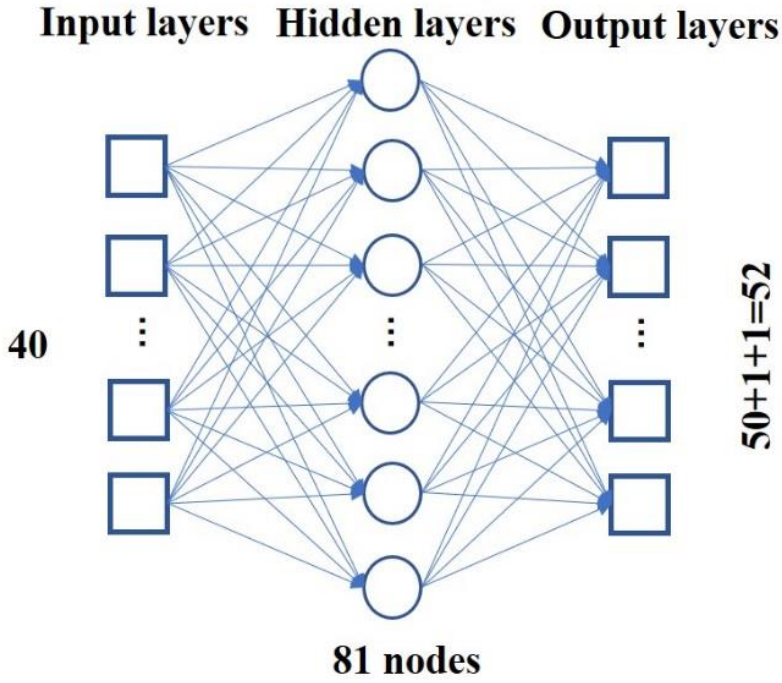

Fig.5. 5. Topological structure of the NN. The input layer contains 40 neurons (40 PC coefficients for brightness temperature). The output layer contains 52 neurons (50 PC coefficients for Ta, one for q, one for surface temperature).

5.3.3 Results and analysis

5.3.3.1 Initial estimation based on the ANN method

For the prepared dataset, the above-mentioned multilayer perceptron provides the initial value as the first iteration of the physical process and the basis for the LST weight channel selection.

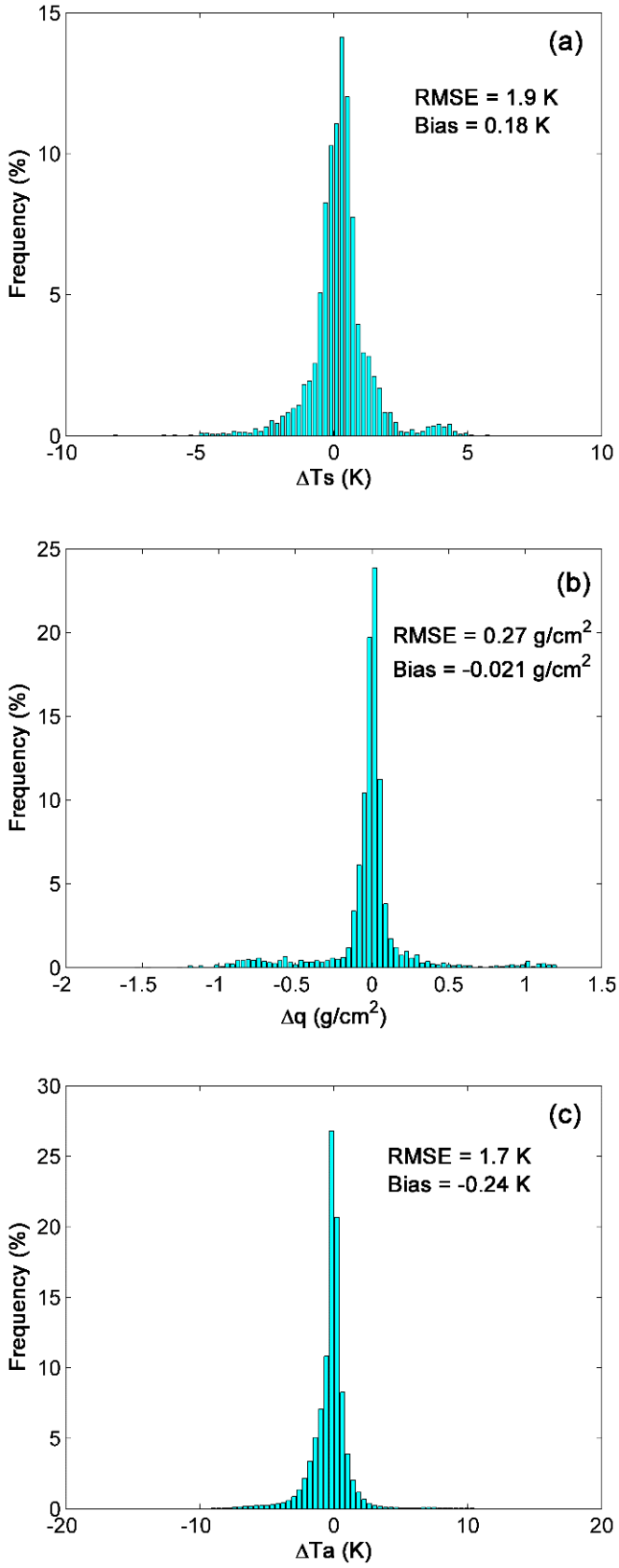

Fig.5. 6. Histogram of the residuals between the values retrieved using ANN method and the true values. a) for LST; b) for q; c) for Ta of all the selected channels.

In the training process, 90% of the simulated data (332046 samples) were adopted as the training dataset of the neural network and 10% of the data (36894 samples) were used as the test dataset. The initial LST estimation indicates that the LST can be retrieved with an accuracy of <2 K based on the ANN method and validation with the test dataset (Fig.5.6a). The constructed multilayer perceptron yields accuracies of ~0.3 g/cm^2 for q and 2 K for Ta of the selected channels (Fig.5.6b, Fig.5.6c). RMSE of Ta was calculated as $\sqrt{(\sum_{i=1}^{N_D}\sum_{j=1}^{N_M}(Ta_{ret,i,j}\text{-}Ta_{true,i,j})^2)/N_D \cdot N_M}$, where Ta_{ret} is the retrieved Ta with the ANN method, Ta_{true} is the true Ta. N_M is the number of bands, and N_D is the number of total samples. Therefore, in the following sections, this multilayer perceptron with good estimation is used to constrain the numerical solution to obtain physically reasonable results.

5.3.3.2 Retrieval result based on the physical method

For the proposed physical method, the channel selection was changed using different initial input values. Fig.5.7 shows an example of a selected channels with large W_{Ts_λ} (top 20%) calculated with the given initial values of the simulated dataset. In this example, the selected channels are mainly located at 700–1000 cm^{-1} and 1100–1300 cm^{-1}. Most of the selected channels of this scheme are less affected by the main absorption molecules in the atmosphere, which is beneficial for surface temperature inversion.

We obtained the difference between the observed brightness temperature and that calculated from the initial estimates using the RTE, called δy. The Tikhonov regularization was used to solve Eq.5.9, where the diagonal constraint matrix L is a combination of multiple identity matrices and the Tikhonov regularization parameter includes solutions with small norms (Ma et al., 2000). Based on the Tikhonov solution (coefficient vector f) and constructed eigenvector matrix V, new estimates of LST, LSE, Ta, and q were obtained. The solution of Eq.5.9 was further optimized by the discrepancy principle iteration algorithm (Huang and Li, 2000), which updates the regularized solution as the initial estimate to obtain the final maximum likelihood solution of the LST. The results of this physical method show

that the LST retrieval accuracy of the physical method is 0.76 K, with an initial estimate error (1.9 K) based on the ANN method (Fig.5.6a, Fig.5.8). Compared with the LST estimation using the ANN, the residuals between the retrieved and true LSTs are ±2 K (Fig.5.8), representing an improvement compared with the ANN (±5 K, Fig.5.6a). The biases of the retrieved LST indicate that the results were overestimated; they have an inversion tendency similar to the ANN biases of the LST. Therefore, based on this physical method, the basic trend of the inversion results of the initial estimates is maintained, but the accuracy is improved. For the simulated test dataset, an improved LST accuracy of 1 K is obtained based on the physical method.

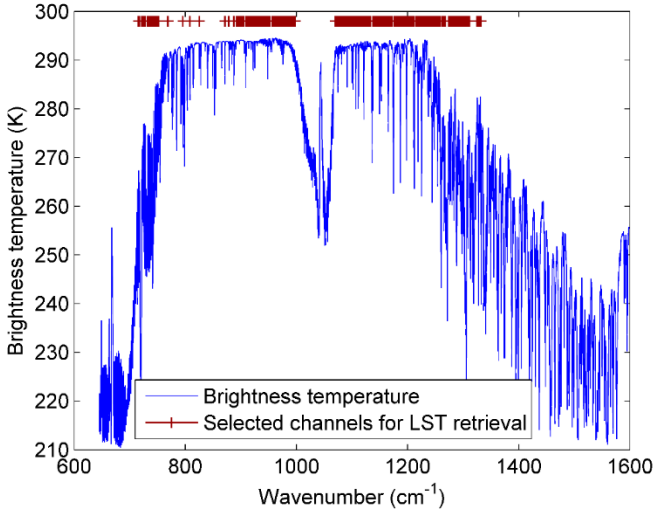

Fig.5. 7. An example of the selected channels for the simulated dataset.

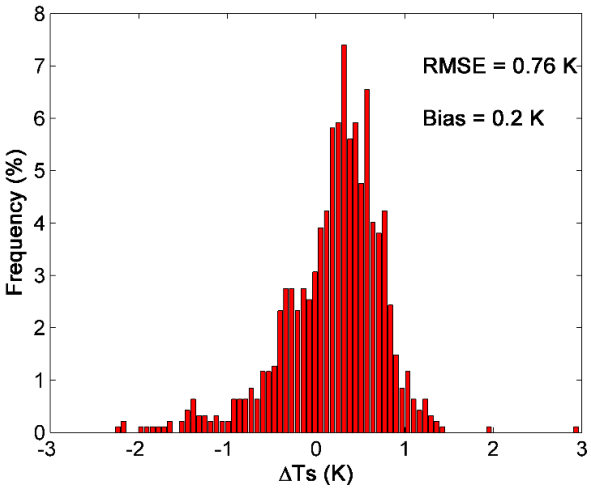

Fig.5. 8. Histogram of the residuals between the retrieved and true LST with the physical method for the simulated dataset.

5.3.3.3 Sensitivity to Instrument Noise

When the ANN method was used to determine the initial value for the previous simulated datasets, the simulated instrument noise has already been added to the brightness temperature. However, the instrument noise was not considered by the following physical method. To better analyze the influence of the instrument noise, the selected channels instrument noise was added to the simulated brightness temperature for the physical retrieval method to be compared to the condition where error was not added. The influence of the instrument noise was presented in Fig.5.9. Retrieval $RMSE_T$ with noise added (0.76 K) is slightly degraded compared to no noise (0.71 K), and the retrieval accuracy is still good. This test indicates that the accuracy of the physical retrieval algorithm is, in general, not highly influenced by a small instrument noise.

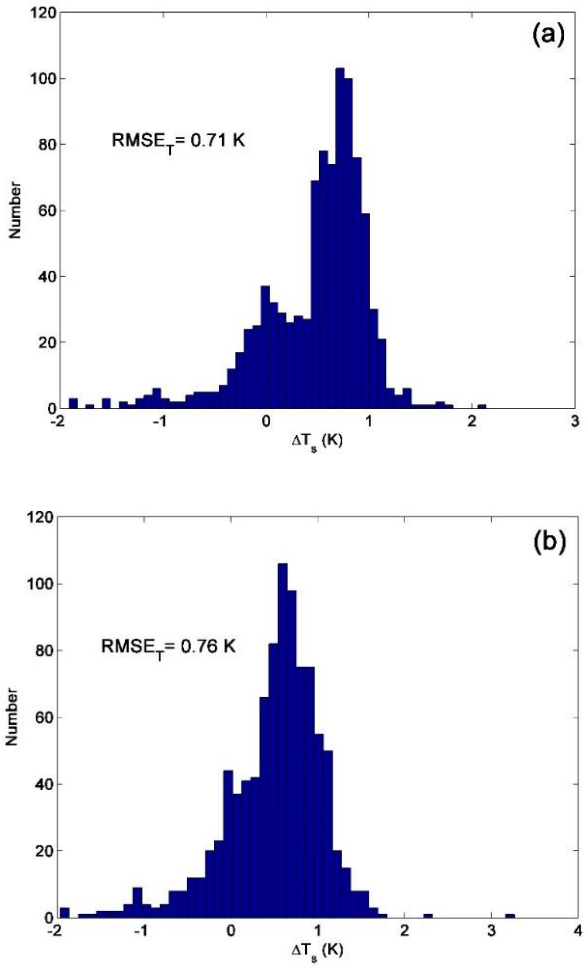

Fig.5. 9. (a) Retrieval LST with no instrument noise. (b) Retrieval LST with instrument noise added.

5.3.3.4 Sensitivity of the LST retrieval to initial unknown values

In this section, the effect of initial unknown estimates on the LST retrieval is discussed. To obtain reasonable statistical results, we selected profiles with a relatively uniform distribution of q of 0–1, 1–2, 2–3, 3–4, 4–5, and >5 g/cm^2. The number of atmospheric profiles in these intervals is equal. Finally, 90 profiles were selected for the sensitivity analysis. To discuss the effects of the initial LSE estimation (LSE_0), initial Ta estimation (Ta_0), and initial q estimation (q_0) errors on the LST retrieval, different error levels were added to the true LSE, Ta, and q. For the initial LST estimation (LST_0), we artificially set the value to deviate from the true LST value with a random error (normal distribution with a mean of 0 K and standard deviation of 0, 1, 3, and 5 K) as the initial estimate to discuss the final LST retrieval accuracy.

5.3.3.4.1 Sensitivity to initial LSE value

Considering that the initial LSE value for each channel was constant (0.97) in the dataset simulated using the physical method, only two types of initial LSE values are used to discuss the effect of the LSE_0 on the LST retrieval: 1) the true LSE value is used as the initial value; and 2) a value of 0.97 is used for each channel as the initial value. Therefore, the constant initial LSE value and actual LSE value with a random LST_0 error (0, 1, 3, and 5 K) are discussed. Note that true values were adopted for Ta and q.

Fig.5.10 shows the RMSEs of the LST, LSE, Ta, and q with a random LST_0 error of 0, 1, 3, and 5 K. The LST retrieval accuracy (RMSE) based on the constant initial LSE slightly increases with the random error of LST_0 (Fig.5.10). When the true values for the LST_0, Ta_0, and q_0 and an LSE_0 value of 0.97 were used for each channel, the LST retrieval yields an error of 0.6 K (RMSE). As the random error of the LST_0 increases to 5 K, the LST retrieval accuracy increases to ~0.7 K. The effect of the LST_0 error (5 K) on the LST retrieval accuracy is small; therefore, the LST_0 estimate RMSE (1.9 K) based on the ANN method is sufficient for the physical method. When the true LST_0, LSE_0, Ta_0, and q_0 values are utilized, the error of the LST estimation is 0.3 K. This error is mainly caused by the linearization of the RTE and the subsequent physical solution process. Therefore,

the constant initial value of the LSE leads to an insignificant accuracy loss (0.3 K) with respect to the LST retrieval using the proposed method. This is why the initial LSE estimate was set to 0.97.

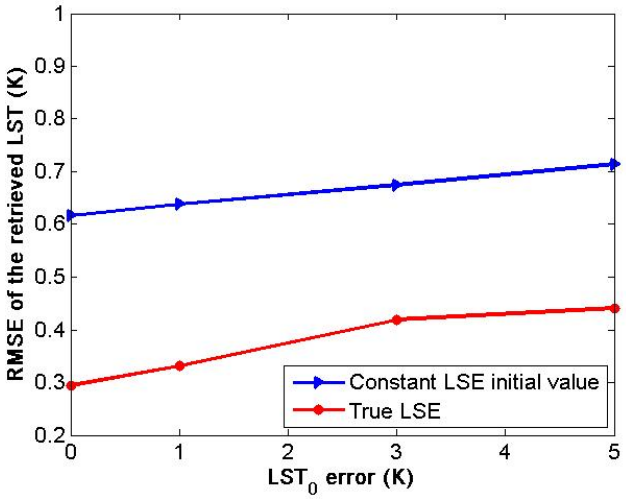

Fig.5. 10. Retrieved RMSE of the LST depending on the random error (0, 1, 3, and 5 K) of the LST_0. True values were used for the q_0 and Ta_0.

5.3.3.4.2 Sensitivity to initial Ta value

Because Ta is related to the LST in the physical method, the accuracy of the retrieved LST based on different levels of errors for Ta was also analyzed. As shown in Fig.5.6c, the maximum channel residual between the retrieved and true Ta_λ is ~20 K based on the ANN estimation. Therefore, in this section, Ta_λ in each channel is scaled to 0.9, 0.95, 1.0, 1.05, and 1.1 times the actual value as Ta_0 to investigate the effect of the initial estimation error on the LST retrieval. True values were used for the LSE and q. As mentioned above, the retrieval accuracy of the true LST based on the addition of a random error of 0, 1, 3, and 5 K as the initial value was discussed.

When real values are used as initial values of the other three unknown variables, a Ta_0 error of +10%, +5%, 0%, −5%, and −10% lead to an approximate LST retrieval accuracy RMSE of 0.65, 0.45, 0.3, 0.36, and 0.5 K; (Fig.5.11). Based on a Ta_0 error of 0% and +10%, the LST can be retrieved within the accuracy of about 0.3 and 0.65 K (Fig.5.11), respectively, using the physical method. A Ta_0 error of 10% results in an LST retrieval accuracy loss of 0.3 K (RMSE; Fig.5.11). Therefore, within the estimated error range of Ta_0 based on ANN, a good accuracy

can be maintained by the inversion of the LST and the error of Ta_0 is insignificantly affected by using real values as initial values for the other three unknown variables.

When true values are used as the initial values of the other two variables (LSE and q), for one level of Ta_0 error, the RMSE error of the LST retrieval increases with increasing LST_0 error (0, 1, 3, and 5 K), but the accuracy insignificantly changes. Fig.5.11 shows that the RMSE of the retrieved LST increases to ~0.7 K as the random error of the LST increases to 5 K for a Ta_0 error of +10%. For a random LST_0 error of 0, 1, 3, and 5 K, the difference between the LST retrieval accuracy with a Ta_0 error of 0% and that with a Ta_0 error of +10% error is only ~0.3 K (Fig.5.11). Thus, within the maximum channel residual based on the ANN method, the LST retrieval accuracy of the physical method is insignificantly affected by the LST_0 error based on the use of true values as initial LSE and q values.

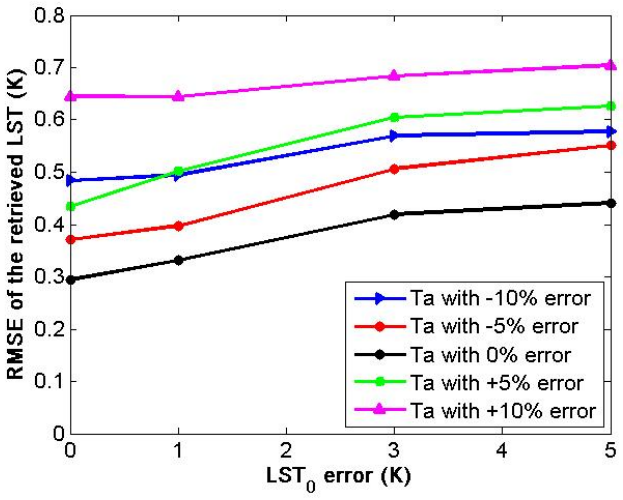

Fig.5. 11. Retrieval accuracy of the LST (RMSE) with Ta_0 errors of −10%, −5%, 0%, +5%, and +10%. True values were used for the LSE_0 and q_0.

5.3.3.4.3 Sensitivity to initial q value

q is commonly discussed for the accurate atmospheric correction of hyperspectral thermal sensor data (Gu et al., 2000)(Young et al., 2002). It is a solution variable in the proposed method (Eq.5.9). Therefore, the effect of its initial estimate on the LST accuracy must be discussed. Considering the accuracy of the initial estimation of the ANN method (Fig.5.6b), we calculated the difference

between the retrieved and true q values. The difference is in the ±40% range. Therefore, relative errors of −40%, −20%, 0%, +20%, and +40% were added to the true q value as the initial value. To study the effects of the LST_0 and q_0 errors on the LST retrieval results, true values were used as the initial values for the other two parameters, that is, Ta and LSE.

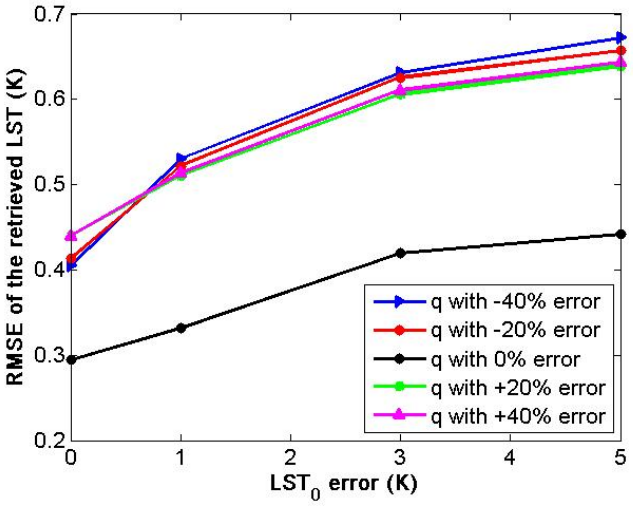

Fig.5. 12. Retrieval accuracy of the LST (RMSE) with q_0 errors of −40%, −20%, 0%, +20%, and +40%. True values were used for LSE_0 and Ta_0.

As shown in Fig. 5.12, the retrieval accuracy of the LST (RMSE) is similar to the retrieval accuracy based on the addition of errors (−40%, −20%, 0%, +20%, and +40%) to the true q as the initial value. Four types of relative q errors (−40%,−20%, +20% and +40%) lead to an LST retrieval error of ~0.4 and 0.65 K based on the addition of a random error of 0 and 5 K, respectively. Based on a random LST_0 error of 0, 1, 3, and 5 K, the difference between the LST retrieval accuracy with q_0 errors of 0% and +10% is ~0.2 K. Because the LST accuracy presents a small difference based on q_0 errors of −40%, −20%, +20%, and +40% at the same error level of LST, the proposed physical method does not require a very high precision regarding the initial estimation of variable q.

5.3.3.4.4 Sensitivity analysis with four initial values

In the above-mentioned three sections, the effects of errors of the initial values of other variables on the LST retrieval accuracy were discussed. To further demonstrate the effect of the initial estimates of the other three variables (LSE_0,

Ta_0, and q_0) on the LST retrieval accuracy, different error combinations were utilized to determine and present the LST retrieval accuracy of the physical method.

Table 5. 1. Retrieved LST accuracy (RMSE) for different kinds of errors for the four initial values.

Initial LST value (K)	Initial LSE value	Initial Ta value (K)	Initial q value (g/cm²)	RMSE of LST (K)
LST with random error =0 K	True LSE	True Ta	True q	0.30
			True q with 40% error	0.44
		True Ta with 10% error	True q	0.57
			True q with 40% error	0.65
	0.97	True Ta	True q	0.61
			True q with 40% error	0.64
		True Ta with 10% error	True q	0.70
			True q with 40% error	0.73
LST with random error =3 K	True LSE	True Ta	True q	0.44
			True q with 40% error	0.61
		True Ta with 10% error	True q	0.68
			True q with 40% error	0.75
	0.97	True Ta	True q	0.67
			True q with 40% error	0.76
		True Ta with 10% error	True q	0.80
			True q with 40% error	0.89

To demonstrate the effects of initial estimates on the LST retrieval accuracy, LST with a random error (0 and 3 K), LSE with a constant initial value (0.97) and true value, Ta with a relative error (0% and 10%), and q with a relative error (0% and 10%) were combined as the initial estimate. As shown in Table 5.1, based on the LST with a random error of 3 K, LSE_0 of 0.97, Ta with a relative error of 10%, and q with a relative error of 40%, the retrieval accuracy of LST is 0.89 K. If all initial values are true values, the retrieval accuracy of LST is 0.3 K. Within the error range of the initial values for the simulated dataset, the LST retrieval accuracy is insignificantly affected by the initial estimates of the unknown variables, whereas an initial value estimate with a better accuracy improves the accuracy of the LST inversion to a certain extent.

5.4 Application to IASI Real Observations

This physical method was applied on the IASI real observations. The brightness temperature (IASI Level 1C product) obtained from the EUMETSAT was selected to retrieve LST directly adopting this physical algorithm. Additionally, to validate the performance of this physical algorithm, the retrieval results of physical method with the selected IASI data are compared to the AVHRRLST product on-board EUMETSAT polar system satellites (MetOp). AVHRR/MetOp LST product was reprojected according to the mathematic construction of the sinusoidal projection to obtain its latitude and longitude (Snyder, 1987), then it was resampled to the same pixel size for each IASI LEVEL 1C product using spatial-average value.

The study areas are located in Spain and North Africa (a variety of land surface coverages, mostly clear sky). The viewing zenith angle (VZA) of the IASI in the study area during the day and night must be smaller than 20° considering the near vertical observation of the proposed physical method. Therefore, limited by the VZA, the daytime and nighttime data were not obtained on the same day. For the study area in Spain, the daytime and nighttime data were obtained on April 27 and 30, 2018, and on October 1 and 2, 2018. The daytime and nighttime data for the study area in North Africa were obtained on January 1 and 2, 2018 and July 1 and 2, 2018.

The constructed ANN aforementioned was firstly used on this real observation to give the initial estimation, then physical method performed iterative solutions. Compared to AVHRR/MetOp LST product, the LST could be retrieved with an accuracy of < 1.1 K for April and October in Spain (Fig.5.13b, Fig. 5.14b, Fig.5.15b and Fig.5.16b) and < 1.3 K for January and July in North Africa (Fig.5.17b, Fig.5.18b, Fig.5.19b and Fig.5.20b). The LST retrievals at night have an accuracy of <1.0 K and are better than those obtained during the day. One reason for this difference might be that the surface temperature is more uniform during the night. The biases of the ANN and physical method indicate that the LST in North Africa was underestimated compared with results obtained from the AVHRR/MetOp LST product. One reason for this underestimation might be that the performance of the

physical method depends on the initial estimate based on the ANN method. The higher ground temperature obtained from the atmospheric profile accounts for a smaller proportion of the overall atmospheric profile, which leads to an underestimation of the initial LST estimate with the ANN method. The LST obtained from the ANN further influences the retrieval result of the physical method. The initial estimate could be improved by identifying and using a more comprehensive and evenly distributed atmospheric profile dataset for the training of the ANN. Another possible reason for the difference is that the projection and spatial resolution of the IASI Level 1C and AVHRR/MetOp Daily LST products differ and reprojection and resampling lead to the loss of accuracy. In addition, the instrument noise of real observations may have an influence on the comparison.

Finally, based on the proposed physical method, the LST retrieval accuracy can be improved to 1.5 and 1 K for daytime and nighttime data of the selected study area compared with the AVHRR/MetOp LST product. It is reasonable to conclude that the application of the proposed physical method to IASI data yields an LST retrieval that coincides with that based on the AVHRR/MetOp LST product.

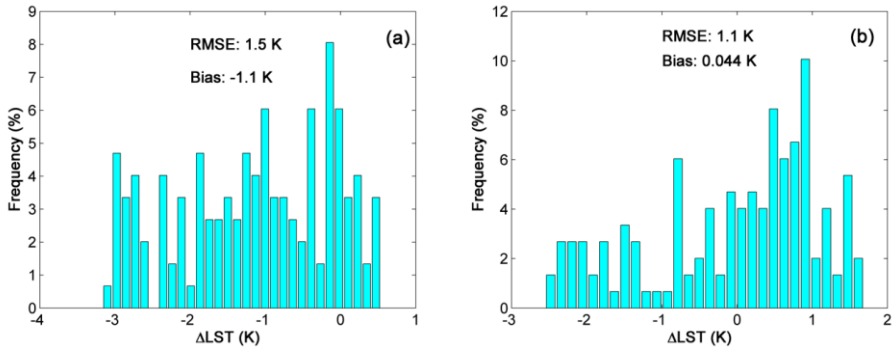

Fig.5. 13. Retrieval results for the daytime data in Spain on April 27, 2018. (a) Histogram of the residuals between the retrieved LST and AVHRR/MetOp LST product with the ANN method. (b) Histogram of the residuals between the retrieved LST and AVHRR/MetOp LST product with the physical method.

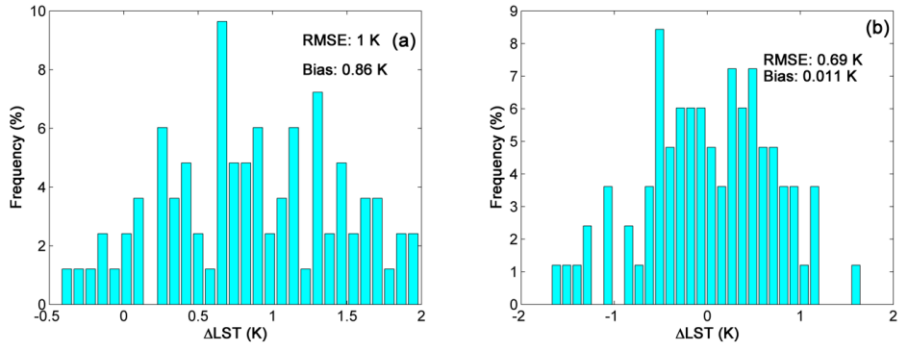

Fig.5. 14. Retrieval results for the nighttime data in Spain on April 30, 2018. (a) Histogram of the residuals between the retrieved LST and AVHRR/MetOp LST product with the ANN method. (b) Histogram of the residuals between the retrieved LST and AVHRR/MetOp LST product with the physical method.

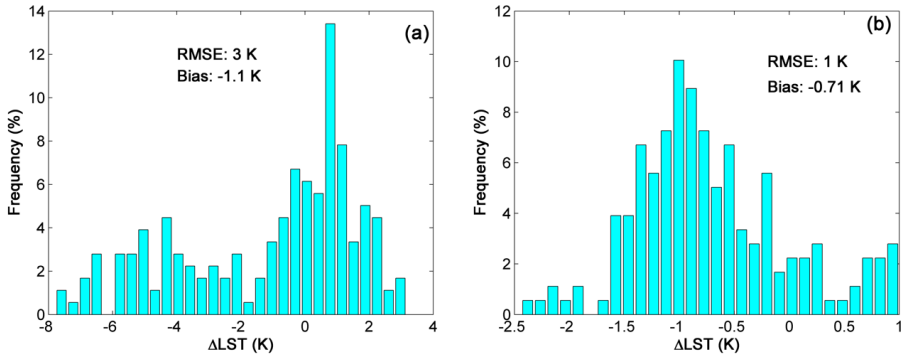

Fig.5. 15. Retrieval results for the daytime data in Spain on October 1, 2018. (a) Histogram of the residuals between the retrieved LST and AVHRR/MetOp LST product with the ANN method. (b) Histogram of the residuals between the retrieved LST and AVHRR/MetOp LST product with the physical method.

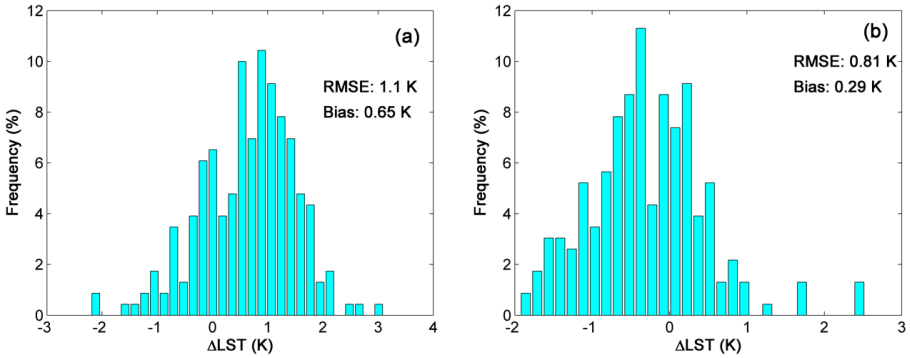

Fig.5. 16. Retrieval results for the nighttime data in Spain on October 2, 2018. (a) Histogram of the residuals between the retrieved LST and AVHRR/MetOp LST product with the ANN method. (b) Histogram of the residuals between the retrieved LST and AVHRR/MetOp LST product with the physical method.

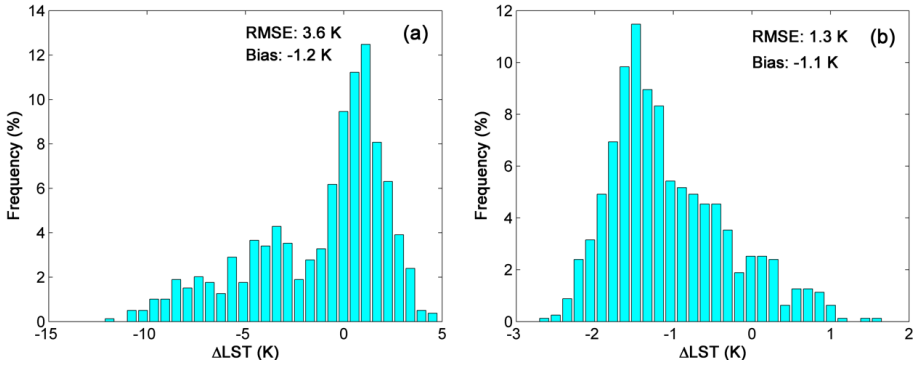

Fig.5. 17. Retrieval results for the daytime data in North Africa on January 2, 2018. (a) Histogram of the residuals between the retrieved LST and AVHRR/MetOp LST product with the ANN method. (b) Histogram of the residuals between the retrieved LST and AVHRR/MetOp LST product with the physical method.

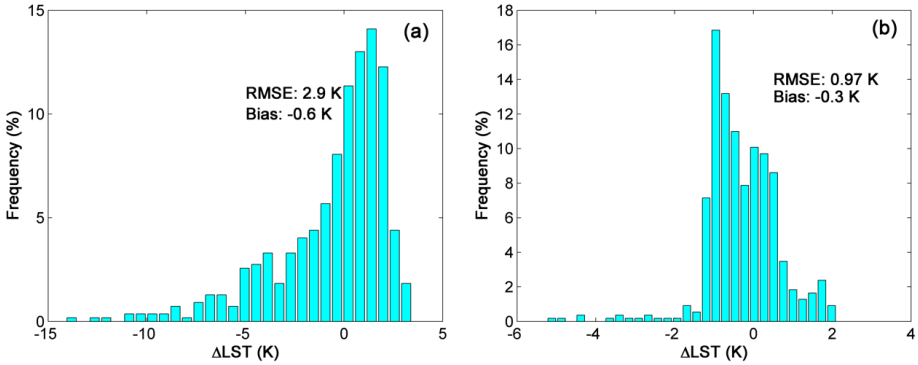

Fig.5. 18. Retrieval results for the nighttime data in North Africa on January 1, 2018. (a) Histogram of the residuals between the retrieved LST and AVHRR/MetOp LST product with the ANN method. (b) Histogram of the residuals between the retrieved LST and AVHRR/MetOp LST product with the physical method.

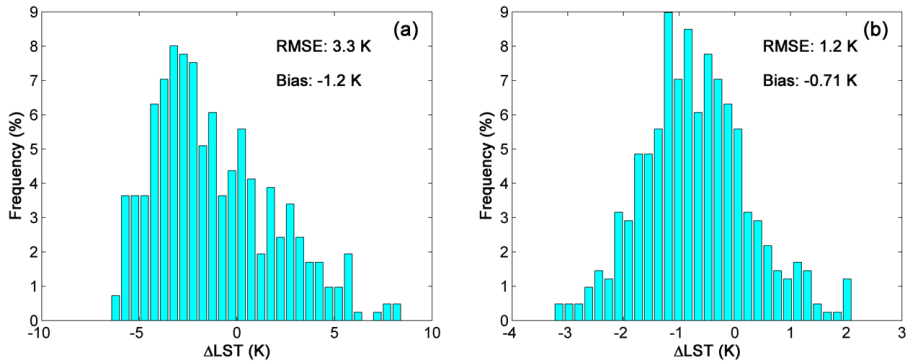

Fig.5. 19. Retrieval results for the daytime data in North Africa on July 2, 2018. (a) Histogram of the residuals between the retrieved LST and AVHRR/MetOp LST product with the ANN method. (b) Histogram of the residuals between the retrieved LST and AVHRR/MetOp LST product with the physical method.

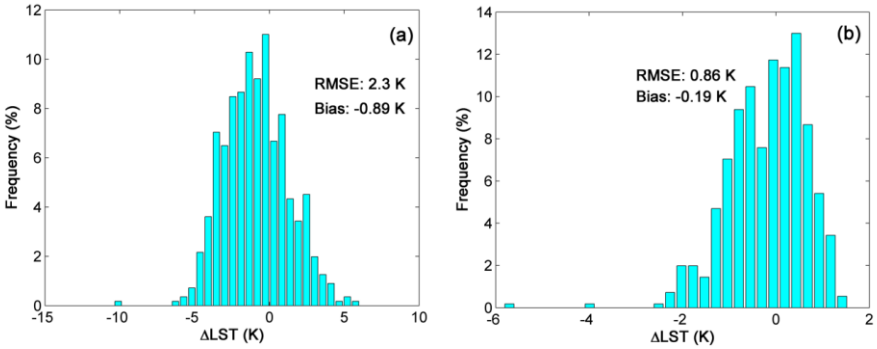

Fig.5. 20. Retrieval results for the nighttime data in North Africa on July 1, 2018. (a) Histogram of the residuals between the retrieved LST and AVHRR/MetOp LST product with the ANN method. (b) Histogram of the residuals between the retrieved LST and AVHRR/MetOp LST product with the Physical method.

The VZA of IASI observations are smaller than 20° due to this physical method only considering nearly vertical observation. Therefore, whether the angle-dependent physical method can be expected, we adopted VZA > 20° IASI observations to test this physical method. The chosen study area is on the east of Europe (a variety of land surface coverages and mostly clear-sky) on July 4, 2015. The viewing zenith angle (VZA) of IASI sensor for this selected area on daytime is small than 20° taking into account the near vertical observation of our simulation dataset above. However, the VZA on nighttime of this area is larger than 20°. Fig.5.21 shows the research area.

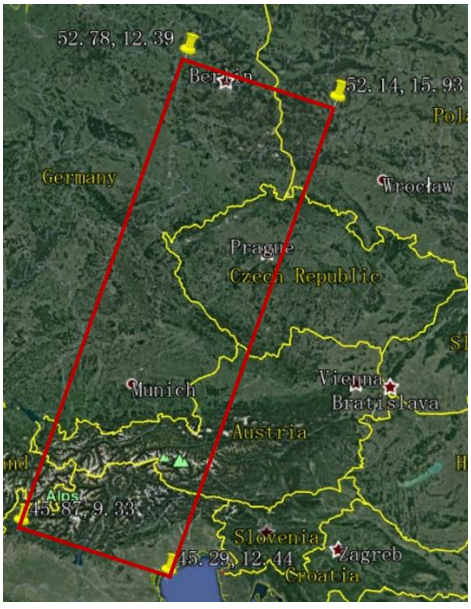

Fig.5. 21. Research area.

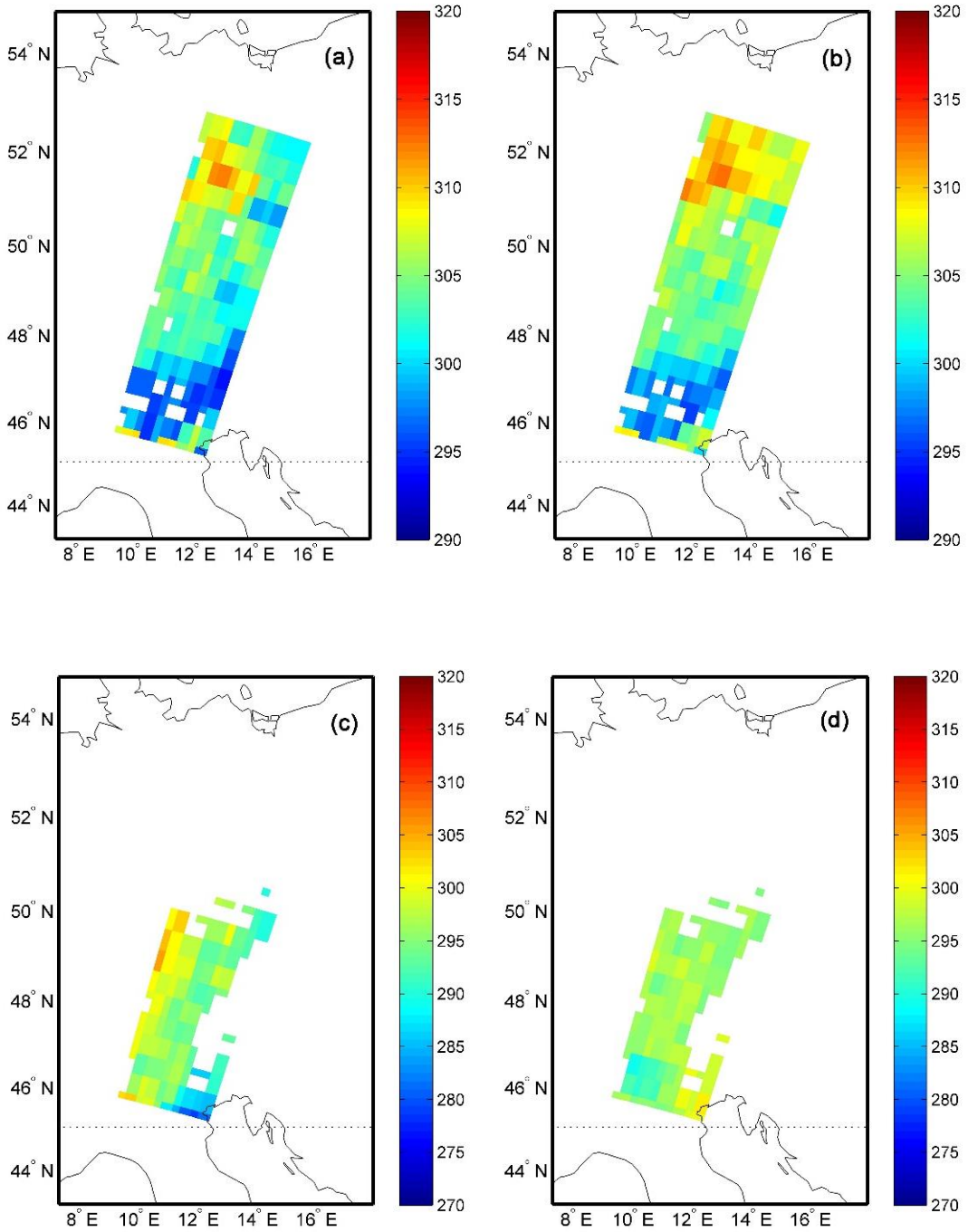

Fig.5. 22. (a) Retrieved LST using ANN method for the daytime data. (b) Retrieved LST using Physical method for the daytime data. (c) Retrieved LST using ANN method for the nighttime data. (d) Retrieved LST using Physical method for the nighttime data.

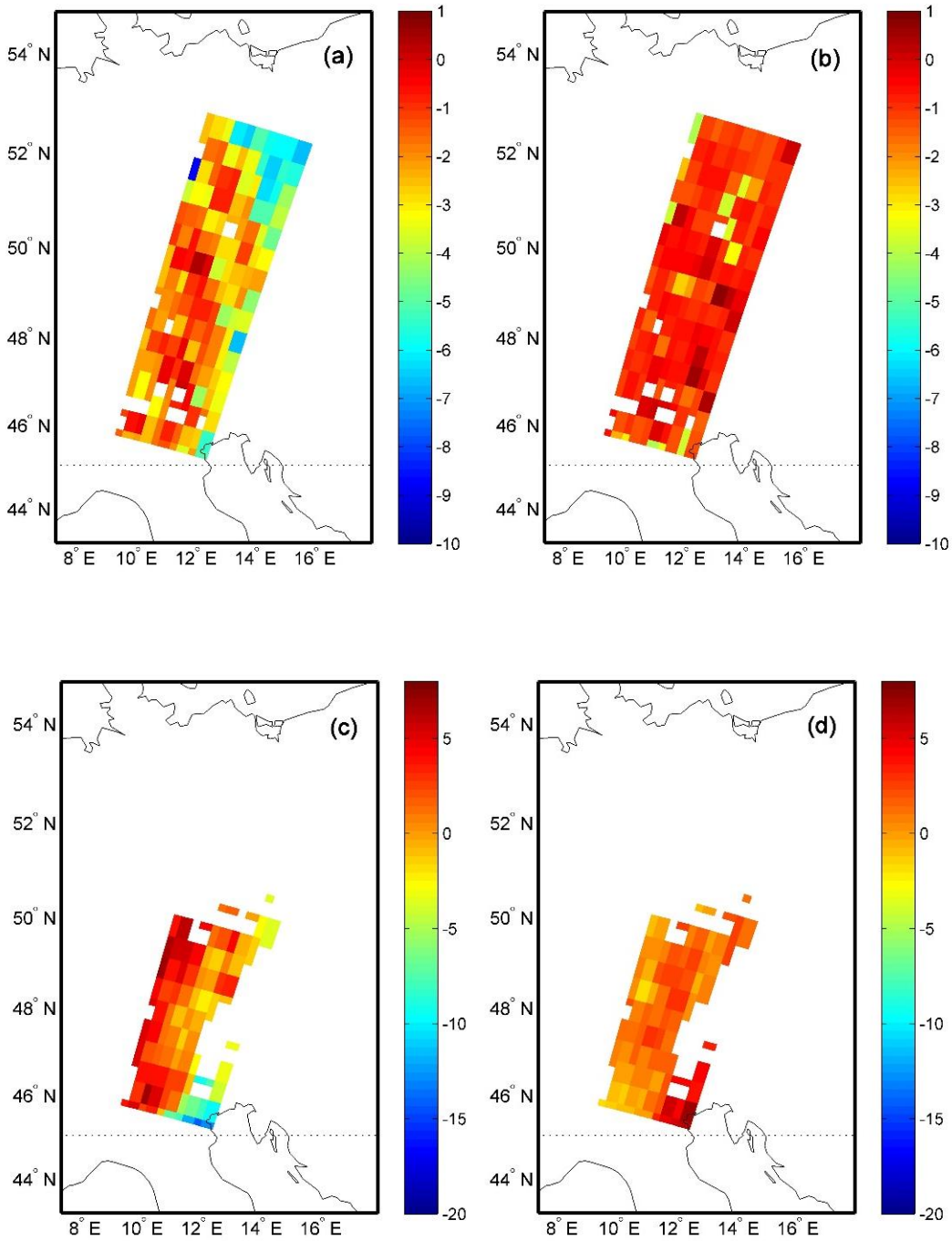

Fig.5. 23. (a) △Ts of Retrieved LST using ANN method for the daytime data. (b) △Ts of Retrieved LST using Physical method for the daytime data. (c) △Ts of Retrieved LST using ANN method for the nighttime data. (d) △Ts of Retrieved LST using Physical method for the nighttime data.

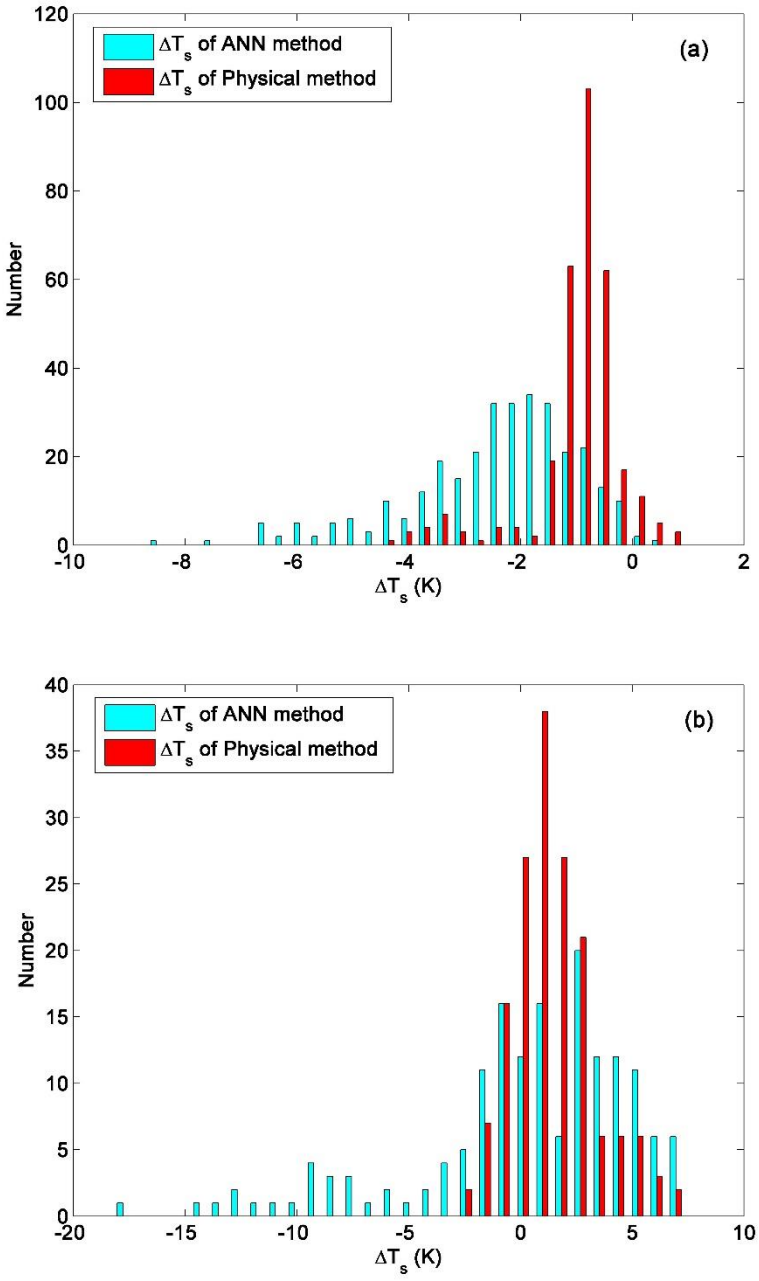

Fig.5. 24. (a) Comparison of △Ts of ANN method and Physical method for the daytime data. (b) Comparison of △Ts of ANN method and Physical method for the nighttime data.

The retrieval RMSEs of ANN method are 3 K (2.86 K) and 5 K (4.75 K) for the daytime and nighttime data, respectively. For the physical method, it is nearly 1 K (1.31 K) and 2 K (2.31 K) for the daytime and nighttime data, respectively, compared with AVHRR/MetOp LST product. Notably, the initial value accuracy estimated with the ANN method is degraded compared to the simulated dataset. This is mainly because the network trained by the simulated data set does not

necessarily contain the actual observed surface and atmospheric information and certainly will influence the accuracy, so a larger simulated dataset covering the surface and atmospheric conditions will bring better results. The nighttime retrieval results demonstrate lower accuracy than daytime data, this is mainly because the VZA of the nighttime data in this area is not nearly vertical observation, angular dependence of TOA radiance strongly effects the retrieval accuracy of ANN method and further influence the retrieval accuracy of physical method.

For the ANN method and physical method, we mainly talk about the near vertical observation, however the ΔT_s does not show a large increase with the increase of the observation VZA angle in this area with the physical method as Fig.5.23 (b) and Fig.5.23 (d) demonstrated. Therefore, the angle-dependent physical method can be expected. The initial value providing by ANN method has angle-dependent effect (Fig.5.23 (a) and Fig.5.23 (c)). Therefore, a multi-angle-dependent neural network training model can be discussed in the future to further improve the accuracy of the initial estimation for real observation.

5.5 Conclusion

In hyperspectral studies, it is generally difficult to simultaneously obtain accurate atmospheric profiles and TIR measurements. Thus, the lack of an accurate atmospheric correction affects the LST retrieval accuracy. The simultaneous retrieval of land surface and atmospheric information would be ideal. The linearized RTE and two-step physical retrieval method can be used to obtain the LST, LSE, and atmospheric profiles. However, this two-step physical method considers the complex vertical structure of the atmospheric profile. Thus, we propose a new approach to relinearize the RTE and retrieve the LST without considering the vertical structure of the atmospheric profile using IASI observations.

A new physical method was developed to retrieve the LST from IASI observations. The RTE was tangent-linearized around the initial estimate with respect to the LST, LSE, *Ta*, and *q*. Subsequently, PCA was used to reduce the number of unknown *Ta* and LSE values. The Tikhonov regularization method and

discrepancy principle iteration algorithm were employed to stabilize the ill-posed problem and obtain the final maximum likelihood solution of the LST. Channel selection is a key issue of this method, leading to inaccurate LST inversion. In this study, it was dynamically varied depending on the weight value (W_{Ts_λ}) calculated from the initial estimate. The initial LST, Ta, and q values can be determined with a multilayer perceptron, which provides good parameter accuracies. The initial value of each channel LSE was set to 0.97.

The proposed algorithm was tested on a simulated IASI dataset. The RMSE of the retrieved LST using the physical method is 0.75 K, with an initial estimate error of 1.9 K based on the ANN method. The physical method yields an improved LST retrieval accuracy (1 K). When 0.97 is used as the LSE_0, the error of the LST retrieval is 0.6 K (RMSE). A Ta_0 value with an error of ±10% leads to a retrieval error of 0.6 K and a q value with an error of ±40% results in an LST retrieval with an error of 0.4 K. Based on an LST with a random error of 3 K, LSE_0 of 0.97, 10% Ta_0 error, and 40% q_0 error, the LST retrieval accuracy is 0.89 K. Within the given error range of the initial values of the simulated dataset, the accuracy of the LST is insignificantly affected, whereas an initial value estimate with a better accuracy improves the accuracy of the LST inversion to a certain extent. The proposed method was also applied to real IASI observations obtained in two study areas. The LST can be retrieved with an accuracy of <1.1 K for Spain and <1.3 K for North Africa. Based on the physical method, the LST retrieval accuracy can be improved. Our proposed method can be used to obtain LST retrievals that coincide with those of the AVHRR/Metop LST product.

Many attempts were made to identify an optimal channel subset for the LST inversion. If we could simultaneously and accurately retrieve the LSE, Ta, and q, this method could be more widely applied. Whether it is possible to identify an optimal channel subset or inversion algorithm to simultaneously and accurately retrieve the LSE, LST, and atmospheric parameters should be explored in the future. Furthermore, only near-vertical observations were simulated using the new physical method. However, angle-dependent ANN and physical methods may further improve the applicability of the algorithm to real observations. However, large-scale regional experiments have not been conducted and more simulation

datasets must be obtained to gather different atmospheric and ground information for the constructed neural network.

Chapter 6. Conclusions and perspectives

6.1 Conclusions

As an important parameter of land surface process, LST has been widely used in many disciplines and fields, and its acquisition methods and accuracy have been paid attention by scholars. In the thermal infrared spectrum, surface temperature, emissivity and atmospheric state parameters are coupled together and affect the satellite observation radiance. The hyperspectral thermal infrared sensor has a narrow channel and a corresponding sharp weight function, which can provide good vertical resolution to detect atmospheric conditions. At the same time, the hyperspectral data contains rich and delicate spectral information, which can not only describe the vertical distribution of atmospheric temperature, humidity, and ozone, but also provide the distribution of other trace gases. In addition, the hyperspectral thermal infrared sensor has a large number of channels, which can increase the stability of the system of equations, and can also provide integrated constraints to provide more constraints that conform to the true physical properties of the surface. Therefore, using hyperspectral thermal infrared satellite data to retrieve surface temperature is a research direction worthy of bold exploration. Based on the above considerations, this thesis takes the surface temperature inversion of hyperspectral infrared data as the research goal, and has completed the following research work, and has obtained corresponding research results and clear conclusions:

1) Assuming that the atmospheric correction has been accurately performed, a method for separating the surface temperature and specific emissivity suitable for hyperspectral thermal infrared data based on the LSEC idea is proposed. This method uses non-equally-spaced piecewise linear functions to fit the emissivity spectrum to greatly reduce the number of parameters to be retrieved so that the number of observations is greater than the number of unknowns, and then solves the equation. This method is defined as Pre-estimate shape (PES)-LSEC method. This proposed method provides the basic tendency of LSE and determine relatively

accurate crest and trough positions, producing a better non-equal-interval segmentation scheme than LSEC method to separate temperature and emissivity. Subsequently, simulated data was used to analyze the sensitivity of the proposed method to at-ground radiation and downward radiation errors of the atmosphere. Compared to LSEC method, the retrieval accuracy of PES-LSEC was improved to a certain extent. Compared to the ISSTES method, LSEC and PES-LSEC showed good noise-resistant ability. For the in situ measurements, with initial-shape estimation, more accurate and less segmentation schemes are given to obtain a better accuracy than that of the LSEC method. The crest and tough information of LSE is better preserved using PES-LSEC method. Most of samples of the errors of LST are within 1 K. These results showed that the PES-LSEC method could give accurate LST if atmospheric correction has been done accurately and further confirm the applicability of the proposed method.

2) A deep learning model that can estimate LST without accurate atmospheric correction for IASI hyperspectral data is developed. The established deep learning model does not require the support of atmospheric information, and it can be used for inversion of the surface temperature by using satellite observe radiance. Therefore, this deep learning model is expected to train and learn the relationship between the IASI observations (brightness temperature) and the LST. This deep mixture model combines the advantages of Deep Neural networks (DNN) and Convolutional neural network (CNN) for extracting features of training data and Long Short-Term Memory (LSTM) model for sequence prediction. The constructed deep learning model was verified using actual satellite data. It was applied on other times IASI real observations to give the LST estimation. Two seasons IASI (Infrared Atmospheric Sounding Interferometer) Tb data in the selected two areas (northern and southern Africa with a variety of land surface coverages and many clear-sky days) are adopted to validate the retrieval accuracy of LST. RMSE of LST for the selected areas are < 3 K validating with the corresponding AVHRR/MetOp LST product. Therefore, our constructed deep mixture model can be used to determine LST with a good retrieval accuracy. Compared to the PES-LSEC method, this method does not require any atmospheric information, but it needs a large

amount of satellite data to train and learn for the network. Inversion for the large-scale area has high requirements on data volume and computing performance.

3) The fifth chapter gives a new physical method to retrieve surface temperature for IASI observations without accurate atmospheric correction based on atmospheric radiation transmission theory. This method is based on two-step physical retrieval method (Ma et al., 2000) and attempts a new simple form to re-linearize the radiative transfer equation (RTE). RTE was tangent-linearized around the initial guess with respect to the LST, the land surface emissivity (LSE), the atmospheric equivalent temperature (Ta), and the water vapor content (q) without considering complicated vertical structure of the atmospheric profile. The principle component-analysis (PCA) technique is used to reduce the number of unknowns for Ta and LSEs. The Tikhonov regularization method and the discrepancy principle iteration algorithm are employed to stabilize the ill-posed problem and obtain the final maximum likelihood solution of the LST. A new channel selection scheme was proposed according to the purpose of giving accurate LST estimation for this physical method. This physical algorithm was tested with both simulated and real data from the IASI sensor. The root-mean-square error (RMSE) of LST for the simulated data is about 1 K with the estimate initial LST value RMSE error 2 K (1.9 K). The sensitivity analysis showed that the retrieval accuracy of LST is nearly 1 K with the 3 K random error on LST initial estimation, constant LSE initial estimation (0.97), 10% relative error on each channel of Ta initial estimation and 40% relative error on q initial estimation. Within the given initial error range values for the simulated dataset, the retrieval accuracy of LST is not greatly affected by the initial estimate of the unknown variables. Finally, compared to the AVHRR/MetOp LST product, this physical method improves the ANN retrieval LST accuracy within 1.5 K for daytime data, and within 1 K for nighttime data for the selected actual IASI data in research area. It is capable of retrieving LST with accuracy similar to that of the AVHRR/MetOp LST product.

6.2 Perspectives

In this dissertation research, we developed three methods to retrieve LST for hyperspectral TIR data. The PES-LSEC method has good performance on LST

retrieval with accurate atmospheric correction. Deep learning and physical method can provide us the LST information without any prior atmospheric information. Future work would proceed in the following two aspects.

(1) In this dissertation research we develop a deep mixture network to retrieve the LST. This method successfully settles the problem that obtaining accurate atmospheric parameters synchronously with TIR measurements for LST retrieval. The retrieved LST estimates present good accuracy. However, this method can be tested with measurement data to further demonstrate its effectiveness. We will find more data to validate this network.

(2) For the proposed physical method, we have made many attempts to give an optimal subset channels to benefit the LST inversion. If we can accurately retrieve LSE, Ta, and q at the same time, not only LST, then this method will be more widely applied. Whether it is possible to find an optimal channel subset or inversion algorithm to accurately give LSE, LST and atmospheric parameters simultaneously is another issue that can be explored in the future. Furthermore, only nearly vertical observation is simulated and discussed for this physical method, angle-dependent ANN method and physical method may be expected to further improve the applicability of the algorithm for real observation. On the other hand, large-scale regional experiments have not been conducted, it may need to collect more simulation data sets to describe different atmospheric and ground information for the constructed neural network.

References

Aires, Filipe, Chédin, A., Scott, N.A., Rossow, W.B., 2002. A regularized neural net approach for retrieval of atmospheric and surface temperatures with the IASI instrument. J. Appl. Meteorol. 41, 144–159.

Aires, F., Prigent, C., Rossow, W.B., Rothstein, M., 2001. A new neural network approach including first guess for retrieval of atmospheric water vapor, cloud liquid water path, surface temperature, and emissivities over land from satellite microwave observations. J. Geophys. Res. Atmos. 106, 14887–14907.

Aires, F., Rossow, W.B., Scott, N.A., Chédin, A., 2002a. Remote sensing from the infrared atmospheric sounding interferometer instrument 1. Compression, denoising, and first-guess retrieval algorithms. J. Geophys. Res. Atmos. 107.

Aires, F., Rossow, W.B., Scott, N.A., Chédin, A., 2002b. Remote sensing from the infrared atmospheric sounding interferometer instrument 2. Simultaneous retrieval of temperature, water vapor, and ozone atmospheric profiles. J. Geophys. Res. Atmos. 107, 1–12.

Anderson, M C, Norman, J.M., Kustas, W.P., Houborg, R., Starks, P.J., Agam, N., 2008. A thermal-based remote sensing technique for routine mapping of land-surface carbon, water and energy fluxes from field to regional scales. Remote Sens. Environ. 112, 4227–4241.

Atitar, M., Sobrino, J.A., 2008. A split-window algorithm for estimating LST from Meteosat 9 data: Test and comparison with in situ data and MODIS LSTs. IEEE Geosci. Remote Sens. Lett. 6, 122–126.

Aumann, H.H., Chahine, M.T., Gautier, C., Goldberg, M.D., Kalnay, E., McMillin, L.M., Revercomb, H., Rosenkranz, P.W., Smith, W.L., Staelin, D.H., Strow, L.L., Susskind, J., 2003. AIRS/AMSU/HSB on the aqua mission: Design, science objectives, data products, and processing systems. IEEE Trans. Geosci. Remote Sens. 41, 253–263.

Ba, J.L., Kiros, J.R., Hinton, G.E., 2016. Layer normalization. arXiv Prepr. arXiv1607.06450.

Baldridge, Alice M, Hook, S.J., Grove, C.I., Rivera, G., 2009. The ASTER spectral library version 2.0. Remote Sens. Environ. 113, 711–715.

Baldridge, A. M., Hook, S.J., Grove, C.I., Rivera, G., 2009. The ASTER spectral library version 2.0. Remote Sens. Environ. 113, 711–715.

Balick, L., Gillespie, A., French, A., Danilina, I., Allard, J.-P., Mushkin, A., 2008. Longwave thermal infrared spectral variability in individual rocks. IEEE Geosci. Remote Sens. Lett. 6, 52–56.

Barducci, A., Pippi, I., 1996. Temperature and emissivity retrieval from remotely sensed images using the" grey body emissivity" method. IEEE Trans. Geosci. Remote Sens. 34, 681–695.

Becker, F., 1987. The impact of spectral emissivity on the measurement of land surface temperature from a satellite. Int. J. Remote Sens. 8, 1509–1522.

Becker, F., Li, Z.-L., 1990a. Towards a local split window method over land surfaces. Remote Sens. 11, 369–393.

Becker, F., Li, Z.-L., 1990b. Temperature-independent spectral indices in thermal infrared bands. Remote Sens. Environ. 32, 17–33.

Becker, F., Zhao-Liang Li, 1995. Surface temperature and emissivity at various scales: definition, measurement and related problems. Remote Sens. Rev. 12, 225–253.

Bengio, Y., 2009. Learning deep architectures for AI. Now Publishers Inc.

Bloom, H.J., 2001. The cross-track infrared sounder (CrIS): A sensor for operational meteorological remote sensing. Int. Geosci. Remote Sens. Symp. 3, 1341–1343.

Borel, C., 2008. Error analysis for a temperature and emissivity retrieval algorithm for hyperspectral imaging data. Int. J. Remote Sens. 29, 5029–5045.

Borel, C., 2003. ARTEMISS - an Algorithm to Retrieve Temperature and Emissivity from Hyper-Spectral Thermal Image Data. 28th Annu. GOMACTech Conf. 3–6.

Borel, C., 1997. Iterative Retrieval of Surface Emissivity and Temperature for a Hyperspectral Sensor. First JPL Work. Remote Sens. L. Surf. Emiss.

Borel, C.C., 1998. Surface emissivity and temperature retrieval for a hyperspectral sensor. Int. Geosci. Remote Sens. Symp. 1, 546–549.

Boureau, Y.-L., Ponce, J., LeCun, Y., 2010. A theoretical analysis of feature pooling in visual recognition, in: Proceedings of the 27th International Conference on Machine Learning (ICML-10). pp. 111–118.

Brunsell, N.A., Gillies, R.R., 2003. Length scale analysis of surface energy fluxes derived from remote sensing. J. Hydrometeorol. 4, 1212–1219.

Chaumat, L., Standfuss, C., Tournier, B., Armante, R., Scott, N.A., 2009. 4A/OP reference documentation. NOV-3049-NT-1178-v4. 0, Nov. LMD/CNRS, CNES 307.

Chaumat, L., Standfuss, C., Tournier, B., Bernard, E., Armante, R., Scott, N.A., 2012. 4A/OP Reference Documentation. NOV-3049-NT-1178-v4.3, Nov. LMD/CNRS, CNES, 311 pp.

Chédin, A., Scott, N.A., Claud, C., Bonnet, B., Escobar, J., Dardaillon, S., Cheruy, F., Husson, N., 1994. Global scale observation of the Earth for climate studies. Adv. Sp. Res. 14, 155–159.

Chedin, A., Scott, N.A., Wahiche, C., Moulinier, P., 1985. The improved initialization inversion method: A high resolution physical method for temperature retrievals from satellites of the TIROS-N series. J. Clim. Appl. Meteorol. 24, 128–143.

Chen, M., Ni, L., Jiang, X., Wu, H., 2019. Retrieving atmospheric and land surface parameters from at-sensor thermal infrared hyperspectral data with artificial neural network. IEEE J. Sel. Top. Appl. Earth Obs. Remote Sens. 12, 2409–2416.

Cheng, J., Liang, S., Wang, J., Li, X., 2010. A stepwise refining algorithm of temperature and emissivity separation for hyperspectral thermal infrared data. IEEE Trans. Geosci. Remote Sens. 48, 1588–1597.

Cheng, J., Liu, Q.H., Li, X.W., Xiao, Q., Liu, Q., Du, Y.M., 2008. Correlation-based temperature and emissivity separation algorithm. Sci. China, Ser. D Earth Sci. 51, 357–369.

Chevallier, F., Chéruy, F., Scott, N.A., Chédin, A., 1998. A neural network approach for a fast and accurate computation of a longwave radiative budget. J. Appl. Meteorol. 37, 1385–1397.

Coll, C., Caselles, V., Sobrino, J.A., Valor, E., 1994. On the atmospheric dependence of the split-window equation for land surface temperature. Remote Sens. 15, 105–122.

Collard, A.D., 2007. Selection of IASI channels for use in numerical weather prediction. Q. J. R. Meteorol. Soc. 133, 496.

Collard, A.D., Matricardi, M., 2005. Selection of a subset of IASI Channels for Near Real Time Dissemination. Proc. ITSC-XIV.

Da, K., 2014. A method for stochastic optimization. arXiv Prepr. arXiv1412.6980.

Dash, Prasanjit, Göttsche, F.-M., Olesen, F.-S., Fischer, H., 2002. Land surface temperature and emissivity estimation from passive sensor data: Theory and practice-current trends. Int. J. Remote Sens. 23, 2563–2594.

Dash, P., Göttsche, F.M., Olesen, F.S., Fischer, H., 2002. Land surface temperature and emissivity estimation from passive sensor data: Theory and practice-current trends. Int. J. Remote Sens. 23, 2563–2594.

Daxini, S.D., Prajapati, J.M., 2020. Numerical shape optimization based on meshless method and stochastic optimization technique. Eng. Comput. 36, 565–586.

EUMETSAT, I., 2012. IASI Level 1 Product Guide.

Galve, J.M., Coll, C., Caselles, V., Valor, E., 2008. An atmospheric radiosounding database for generating land surface temperature algorithms. IEEE Trans. Geosci. Remote Sens. 46, 1547–1557.

Gillespie, A, Alley, R., Kahle, A., Cothern, S., 1998. In-scene atmospheric characterization and compensation in hyperspectral thermal infrared images.

Gillespie, Alan, Rokugawa, S., Matsunaga, T., Cothern, J.S., Hook, S., Kahle, A.B., 1998. A temperature and emissivity separation algorithm for Advanced Spaceborne Thermal Emission and Reflection Radiometer (ASTER) images. IEEE Trans. Geosci. Remote Sens. 36, 1113–1126.

Girshick, R., Donahue, J., Darrell, T., Malik, J., 2016. Region-Based Convolutional Networks for Accurate Object Detection and Segmentation. IEEE Trans. Pattern Anal. Mach. Intell. 38, 142–158.

Goldberg, M.D., Qu, Y., McMillin, L.M., Wolf, W., Zhou, L., Divakarla, M., 2003. AIRS near-real-time products and algorithms in support of operational numerical weather prediction. IEEE Trans. Geosci. Remote Sens. 41, 379–388.

Gu, D.G., Gillespie, A., Kahle, A., Palluconi, F., 2000. Autonomous atmospheric compensation (AAC) of high resolution hyperspectral thermal infrared remote-sensing imagery. Geosci. Remote Sensing, IEEE Trans. 38, 2557–2570.

Hansen, P.C., O'Leary, D.P., 1993. The use of the L-curve in the regularization of discrete ill-posed problems. SIAM J. Sci. Comput. 14, 1487–1503.

He, K., Zhang, X., Ren, S., Sun, J., 2016. Deep residual learning for image recognition, in: Proceedings of the IEEE Conference on Computer Vision and Pattern Recognition. pp. 770–778.

Hilton, F., Armante, R., August, T., Barnet, C., Bouchard, A., Camy-Peyret, C., Capelle, V., Clarisse, L., Clerbaux, C., Coheur, P.F., Collard, A., Crevoisier, C., Dufour, G., Edwards, D., Faijan, F., Fourrié, N., Gambacorta, A., Goldberg, M., Guidard, V., Hurtmans, D., Illingworth, S., Jacquinet-Husson, N., Kerzenmacher, T., Klaes, D., Lavanant, L., Masiello, G., Matricardi, M., McNally, A., Newman, S., Pavelin, E., Payan, S., Péquignot, E., Peyridieu, S., Phulpin, T., Remedios, J., Schlüssel, P., Serio, C., Strow, L., Stubenrauch, C., Taylor, J., Tobin, D., Wolf, W., Zhou, D., 2012. Hyperspectral earth observation from IASI. Bull. Am. Meteorol. Soc. 93, 347–370.

Hochreiter, S., Schmidhuber, J., 1997. Long short-term memory. Neural Comput. 9, 1735–1780.

Hook, S.J., Gabell, A.R., Green, A.A., Kealy, P.S., 1992. A comparison of techniques for extracting emissivity information from thermal infrared data for geologic studies. Remote Sens. Environ. 42, 123–135.

Horton, K.A., Johnson, J.R., Lucey, P.G., 1998. Infrared measurements of pristine and disturbed soils 2. Environmental effects and field data reduction. Remote Sens. Environ. 64, 47–52.

Huang, S.-X., Li, J., 2000. Theoretical and Numerical Analysis of Inversion of Satellite Remote Sensing, in: Begehr, H.G.W., Gilbert, R.P., Kajiwara, J. (Eds.), Proceedings of the Second ISAAC Congress: Volume 1: This Project Has

Been Executed with Grant No. 11--56 from the Commemorative Association for the Japan World Exposition (1970). Springer US, Boston, MA, pp. 129–136.

Hubbard, B.E., Hooper, D.M., Solano, F., Mars, J.C., 2018. Determining mineralogical variations of aeolian deposits using thermal infrared emissivity and linear deconvolution methods. Aeolian Res. 30, 54–96.

Ioffe, S., Szegedy, C., 2015. Batch normalization: Accelerating deep network training by reducing internal covariate shift. arXiv Prepr. arXiv1502.03167.

Jielun Sun, Mahrt, L., 1995. Determination of surface fluxes from the surface radiative temperature. J. Atmos. Sci.

Kanani, K., 2005. Utilisation de la très haute résolution spectrale pour la mesure en environnement extérieur de l'émissivité de surface dans la bande infrarouge 3-13 Mum: Méthodes et validation expérimentale.

Kanani, K., Poutier, L., Nerry, F., Stoll, M.-P., 2007a. Directional effects consideration to improve out-doors emissivity retrieval in the 3–13 µm domain. Opt. Express 15, 12464–12482.

Kanani, K., Poutier, L., Nerry, F., Stoll, M.-P., 2007b. Directional effects consideration to improve out-doors emissivity retrieval in the 3-13 µm domain. Opt. Express 15, 12464.

Kolmogorov, A.N., 1957. On the representation of continuous functions of many variables by superposition of continuous functions of one variable and addition, in: Doklady Akademii Nauk. Russian Academy of Sciences, pp. 953–956.

Krizhevsky, A., Sutskever, I., Hinton, G.E., 2012. Imagenet classification with deep convolutional neural networks, in: Advances in Neural Information Processing Systems. pp. 1097–1105.

Li, J., Fengxian, Z., Qingcun, Z., 1994. Simultaneous non-linear retrieval of atmospheric temperature and absorbing constituent profiles from satellite infrared sounder radiances. Adv. Atmos. Sci. 11, 128–138.

Li, Jun, Li, Jinlong, Weisz, E., Zhou, D.K., 2007. Physical retrieval of surface emissivity spectrum from hyperspectral infrared radiances. Geophys. Res. Lett. 34, 4–9.

Li, Z.L., Tang, B.H., Wu, H., Ren, H., Yan, G., Wan, Z., Trigo, I.F., Sobrino, J.A., 2013. Satellite-derived land surface temperature: Current status and perspectives. Remote Sens. Environ. 131, 14–37.

Liou, K.-N., 2002. An introduction to atmospheric radiation. Elsevier.

Liu, X., Smith, W.L., Zhou, D.K., Larar, A., 2006. Principal component-based radiative transfer model for hyperspectral sensors: Theoretical concept. Appl. Opt. 45, 201–209.

Liu, X., Zhou, D.K., Larar, A.M., Smith, W.L., Schluessel, P., Newman, S.M., Taylor, J.P., Wu, W., 2009. Retrieval of atmospheric profiles and cloud properties from IASI spectra using super-channels. Atmos. Chem. Phys. 9, 9121–9142.

Ma, X.L., Schmit, T.J., Smith, W.L., 1999. A nonlinear physical retrieval algorithm - Its application to the GOES-8/9 sounder. J. Appl. Meteorol. 38, 501–513.

Ma, X.L., Wan, Z., Moeller, C.C., Menzel, W.P., Gumley, L.E., 2002. Simultaneous retrieval of atmospheric profiles, land-surface temperature, and surface emissivity from Moderate-Resolution Imaging Spectroradiometer thermal infrared data: extension of a two-step physical algorithm. Appl. Opt. 41, 909.

Ma, X.L., Wan, Z., Moeller, C.C., Menzel, W.P., Gumley, L.E., Zhang, Y., 2000. Retrieval of geophysical parameters from Moderate Resolution Imaging Spectroradiometer thermal infrared data: evaluation of a two-step physical algorithm. Appl. Opt. 39, 3537.

Martinet, P., Lavanant, L., Fourrié, N., Rabier, F., Gambacorta, A., 2014. Evaluation of a revised IASI channel selection for cloudy retrievals with a focus on the Mediterranean basin. Q. J. R. Meteorol. Soc. 140, 1563–1577.

Mas, J.F., Flores, J.J., 2008. The application of artificial neural networks to the analysis of remotely sensed data. Int. J. Remote Sens. 29, 617–663.

Masiello, G., Serio, C., 2013. Simultaneous physical retrieval of surface emissivity spectrum and atmospheric parameters from infrared atmospheric sounder interferometer spectral radiances. Appl. Opt. 52, 2428–2446.

McCabe, M.F., Wood, E.F., Wójcik, R., Pan, M., Sheffield, J., Gao, H., Su, H., 2008. Hydrological consistency using multi-sensor remote sensing data for water and energy cycle studies. Remote Sens. Environ. 112, 430–444.

McMillin, L.M., 1975. Estimation of sea surface temperatures from two infrared window measurements with different absorption. J. Geophys. Res. 80, 5113–5117.

Meerdink, S.K., Hook, S.J., Roberts, D.A., Abbott, E.A., 2019. The ECOSTRESS spectral library version 1.0. Remote Sens. Environ. 230, 111196.

Motteler, H.E., Strow, L.L., McMillin, L., Gualtieri, J.A., 1995. Comparison of neural networks and regression-based methods for temperature retrievals. Appl. Opt. 34, 5390.

Mushkin, A., Balick, L.K., Gillespie, A.R., 2005. Extending surface temperature and emissivity retrieval to the mid-infrared (3–5 μm) using the Multispectral Thermal Imager (MTI). Remote Sens. Environ. 98, 141–151.

Nair, V., Hinton, G.E., 2010. Rectified linear units improve restricted boltzmann machines, in: Proceedings of the 27th International Conference on Machine Learning (ICML-10). pp. 807–814.

Ottlé, C., Vidal-Madjar, D., 1992. Estimation of land surface temperature with NOAA 9 data. Remote Sens. Environ. 40, 27–41.

Ouyang, X., Kang, G., Zeng, F., Qi, E., Li, Z.L., 2013. Preliminary applications of a land surface temperature retrieval method to IASI and AIRS data. Int. J. Remote Sens. 34, 3128–3139.

Paul, M., Aires, F., Prigent, C., Trigo, I.F., Bernardo, F., 2012. An innovative physical scheme to retrieve simultaneously surface temperature and emissivities using high spectral infrared observations from IASI. J. Geophys. Res. Atmos. 117, 1–15.

Pavelka, A., Procházka, A., 2004. Algorithms for initialization of neural network weights. Sb. Prisp. 12. rocniku Konf. MATLAB 2004 2, 453–459.

Pearson, R.K., 2002. Outliers in process modeling and identification. IEEE Trans. Control Syst. Technol. 10, 55–63.

Péquignot, E., Chédin, A., Scott, N.A., 2008. Infrared continental surface emissivity spectra retrieved from AIRS hyperspectral sensor. J. Appl. Meteorol. Climatol. 47, 1619–1633.

Prata, A.J., 1994. Land surface temperature determination from satellites. Adv. Sp. Res. 14, 15–26.

Price, J.C., 1984. Land surface temperature measurements from the split window channels of the NOAA-7 AVHRR. J. Geophys. Res. 79, 5039–5044.

Price, J.C., 1983. Estimating surface temperatures from satellite thermal infrared data—A simple formulation for the atmospheric effect. Remote Sens. Environ. 13, 353–361.

Qin, Z., Dall'Olmo, G., Karnieli, A., Berliner, P., 2001. Derivation of split window algorithm and its sensitivity analysis for retrieving land surface temperature from NOAA-advanced very high resolution radiometer data. J. Geophys. Res. Atmos. 106, 22655–22670.

Ryu, Y., Kang, S., Moon, S.-K., Kim, J., 2008. Evaluation of land surface radiation balance derived from moderate resolution imaging spectroradiometer (MODIS) over complex terrain and heterogeneous landscape on clear sky days. Agric. For. Meteorol. 148, 1538–1552.

Sainath, T.N., Vinyals, O., Senior, A., Sak, H., 2015. Convolutional, long short-term memory, fully connected deep neural networks, in: 2015 IEEE International Conference on Acoustics, Speech and Signal Processing (ICASSP). IEEE, pp. 4580–4584.

Santurkar, S., Tsipras, D., Ilyas, A., Madry, A., 2018. How does batch normalization help optimization?, in: Advances in Neural Information Processing Systems. pp. 2483–2493.

Schmidhuber, J., 2015. Deep learning in neural networks: An overview. Neural networks 61, 85–117.

Scott, N.A., Chedin, A., 1981. A fast line-by-line method for atmospheric absorption computations: the automatized atmospheric absorption atlas. J. Appl. Meteorol.

Singh, A., 1993. Principal components analysis in remote sensing. Int. Geosci. Remote Sens. Symp. 4, 1680–1682.

Smith, W.L., Woolf, H.M., 1976. Use of Eigenvectors of Statistical Covariance Matrices for Interpreting Satellite Sounding Radiometer Observations. J. Atmos. Sci.

Snyder, J.P., 1987. Map projections: a working manual (US Geological Survey Professional Paper). US Gov. Print. Off. 1395.

Snyder, W.C., Wan, Z., Zhang, Y., Feng, Y.-Z., 1998. Classification-based emissivity for land surface temperature measurement from space. Int. J. Remote Sens. 19, 2753–2774.

Sobrino, J.A., Coll, C., Caselles, V., 1991. Atmospheric correction for land surface temperature using NOAA-11 AVHRR channels 4 and 5. Remote Sens. Environ. 38, 19–34.

Sobrino, J.A., Jiménez-Muñoz, J.C., Sòria, G., Romaguera, M., Guanter, L., Moreno, J., Plaza, A., Martínez, P., 2008. Land surface emissivity retrieval from different VNIR and TIR sensors. IEEE Trans. Geosci. Remote Sens. 46, 316–327.

Sobrino, J.A., Li, Z.-L., Stoll, M.P., Becker, F., 1994. Improvements in the split-window technique for land surface temperature determination. IEEE Trans. Geosci. Remote Sens. 32, 243–253.

Sobrino, J.A., Li, Z.L., Stoll, M.P., Becker, F., 1996. Multi-channel and multi-angle algorithms for estimating sea and land surface temperature with ATSR data. Int. J. Remote Sens. 17, 2089–2114.

Sobrino, J.A., Sòria, G., Prata, A.J., 2004. Surface temperature retrieval from Along Track Scanning Radiometer 2 data: Algorithms and validation. J. Geophys. Res. Atmos. 109.

Sontag, E.D., 1992. Feedback Stabilization Using Two-Hidden-Layer Nets. IEEE Trans. Neural Networks 3, 981–990.

Susskind, J., Rosenfield, J., Reuter, D., Chahine, M.T., 1984. Remote sensing of weather and climate parameters from HIRS2/MSU on TIROS - N. J. Geophys. Res. Atmos. 89, 4677–4697.

Szegedy, C., Toshev, A., Erhan, D., 2013. Deep neural networks for object detection, in: Advances in Neural Information Processing Systems. pp. 2553–2561.

Tikhonov, A.N., Arsenin, V.Y., 1977. Solutions of ill-posed problems. New York 1–30.

Tournier, B., Camy-Peyret, C., 2003. The IASI level 1c: Instrument Spectral Response Function (ISRF).", in: ISSWG17, Darmstadt, Allemagne–1-3 Avril 2003.

Valueva, M. V, Nagornov, N.N., Lyakhov, P.A., Valuev, G. V, Chervyakov, N.I., 2020. Application of the residue number system to reduce hardware costs of the convolutional neural network implementation. Math. Comput. Simul.

Van de Griend, A.A., OWE, M., 1993. On the relationship between thermal emissivity and the normalized difference vegetation index for natural surfaces. Int. J. Remote Sens. 14, 1119–1131.

Ventress, L., Dudhia, A., 2014. Improving the selection of IASI channels for use in numerical weather prediction. Q. J. R. Meteorol. Soc. 140, 2111–2118.

Vining, R.C., Blad, B.L., 1992. Estimation of sensible heat flux from remotely sensed canopy temperatures. J. Geophys. Res. Atmos. 97, 18951–18954.

Wan, Z., Jeff, D., 1996. A generalized split-window algorithm for retrieving land-surface temperature from space. IEEE Trans. Geosci. Remote Sens. 34, 892–905.

Wan, Z., Li, Z.-L., 1997. A physics-based algorithm for retrieving land-surface emissivity and temperature from EOS/MODIS data. IEEE Trans. Geosci. Remote Sens. 35, 980–996.

Wang, N., Li, Z.L., Tang, B.H., Zeng, F., Li, C., 2013. Retrieval of atmospheric and land surface parameters from satellite-based thermal infrared hyperspectral data using a neural network technique. Int. J. Remote Sens. 34, 3485–3502.

Wang, N., Wu, H., Nerry, F., Li, C., Li, Z.L., 2011. Temperature and emissivity retrievals from hyperspectral thermal infrared data using linear spectral emissivity constraint. IEEE Trans. Geosci. Remote Sens. 49, 1291–1303.

Wang, X., OuYang, X., Tang, B., Li, Z.L., Zhang, R., 2008. A new method for temperature/emissivity separation from hyperspectral thermal infrared data. Int. Geosci. Remote Sens. Symp. 3.

Watson, K., 1992. Two-temperature method for measuring emissivity. Remote Sens. Environ. 42, 117–121.

Widmann, A., Schröger, E., Maess, B., 2015. Digital filter design for electrophysiological data–a practical approach. J. Neurosci. Methods 250, 34–46.

Young, S.J., Johnson, B.R., Hackwell, J.A., 2002. An in-scene method for atmospheric compensation of thermal hyperspectral data. J. Geophys. Res. Atmos. 107, 1–20.

Yousefi, B., Sojasi, S., Castanedo, C.I., Maldague, X.P. V, Beaudoin, G., Chamberland, M., 2018. Continuum removal for ground-based LWIR hyperspectral infrared imagery applying non-negative matrix factorization. Appl. Opt. 57, 6219–6228.

Yu, X., Wu, X., Luo, C., Ren, P., 2017. Deep learning in remote sensing scene classification: a data augmentation enhanced convolutional neural network framework. GIScience Remote Sens. 54, 741–758.

Yu, Y., Privette, J.L., Pinheiro, A.C., 2007. Evaluation of split-window land surface temperature algorithms for generating climate data records. IEEE Trans. Geosci. Remote Sens. 46, 179–192.

Yuan, F., Bauer, M.E., 2007. Comparison of impervious surface area and normalized difference vegetation index as indicators of surface urban heat island effects in Landsat imagery. Remote Sens. Environ. 106, 375–386.

Zhang, Y., Qiu, Z., Yao, T., Liu, D., Mei, T., 2018. Fully Convolutional Adaptation Networks for Semantic Segmentation. Proc. IEEE Comput. Soc. Conf. Comput. Vis. Pattern Recognit. 6810–6818.

Zhang, Y.Z., Wu, H., Jiang, X.G., Jiang, Y.Z., Liu, Z.X., Nerry, F., 2017. Land surface temperature and emissivity retrieval from field-measured hyperspectral thermal infrared data using wavelet transform. Remote Sens. 9.

Zhong, X., Huo, X., Ren, C., Labed, J., Li, Z.L., 2016. Retrieving land surface temperature from hyperspectral thermal infrared data using a multi-channel method. Sensors (Switzerland) 16, 1–14.

Zhong, X., Labed, J., Zhou, G., Shao, K., Li, Z.L., 2015. A multi-channel method for retrieving surface temperature for high-emissivity surfaces from hyperspectral thermal infrared images. Sensors (Switzerland) 15, 13406–13423.

Zhou, D.K., Larar, A.M., Liu, X., Smith, W.L., Strow, L.L., Yang, P., Schlüssel, P., Calbet, X., 2011. Global land surface emissivity retrieved from satellite

ultraspectral IR measurements. IEEE Trans. Geosci. Remote Sens. 49, 1277–1290.

Zhou, D.K., Smith, W.L., Li, J., Howell, H.B., Cantwell, G.W., Larar, A.M., Knuteson, R.O., Tobin, D.C., Revercomb, H.E., Mango, S.A., 2002. Thermodynamic product retrieval methodology and validation for NAST-I. Appl. Opt. 41, 6957.

Xinyu LAN

Land surface temperature retrieval from hyperspectral thermal infrared data

Résumé

Notre recherche utilise les données TIR hyperspectrales comme principale source d'information et vise à accéder à la température de surface terrestre (LST). Une méthode pré-estimant la forme de la courbe spectrale de LSE (PSE)-LSEC a été proposée pour séparer LST et LSE. Pour les mesures in situ, les erreurs sur la LST se situent à moins de 1 K. Un modèle de « deep learning » a été développé permettant de restituer directement la LST sans correction atmosphérique préalable à partir de données hyperspectrales de l'instrument IASI. Le RMSE de LST restituée par ce modèle sont de 3 K en comparant avec le produit LST de l'AVHRR/MetOp pour les zones sélectionnées. Une nouvelle méthode physique a été développée pour restituer la LST à partir de données hyperspectrales de l'instrument IASI sans correction atmosphérique. Ces valeurs montrent que la méthode proposée est capable de déterminer les LSTs avec une précision similaire à celle de l'AVHRR/MetOp.

Résumé en anglais

Our research adopts hyperspectral thermal infrared (TIR) data as the main source information to retrieve land surface temperature (LST). A pre-estimate shape (PES)-LSEC method was proposed to separate temperature and emissivity. For the in situ measurements, most of samples of the errors of LST are within 1 K. A deep mixture model that can estimate LST without accurate atmospheric correction for IASI hyperspectral data is developed. RMSE of LST for the selected areas are < 3 K validating with the corresponding AVHRR/MetOp LST product. A new physical method was developed to retrieve LST for IASI observations without accurate atmospheric correction. It is capable of retrieving LST with accuracy similar to that of the AVHRR/MetOp LST product.